A GLOBAL RESERVOIR DATABASE FOR HIGH-RESOLUTION BATHYMETRY AND LONG-TERM STORAGE VARIATIONS

A Dissertation

by

YAO LI

Submitted to the Office of Graduate and Professional Studies of
Texas A&M University
in partial fulfillment of the requirements for the degree of

DOCTOR OF PHILOSOPHY

Chair of Committee,	Huilin Gao
Committee Members,	Gretchen Miller
	George Allen
	Chenghai Yang
Head of Department,	Robin Autenrieth

August 2020

Major Subject: Civil Engineering

ABSTRACT

Reservoirs play a significant role in water management, with functions related to water supply, hydropower generation, flood protection, and biodiversity conservation. To operate reservoirs efficiently for maximum benefit, it is essential to monitor their characteristics and states. Satellite remote sensing provides the unique advantage of observing reservoirs from space. In this dissertation, a series of algorithms was developed to generate high-resolution 3-D bathymetry maps and long-term storage records at a global scale, which can support a variety of applications such as global hydrological modeling and local water resources related studies. These algorithms and datasets are presented through the following three studies:

(1) In the first study, an algorithm was developed to generate 3D reservoir bathymetries by combining elevations collected by the Ice, Cloud, and Land Elevation Satellite (ICESat-2) airborne prototype with area values from Landsat-based water classifications (from 1982 to 2017). Validations over four transects of Lake Mead show R^2 values ranging from 0.82 to 0.99 and Root Mean Square Error (RMSE) values from 1.18 m to 2.36 m. It is expected that the newly launched ICESat-2 should enable the derivation of bathymetries over an unprecedented number of reservoirs.

(2) The bathymetry generation algorithm was then applied to satellite altimetry and imagery observations to generate a global dataset for 347 global reservoirs. This dataset represents a total volume of 3123 km^3, accounting for 50% of the global reservoir capacity. Validations over 20 reservoirs indicate that the dataset has an overall good

accuracy. It suggests that this approach can also be applied to small reservoirs (with surface areas of a few square kilometers or less) and natural lakes.

(3) In the last study, multi-source remote sensing data—in combination with an improved area-depth-storage database—were used to estimate the monthly storage variations for 7245 reservoirs globally from 1999 to 2018. Results show that there is an overall continuous increase of global reservoir total storage at a rate of 27.44 ± 0.96 km^3/yr, which is attributed to the construction of new dams. However, the reservoir normalized storage shows a significant decrease. It is found that reservoir storage variations are very sensitive to climate variability, especially for reservoirs in South America and Africa.

ACKNOWLEDGEMENTS

First of all, I would like to express my most sincere gratitude to my advisor, Dr. Huilin Gao, for her support, guidance, patience, and encouragement during my doctoral study. I wholeheartedly appreciate the freedom she gave me to do the research I am interested in. This dissertation would not have been possible without her continuing support. What I learned from her will benefit my academic career and personal life.

My sincere gratitude also goes out to my committee members, Dr. Gretchen Miller, Dr. George Allen, and Dr. Chenghai Yang, for their valuable support and constructive suggestions throughout my dissertation research. I am so thankful to my group members for their help and support. I will never forget the happiness they brought into my life. I also want to thank all the co-authors for their time and efforts during the publication process.

Thanks also go to my friends and colleagues and the department faculty and staff for making my time at Texas A&M University a great experience.

Last but not least, many thanks to my wife, parents, and relatives for their encouragement, support, and love.

CONTRIBUTORS AND FUNDING SOURCES

This work was supervised by a dissertation committee consisting of Dr. Huilin Gao [advisor] and Dr. Gretchen Miller of the Department of Civil and Environmental Engineering, Dr. George Allen of the Department of Geography, and Dr. Chenghai Yang of the U.S. Department of Agriculture. All other work conducted for the thesis (or) dissertation was completed by the student independently.

My graduate study was supported by the NASA Science of Terra, Aqua, and Suomi NPP (TASNPP) Program under Grant 80NSSC18K0939, and in part by the Gulf Research Program Early-Career Research Fellowship to Huilin Gao at Texas A&M University (project number 2000007265) and the ICESat-2 Early Adopter Program. I was also partially supported by the Troy Marceleno ’60 Fellowship from the Department of Civil and Environmental Engineering, Texas A&M University.

TABLE OF CONTENTS

Page

LIST OF FIGURES

Page

LIST OF TABLES

Page

1. INTRODUCTION

With the ongoing rapid population growth and socio-economic development, the demand for fresh water is continually increasing (Cook and Bakker 2012). It is reported that over 2 billion people are experiencing high water stress, and about 4 billion people are suffering severe water scarcity for more than one month each year (WWAP 2019). Future water security can be further exacerbated by prolonged droughts under a changing climate (Seckler et al. 1999; Zhao et al. 2018). Serving as a buffer against climate extremes, numerous reservoirs have been constructed to facilitate water supply, flood control, and hydropower generation (Cheng et al. 2008; Fu 2008; Grigg 1996; Lehner and Döll 2004; Li et al. 2010; Moy et al. 1986). Meanwhile, reservoirs constitute an essential component of global hydrological and carbon cycles (Falkowski et al. 2000; Mulholland and Elwood 1982), as well as climate regulation (Oki and Kanae 2006; Tranvik et al. 2009). Given the fact that reservoir observations and characteristics are rarely shared at a large scale (Zhang et al. 2014), reservoir information inferred from satellite remote sensing is especially valuable.

To operate reservoirs efficiently for maximum benefit, it is essential to monitor their characteristics and states. Bathymetry, which characterizes the underwater topography, provides information critical for all aspects of reservoir management (Lakewatch 2001). Through a bathymetric map, key parameters related to reservoir system functions (e.g., surface area, volume, maximum length and width, and shoreline length) can be calculated. More importantly, reservoir bathymetry is a required input for

hydrodynamic circulation and water quality models—which are used for supporting navigation, routing, dredging planning, and sedimentation analysis (Hell et al. 2012). At the global scale, spatially explicit knowledge of reservoir bathymetries (and their associated parameters) is crucial for the understanding and modeling of Earth system processes and their interactions with the environment (Messager et al. 2016; Yigzaw et al. 2018).

Water retained by global reservoirs have long term impacts on global and regional water cycles (Zhou et al. 2016). However, gauge observations for reservoir storages are still lacking, and are not always shared. Additionally, because reservoir operation rules are not publicly available, reservoirs have not been implemented in hydrological models in an operational manner at a large scale. A historical long-term record of reservoir storage can not only improve our understanding about the roles of reservoirs in altering the hydrological cycle, but can also help calibrate and validate reservoir operation rules incorporated into models. Since the early 1990s, satellite radar altimeters have been utilized to measure the water levels of large lakes and reservoirs (Birkett 1994). Recently, more studies have focused on generating consistent satellite-based reservoir storage estimations using elevation and area data collected from multiple sensors (Busker et al. 2019; Crétaux et al. 2011; Gao et al. 2012; Zhang and Gao 2016). Although Gao et al. (2012) generated a 19-year reservoir storage dataset representing 15% of the total global capacity and Busker et al. (2019) evaluated the storage variation for 137 lakes from 1984 to 2015, long-term storage records for more reservoirs are critically needed for water management applications across scales.

In summary, it is essential to acquire high-resolution 3-D reservoir bathymetry information and long-term storage records at a global scale for supporting various applications—especially with ongoing climate change and the escalating water crisis. Therefore, the overarching objective of this dissertation is to develop novel algorithms to leverage existing satellite data for breaking the key barriers with regard to generating reservoir bathymetry information and estimating reservoir storage variations. To achieve this goal, three scientific questions will be answered specifically:

(1) Can we derive 3-D reservoir bathymetry by combining satellite imagery and altimetry data?

(2) How can we generate high-resolution 3-D reservoir bathymetry at a global scale with observations collected from existing satellite data?

(3) With the ongoing climate change and the escalating water crisis, what are the long-term variations of reservoir storage at river basin, continental, and global scales?

In order to answer the above questions, the structure of this dissertation progresses from the development of an algorithm to generate 3-D reservoir bathymetry by combining satellite altimetry and imagery data (Chapter 2), to extending this method to the global scale to develop the first consistent high-resolution 3-D reservoir bathymetry dataset (Chapter 3), and then to leveraging long-term satellite observations to estimate storage variations for global reservoirs (Chapter 4).

In Chapter 2, a novel algorithm was developed and tested using the ICESat-2 airborne prototype, the Multiple Altimeter Beam Experimental Lidar (MABEL), with Landsat-based water classifications (from 1982 to 2017). MABEL photon elevations were

paired with Landsat water occurrence percentiles to establish the Area-Elevation (A-E) relationship, which in turn was applied to the percentile image to obtain partial bathymetry over the historic dynamic range of reservoir area. The bathymetry for the central area was projected to achieve the full bathymetry. The bathymetry image was then embedded onto the Digital Elevation Model (DEM) to replace the constant values for waters. Results were validated over Lake Mead against survey data. Validations over four transects show Coefficient of Determination (R^2) values from 0.82 to 0.99 and Root Mean Square Error (RMSE) values from 1.18 m to 2.36 m. In addition, the A-E and Elevation-Volume (E-V) curves have RMSEs of 1.56 m and 0.08 km^3, respectively. Over the entire dynamic reservoir area, the derived bathymetry agrees very well with independent survey data, except for the highest and lowest percentile bands. With abundant overpassing tracks and high spatial resolution, the newly launched ICESat-2 should enable the derivation of bathymetry over an unprecedented number of reservoirs.

In Chapter 3, a 30 m resolution bathymetry dataset was generated for 347 global reservoirs, representing a total volume of 3123 km^3 (50% of the global reservoir capacity). First, A-E relationships for the identified reservoirs were derived by combining altimetry data from multiple satellites with Landsat imagery data. Next, the resulting A-E relationships were applied to the Surface Water Occurrence (SWO) data from the European Commission Joint Research Centre (JRC) Global Surface Water (GSW) dataset to obtain bathymetry values for the dynamic areas of the reservoirs. Lastly, an extrapolation method was adopted to help achieve the full bathymetry dataset. The remotely sensed bathymetry results were primarily validated against the following: (1)

They were validated against A-E and E-V relationships derived from the *in situ* elevations and volumes for 16 reservoirs, with root-mean-square error (RMSE) values of elevation from 0.06 m to 1.99 m, and normalized RMSE values of storage from 0.56% to 4.40%. (2) They were also validated against survey bathymetric maps for four reservoirs, with R^2 values from 0.82 to 0.99 and RMSE values from 0.13 m to 2.31 m. The projected portions have relatively large errors and uncertainties (compared to the remotely sensed portions) because the extrapolated elevations cannot fully capture the underwater topography. Overall, this approach performs better for reservoirs with a large dynamic area fractions. It can also be applied to small reservoirs (e.g., reservoirs with surface areas of a few square kilometers or less), where ICESat observations are available, and to large natural lakes. With the contribution of ICESat-2, this dataset has the potential to be expanded to thousands of reservoirs and lakes in the future.

In Chapter 4, long-term Landsat observations were used to estimate the monthly storage variations for 7245 global reservoirs from 1999 to 2018. For each reservoir, the A-V relationship was either derived from the 3-D bathymetry using a remote sensing method or estimated through an improved simulation method. Validation over 277 reservoirs indicates that the storage estimates have an overall good agreement with *in situ* observations, with the bathymetry based method performing better than the simulation method. Next, storage variations were evaluated across the global, continental, and river basin scales. Results show an overall continuous increase in global reservoir total storage at a rate of 27.44 ± 0.96 km^3/yr, which is primarily attributed to the construction of new dams. This storage growth is primarily because of Asia (20.53 ± 0.73 km^3/yr), which

accounts for about 75% of the global increase. Meanwhile, the reservoir normalized storage—which is defined as the ratio of the actual storage to the storage capacity—was used to evaluate the relative storage variations. A significant decrease of the normalized storage suggests that global reservoirs are experiencing water shortages. Moreover, the response of global reservoirs to climate variability—using the El Niño-Southern Oscillation (ENSO) as an indicator—was evaluated across spatial scales. Results suggest that reservoir storage is negatively correlated to ENSO, which explains the decrease of reservoir normalized storages in South America and Africa. Lastly, the storage variations were evaluated in terms of reservoir functions. Results show that reservoirs with a hydropower purpose have a relatively high normalized storage, and are more sensitive to ENSO. The normalized storages of water supply reservoirs have declined considerably, correlating with the increasing water stress seen under growing municipal water demand.

2. DERIVING HIGH-RESOLUTION RESERVOIR BATHYMETRY FROM ICESAT-2 PROTOTYPE PHOTON-COUNTING LIDAR AND LANDSAT IMAGERY*

2.1. Introduction

Knowledge of bathymetry (i.e. underwater topography) is critical for the understanding and accurate modeling of many lake, reservoir and river processes including surface water and energy exchanges, circulation, stream discharge, and biogeochemical cycles (Heathcote et al. 2015; Mishra et al. 2010; Mohammed and Tarboton 2011). Lake bathymetries and their associated storage levels can significantly influence local and regional weather (Dutra et al. 2010; Rouse et al. 2005; Samuelsson et al. 2010), despite lakes and reservoirs covering only 2.4% of all continents (Lehner and Döll 2004). Although lake and reservoir models have been coupled to weather models (such as the European Centre for Medium-Range Weather Forecasts' Integrated Forecasting System), to incorporate heat storage effects (Balsamo et al. 2012) lake and reservoir depth and surface area are treated as static due to the lack of bathymetry information. Considering the large variations of lake and reservoir extent (and therefore depth) (Pekel et al. 2016), a more dynamic representation of lakes and reservoirs is required in weather forecast models. Furthermore, water retained by reservoirs has long term impacts on the hydrological systems over most large river basins (Chao et al. 2008;

*Reprinted from IEEE Transactions on Geoscience and Remote Sensing, Volume 57, Yao Li, Huilin. Gao, Michael F. Jasinski, Shuai. Zhang, and Jeremy D. Stoll, "Deriving HighResolution Reservoir Bathymetry from ICESat-2 Prototype Photon-counting Lidar and Landsat Imagery", Pages 7883-7893, Copyright (2019), with permission from IEEE

Lehner et al. 2011a; Lettenmaier and Milly 2009; Nilsson et al. 2005). Although reservoirs have been explicitly represented in an increasing number of large scale hydrological models and Earth System Models (Döll et al. 2009; Haddeland et al. 2006; Hanasaki et al. 2006; Voisin et al. 2017; Zhou et al. 2016), the bathymetry in these models has virtually always been oversimplified. For instance, Hanasaki et al. (2006) simulated reservoir release amount while assuming a constant surface area. This directly inhibits the ability of simulating daily streamflow in a manner suitable for global flood forecasting (Zajac et al. 2017). Within individual reservoirs, bathymetry is a required input for hydrodynamic circulation and water quality models—which are used for supporting navigation, routing, dredging planning, and sedimentation analysis (Hell et al. 2012).

Despite its importance, spatially explicit knowledge of reservoir bathymetry (and the associated parameters) is crucially lacking at a global scale (Messager et al. 2016). Bathymetry is typically mapped through surveys with echo-sounding equipment, airborne lidar, and optical imaging sensors (Gao 2009). The echo-sounding method is highly accurate but inefficient and expensive (Odhiambo and Boss 2004). Airborne lidar using high energy sensors can penetrate through relatively deep waters (up to tens of meters depending on the water clarity) with high accuracy (Hilldale and Raff 2008), but it is relatively expensive for rivers and limited by swath width (Gao 2009), preventing its application at larger scales. Over the Alaska North Slope, Saylam et al. (2017) used airborne lidar to map the bathymetry of thousands of small shallow lakes. While more cost-effective for lakes and reservoirs, optical sensing is limited by water depth and optical properties (Wang and Philpot 2007). It further requires simultaneous *in situ* observations,

whose spatial distributions and reliability affect bathymetric accuracy. More recently, some global datasets have emerged that use alternative approaches to infer lake and reservoir geometry information, but they are insufficient for providing high-resolution 3-D bathymetry data that are locally practical. For instance, lake bathymetry information derived from the ETOPO1 Global Relief Model (Amante 2009) has been used in climate modeling (Kourzeneva et al. 2012), but it is only applicable to large lakes and reservoirs (e.g., the Great Lakes) due to its coarse resolution (1 arc-minute). Yigzaw et al. (2018) developed a global storage-area-depth dataset that used an optimal geometric shape for each reservoir—but this dataset does not provide the 3-D bathymetry information. Tseng et al. (2016) projected the underwater slope using the Digital Elevation Model (DEM) data above the water surface and combined this approximated bathymetry with Landsat area to estimate water elevation variations at the Hoover Dam. Although the resultant water surface height was verified by *in situ* data, the accuracy of their projected bathymetry was not directly evaluated. Both HydroLAKES (Messager et al. 2016) and the Global Reservoir and Dam database (GRanD) (Lehner et al. 2011a) only provide the mean depth of reservoirs—which is inadequate to generate storage-area-depth relationships. Indeed, the bathymetry problem is essentially an elevation measurement problem. The fast growth of space-borne radar altimetry has potential use for deriving reservoir bathymetry, though current studies are mainly focused on the derivation of area-volume-elevation relationships (Crétaux et al. 2016; Crétaux et al. 2011; Zhang et al. 2017a). More recently, Getirana et al. (2018) combined the time series radar altimetry and Landsat data to derive the 3-D bathymetry of the lower portion of Lake Mead. This method is potentially

applicable only to large bodies where elevation observations from radar altimeters are available (Gao 2015).

Thus, the objective of this study is to explore the potential of generating high-resolution reservoir bathymetry at a global scale using the data collected by the photon-counting lidar onboard the new Ice, Cloud, and Land Elevation Satellite (ICESat-2). As the first satellite laser ranging altimeter, ICESat collected elevation data with an approximately 70 m footprint and 170 m along-track spacing, which has been widely used for measuring lake and reservoir levels (Phan et al. 2012; Zhang et al. 2011) and calculating the Area-Elevation (A-E) relationship (Zhang et al. 2014). ICESat-2 decreases the footprint and along-track spacing to 14 m and 0.7 m, respectively, thereby improving its capability to obtain high-quality bathymetric information. Recent analysis of airborne Multiple Altimeter Beam Experimental Lidar (MABEL) observations over several inland water bodies indicates that ICESat-2 can penetrate the water to more than 10 meters, depending on water quality (Jasinski et al. 2016). In this study, a novel algorithm is developed to derive bathymetry by combining one transect of MABEL airborne elevation data with historic series Landsat image classifications. As the prototype of ATLAS on ICESat-2, MABEL can retrieve surface elevation values with a mean precision of approximately 5–7 cm (Jasinski et al. 2016). By relating the MABEL data to the water occurrence percentile images from Landsat, the 3-D bathymetry can be derived. With the launch of ICESat-2 in September 2018, this algorithm holds great promise for generating bathymetry for global reservoirs with areas as small as several square kilometers.

2.2. Data and Methods

2.2.1. Data

The generation of the bathymetry results in this study relied on information from two data sources: Landsat and MABEL. From 1982 to 2017, Landsat Thematic Mapper (TM), Enhanced Thematic Mapper Plus (ETM+), and Operational Land Imager (OLI) images (at a spatial resolution of 30 m) were obtained from the United States Geological Survey (USGS) (https://earthexplorer.usgs.gov/). A total of 410 high-quality images, completely free of cloud contamination, were collected over the Lake Mead area (Table 2.1).

Table 2.1 Specification of Landsat images used to generate the water occurrence percentile image

Satellite	Sensor	Band	Period	Number
Landsat-4	TM	NIR (760 nm – 900 nm)	1982–1992	6
Landsat-5	TM	NIR (760 nm – 900 nm)	1984–2011	293
Landsat-7	ETM	NIR (770 nm – 900 nm)	1999–2003	63
Landsat-8	OLI	NIR (851 nm – 879 nm)	2013–2017	48

MABEL elevation data were collected over Lake Mead on February 24, 2012, with reported clear sky conditions and a relatively low water turbidity of 1.6 NTU (Jasinski et al. 2016). The flight overpassed the western part of Lake Mead in a southwest to northeast direction (Figure 2.1a). MABEL collected data over a ~2 m footprint along its track using the same 532-nm photon-counting lidar as ATLAS. Figure 2.1b shows the profile of the MABEL track, with the red dots indicating the samples used (in this study) to establish the A-E relationship. The information from the captured photons was then processed to generate an elevation dataset with an average segment length of 50 m. Because the original MABEL data were referenced to the WGS84 ellipsoid datum, they were converted to the

EGM96 geoid so that the final bathymetry could be merged with the Shuttle Radar Topography Mission (SRTM) DEM data properly. Given a specific location, the EGM96 geoid height (N) can be calculated using the latitude and longitude information via the online tool provided by the National Geospatial-Intelligence Agency Office of Geomatics (http://earth-info.nga.mil/GandG/wgs84/gravitymod/egm96/intpt.html). Then, the orthometric height with respect to the EGM96 geoid (H) (at the given location) can be calculated as the difference between the WGS84 ellipsoid height h (i.e., MABEL reported elevation) and the EGM96 geoid height (N).

The SRTM 1 arc-second (~30 meters) elevation data were obtained from the USGS EarthExplorer website (https://earthexplorer.usgs.gov/). As the first near-global high-resolution DEM (from 56° S to 60° N), the SRTM dataset has been widely used in various research fields (including geology, geomorphology, glaciology, and hydrology) (Bailey et al. 2007; Wright et al. 2006; Yang et al. 2011). However, because the radar signal cannot penetrate through water—and because the SRTM data were only collected once—reservoir bathymetry information below the water level at the SRTM acquisition time cannot be accessed. More recently, Yamazaki et al. (2017) developed a high-accuracy global DEM database with 3 arc-second (~90 meters) resolution. Still, this dataset cannot provide elevation information below the water surface.

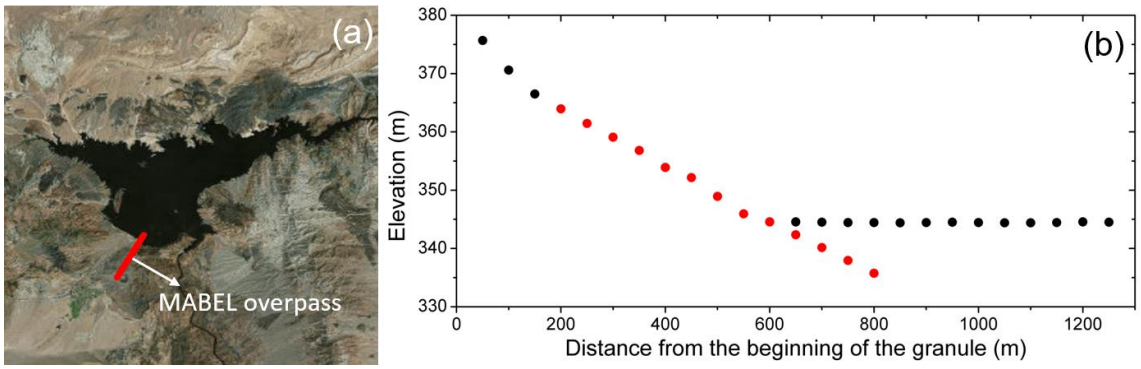

Figure 2.1 (a) Location map and (b) elevation profile of the MABEL samples. The points in (b) represent the samples collected by MABEL. Those in red are the samples used in this study to establish the Area-Elevation (A-E) relationship.

The Lake Mead lidar survey data collected by the United States Bureau of Reclamation (USBR) in 2009 were used to validate the part of the bathymetry product which was generated using MABEL data. This dataset provides detailed elevation contour values for the emergent shoreline areas of Lake Mead, and it covers an area of 445.48 km^2 with elevation values ranging from 334.06 m (1096 feet) to 374.90 m (1230 feet) at a 0.61 m interval (2 feet). For validation purposes, the lidar contours were converted to elevation point values and then resampled to the bathymetry values at a resolution of 30 m using the Inverse Distance Weighted (IDW) interpolation method to match the resolution of the resultant bathymetry. In addition, the contour data—with an elevation interval of 10 m, collected by the 2001 sedimentation survey—were used to validate the projected portion of the bathymetry.

2.2.2. Methods

This reservoir bathymetry generation algorithm contains three main steps (Figure 2.2). First, a water occurrence percentile image was generated for Lake Mead using Landsat image classifications over the lake's historic dynamic elevation variation range.

The occurrence percentile essentially provides the bathymetry contours over the reservoir dynamic area. Second, MABEL elevation data were paired up with the water occurrence percentile image to establish the A-E relationship, which was then used to identify and assign elevation values to the contours. Third, the A-E relationship was applied to the percentile image to obtain the bathymetry for the dynamic reservoir area—which was then used to project the bathymetry for the central area. The full bathymetry was then embedded onto the SRTM data to replace the constant DEM value.

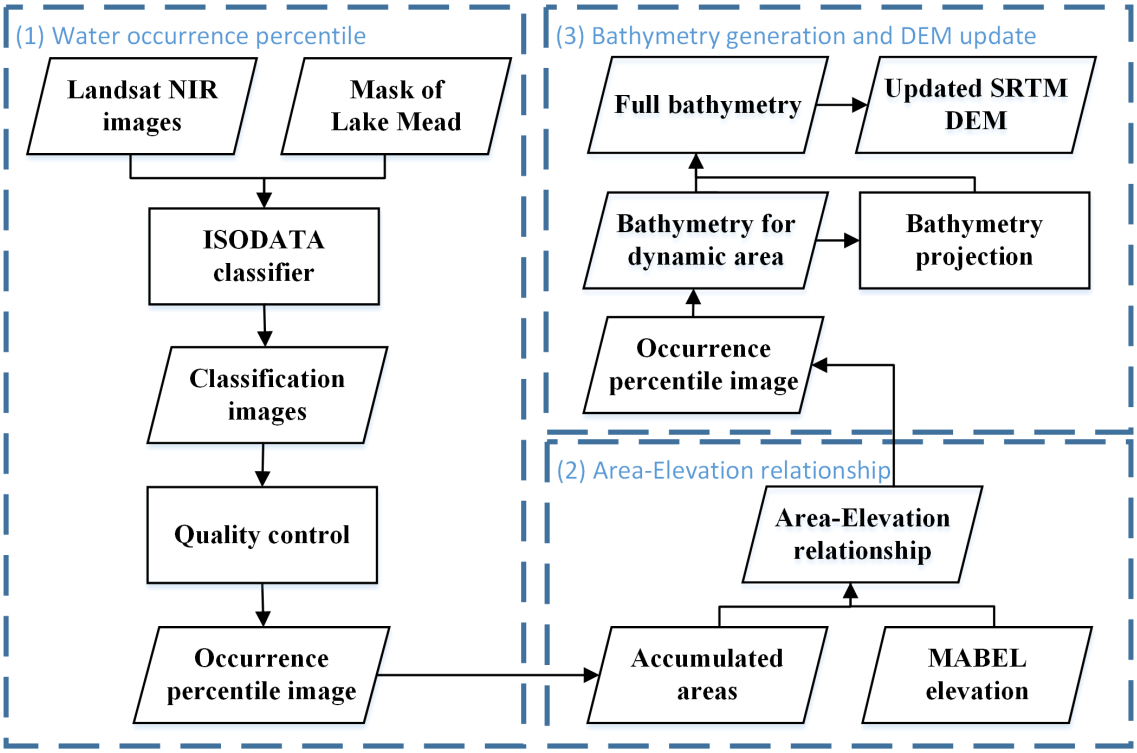

Figure 2.2 Flowchart of the bathymetry generation algorithm. It consists of three parts (separated by the blue boxes): (1) The water occurrence percentile image was generated from the Landsat classifications, which essentially provided the bathymetry contours; (2) The Area-Elevation (A-E) relationship was established by combining the area from the occurrence percentile image with MABEL elevation values. This was then used to identify and assign elevation values to the contours; (3) The A-E relationship was applied to the percentile image to obtain the bathymetry for the dynamic lake area, which was used to project the bathymetry for the central area to obtain the full lake bathymetry. Then, the full bathymetry was overlapped with the SRTM DEM data to replace the constant value.

2.2.2.1. Water occurrence percentile

The water occurrence percentile image shows the frequency at which each pixel is classified as water, which can be calculated as the ratio of the time classified as water vs. the total observation time. The percentile image can characterize the elevation gradients and act as the base map of the bathymetry (Zhao and Gao 2018).

To obtain the water occurrence percentile image, the water classifications were first conducted by applying the Iterative Self-Organizing Data Analysis Techniques Algorithm (ISODATA) (Melesse and Jordan 2002; Ren et al. 2008) to the 410 Landsat Near-infrared (NIR) images collected over Lake Mead from 1982 to 2017. NIR was selected because it is strongly absorbed by water but barely absorbed by terrestrial vegetation and dry soil (McFeeters 1996). Compared to the methods that involve using water indexes—such as the Normalized Difference Water Index (NDWI) (McFeeters 1996)—the unsupervised ISODATA technique has the advantage of producing consistent water classifications without having to choose a threshold based on water body and season (Li and Sheng 2012; Zhang et al. 2017b). To reduce the computation cost and enhance the classification accuracy, a mask was constructed by buffering 10 km of the Lake Mead shapefile. The classification process was performed within the masked area of each image. However, some of the Landsat images were also contaminated by mountain shadows. Lake Mead is partly surrounded by mountain ranges, such as the River Mountains and the Muddy Mountains (the portion within the Boulder Basin). Due to the effect of satellite incident angle, mountain shadows may appear in some images—and these images are very likely to be misclassified as water bodies. To correct this, any water pixel in the water

classification image which has an elevation value greater than 400 m was reclassified as land. A water occurrence percentile image was then created for Lake Mead. To reduce the impacts of random errors, pixels with occurrence values less than 1% were removed from the percentile image.

2.2.2.2. Area-Elevation (A-E) relationship

The A-E relationship is an essential element of the bathymetry retrieval algorithm. A-E relationships vary with water body and have been used as the key function for calculating storage values from either surface area values or elevation values (Crétaux et al. 2016; Gao et al. 2012; Zhang et al. 2017a). To derive the A-E relationship for Lake Mead, MABEL elevation points were projected onto the occurrence percentile image, with each point corresponding to a specific percentile value—each of which could be regarded as a contour. The corresponding water area within that specific contour was then calculated. As shown in Jasinski et al. (2016), MABEL photons penetrated the water body to about 9.2 m of depth. These elevation measurements (below the water surface) were also paired up with the occurrence percentile image, which allowed for four more samples for deriving the A-E relationship (Figure 2.1b). Figure 2.3 suggests that the resulting Lake Mead A-E relationship is very robust (with an R^2 value of 0.98).

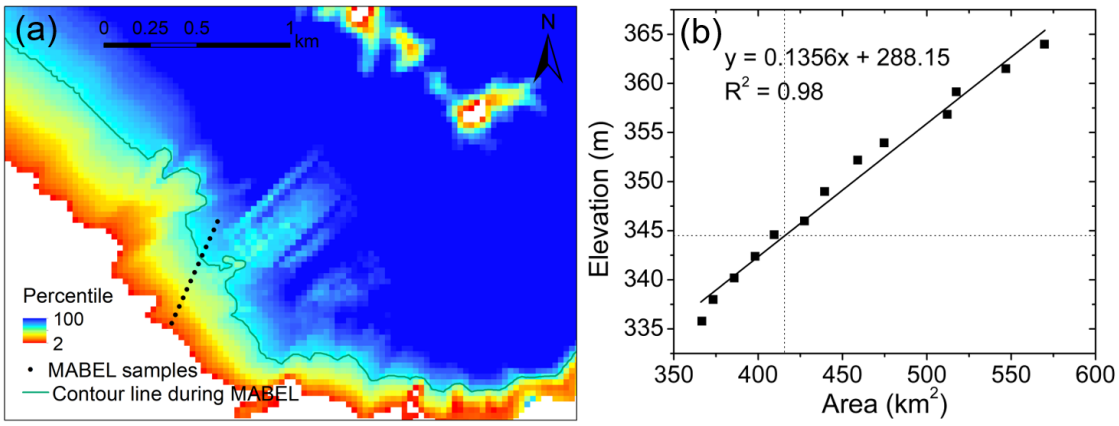

Figure 2.3 (a) The locations of the MABEL samples and (b) the Area-Elevation (A-E) relationship of Lake Mead.

2.2.2.3. Bathymetry generation and SRTM DEM update

The elevation at each percentile contour was determined by applying the A-E relationship to the area enclosed by that contour. Because the water occurrence percentile image is based on 35 years of Landsat classifications, this procedure led to a full dynamic range of bathymetry values. For the central reservoir area, the Tseng et al. (2016) algorithm was adopted to project the part of bathymetry not accessible by MABEL and Landsat. In Tseng et al. (2016), an algorithm was developed to extend the part of Lake Mead bathymetry not measured by SRTM DEM using the elevation information of the surrounding land area. They projected the bathymetry with an elevation range from 320 m to 372 m. In this study, we applied the Tseng et al. (2016) algorithm to extrapolate our remotely sensed partial bathymetry (from MABEL and Landsat) into a bathymetry containing the central reservoir area. We modified the Tseng et al. (2016) algorithm by utilizing the storage capacity information to determine the reservoir bottom level. The cumulative storage associated with the n^{th} contour from the bathymetry was estimated using equation (2.1):

$$V_n = V_c - \sum_{i=1}^{n} \frac{(h_{i+1} - h_i)(A_{i+1} + A_i)}{2} \quad (2.1)$$

where V_c represents the storage at capacity and n is the number of contours below the capacity elevation (h_c). V_c and h_c were obtained from surveying data provided by the USBR, and the area at capacity (A_c) was obtained by applying h_c to the A-E relationship. A_i is the entire water surface area enclosed by the i^{th} contour, which corresponds to the elevation h_i. Thus, the storage value corresponding to each contour was obtained. At the end of each projection step, we calculated the cumulative storage from all contours. When the cumulative storage reached the reservoir capacity, the projection of bathymetry was terminated.

By combining the remotely sensed and projected bathymetry, the full bathymetry was obtained. This was then embedded onto the SRTM DEM dataset to replace the constant value. We calculated the elevation value associated with the reservoir area that corresponded to the constant DEM value using the MABEL-based A-E relationship. Then the elevation difference between this elevation value and the constant DEM value was used to correct the bathymetry data. It is worth noting that our bathymetry data has a higher accuracy than the DEM data, and the purpose of the correction is simply to keep the DEM data consistent.

2.2.2.4. Validation scheme

This study used the USBR lidar survey and sedimentation survey datasets to validate the bathymetry product. The lidar survey—which is of high resolution and quality but only available along the coast—was adopted for evaluating the part of bathymetry

directly derived from remotely sensed data. First, four transects from the north, south, west, and east regions were selected across the shorelines of Lake Mead. The elevations of these transects from this study were compared with their counterparts from lidar. To further evaluate the performance of the remotely sensed bathymetry over the entire reservoir, we divided the percentile image into ten bands (at a 10% increment) and compared the elevation statistics within each band (i.e., we compared the mean and standard deviation). This can better scrutinize which parts (higher or lower elevation zones) tend to have larger/smaller errors (e.g., standard deviations, overestimations vs. underestimations). It should be noted that the evaluated variable is the elevation, not the percentile. In addition, indirect validations were conducted over the full bathymetry by comparing our results for the A-E and Elevation-Volume (E-V) relationships with their counterparts from the lidar and sedimentation survey datasets. The A-E and E-V relationships based on lidar and sedimentation data were provided by the United States Bureau of Reclamation (USBR 2008, 2011). Equation (2.1) is used to calculate the storage from the bathymetry data, from which the E-V relationship can be derived.

The sedimentation data were primarily used for evaluating the projected part of the bathymetry. Because the contour data provided by the USBR (with an elevation interval of 10 m) are not continuous, it is difficult to directly use this dataset to validate the bathymetry values. Thus, we first visually compared the contours generated from the projected bathymetry with the survey contours. Although the bathymetry contours from the sedimentation survey are fragmental, USBR did provide a look-up table detailing the A-E and E-V relationships (USBR 2008, 2011). Thus, we compared these reported

relationships with those from this study to quantify the overall performance of the projected bathymetry.

2.3. Results

2.3.1. Bathymetry results

For the remotely sensed bathymetry values, the elevation range is from 330.62 m to 369.65 m, which corresponds to a water surface area from 313.20 km^2 (inner zone) to 601.05 km^2 (outer zone), representing 58% of the reservoir capacity. When the SRTM DEM data were collected in February 2000, the reservoir area was about 587.50 km^2 with a constant elevation value (372 m), which means that no bathymetry information was acquired below the water surface. In comparison, our remotely sensed results can provide additional reservoir bathymetry information associated with an additional 274.30 km^2 (47%) of reservoir area.

The remotely sensed bathymetry (for the entire reservoir area, with three sub-regions zoomed in upon) is shown in Figure 2.4. Overall, the bathymetry has evident gradients, which are in agreement with the surrounding terrain of Lake Mead. For the western region (Figure 2.4b), the bathymetry has steep elevation gradients across the shorelines, and the shapes of islands within this area are clearly captured. For the northern region (Figure 2.4c), the gradients are gradual, indicating that this part of the reservoir is relatively flat as compared to the western part. As shown in Figure 2.4d, the topography near the Colorado River has been clearly captured.

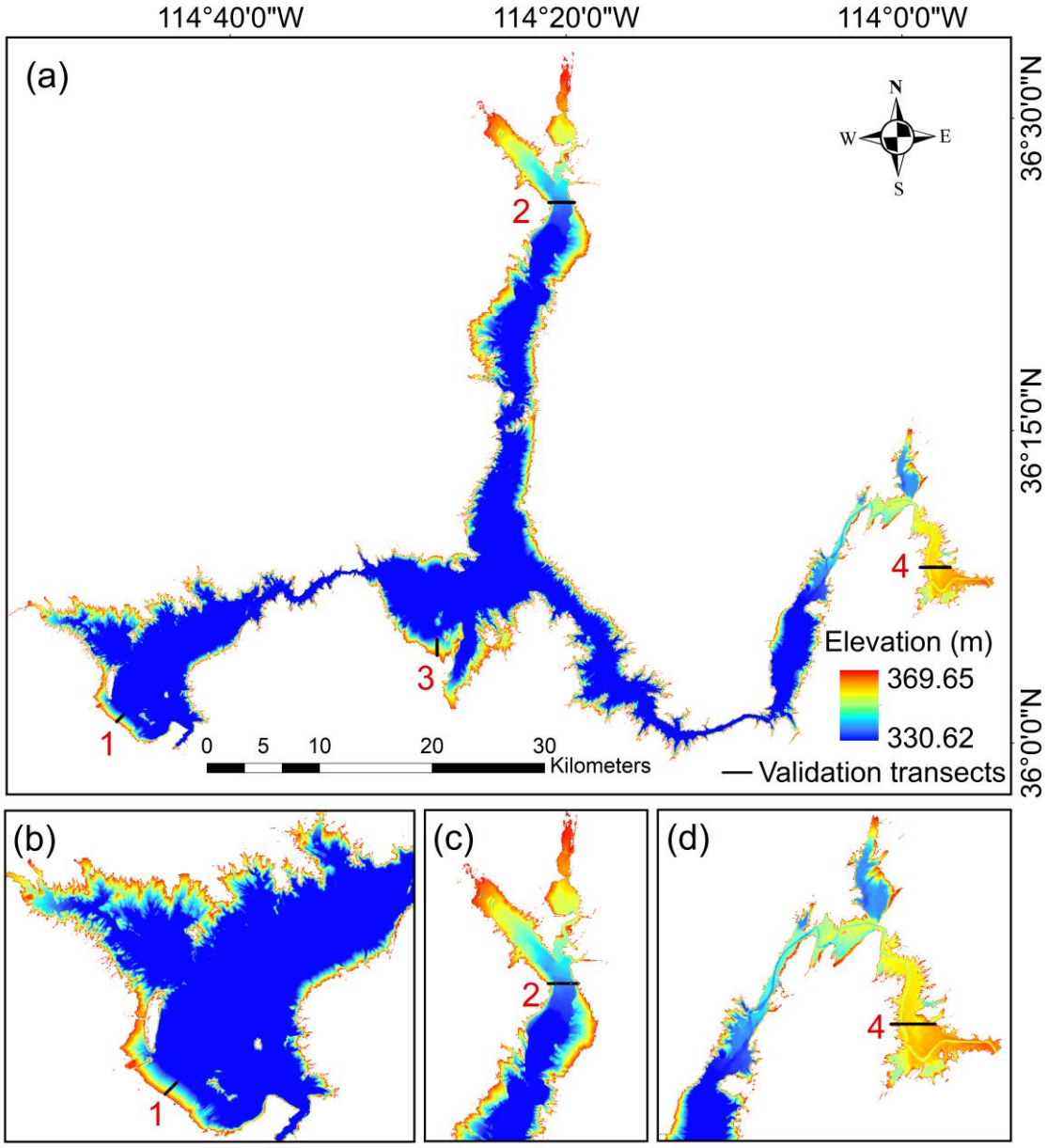

Figure 2.4 The remotely sensed bathymetry of Lake Mead: (a) Overall bathymetry; (b-d) close up views of three sub-regions: (b) the west, (c) the north, (d) the east. The transects labeled 1 to 4 consist of points which are used for validation purposes.

Based on the Tseng et al. (2016) method, we projected the bathymetry for the central area, which ranges from 263.00 m to 330.62 m. The lowest elevation value (263.00 m) was determined by using the storage information calculated after equation (2.1). We

calculated the storage for each contour layer (from outer to inner) and accumulated them. When the elevation is at 263.00 m, the accumulated storage reached the capacity value and we thus ended the projection. Figure 2.5a shows the full bathymetry of Lake Mead, including the remotely sensed part (330.62 m - 369.65 m) and the projected part (263.00 m - 330.62 m). Although the performance of the projected bathymetry varies with region, it has an overall good pattern. Close up views of two regions were selected to show the details. In the subset area shown in Figure 2.5b, the contours based on the projected bathymetry agree well with those from the sedimentation survey data. However, in the sub-domain depicted by Figure 2.5c, the projected results largely missed those from the survey—which was caused by the assumption made in Tseng et al. (2016) that the slope remains constant. The resultant full bathymetry was then embedded onto the SRTM DEM data. The comparison between the bathymetry and SRTM DEM is shown in Figure 2.6. It is evident that the elevation of Lake Mead from DEM is constant (372 m) over the entire reservoir. In order to be accurate, we first applied the reservoir area from the DEM (587.50 km^2) to the MABEL-based A-E relationship to estimate its corresponding elevation (367.82 m). A systematic bias of 4.18 m was found between this elevation value and that according to the SRTM DEM. A bias correction of 4.18 m was then applied to the bathymetry such it can be seamlessly combined with the DEM. Thus, the part of the DEM with a constant value of 372 m was replaced by the part of the bathymetry results representing 372 m and below (after the systematic bias correction). Moreover, contour maps with different horizontal intervals (e.g., 5 m, 10 m, and 20 m) were drawn from the

bathymetry, which can help to delineate the profile. An example of the contour map at a 20 m interval is shown in Figure 2.6.

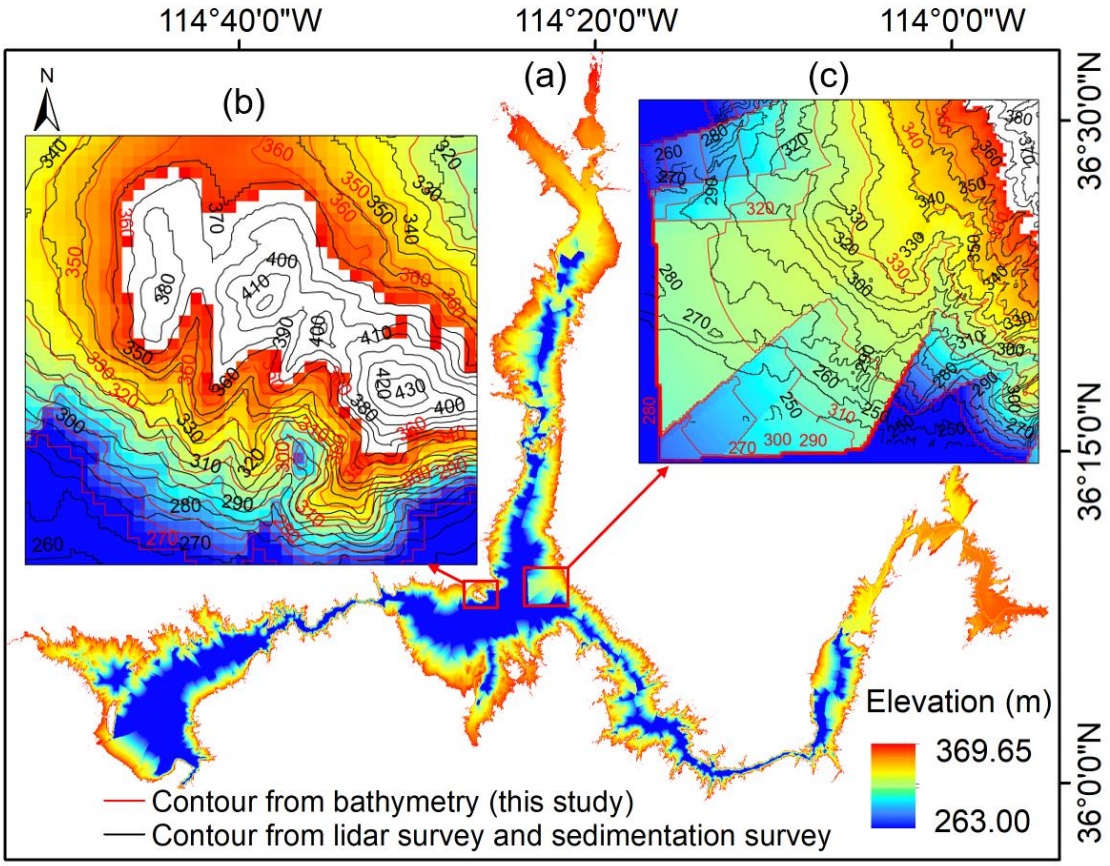

Figure 2.5 (a) Full bathymetry of Lake Mead, including the remotely sensed bathymetry (330.62 m - 369.65 m) and the projected bathymetry (263.00 m - 330.62 m). Close up views of two regions with (b) satisfactory and (c) unsatisfactory performances are selected to show the details. Note that the contour data from both sources have an elevation interval of 10 m. The contour data are not shown in (a) because they are relatively dense and would not be useful to the reader.

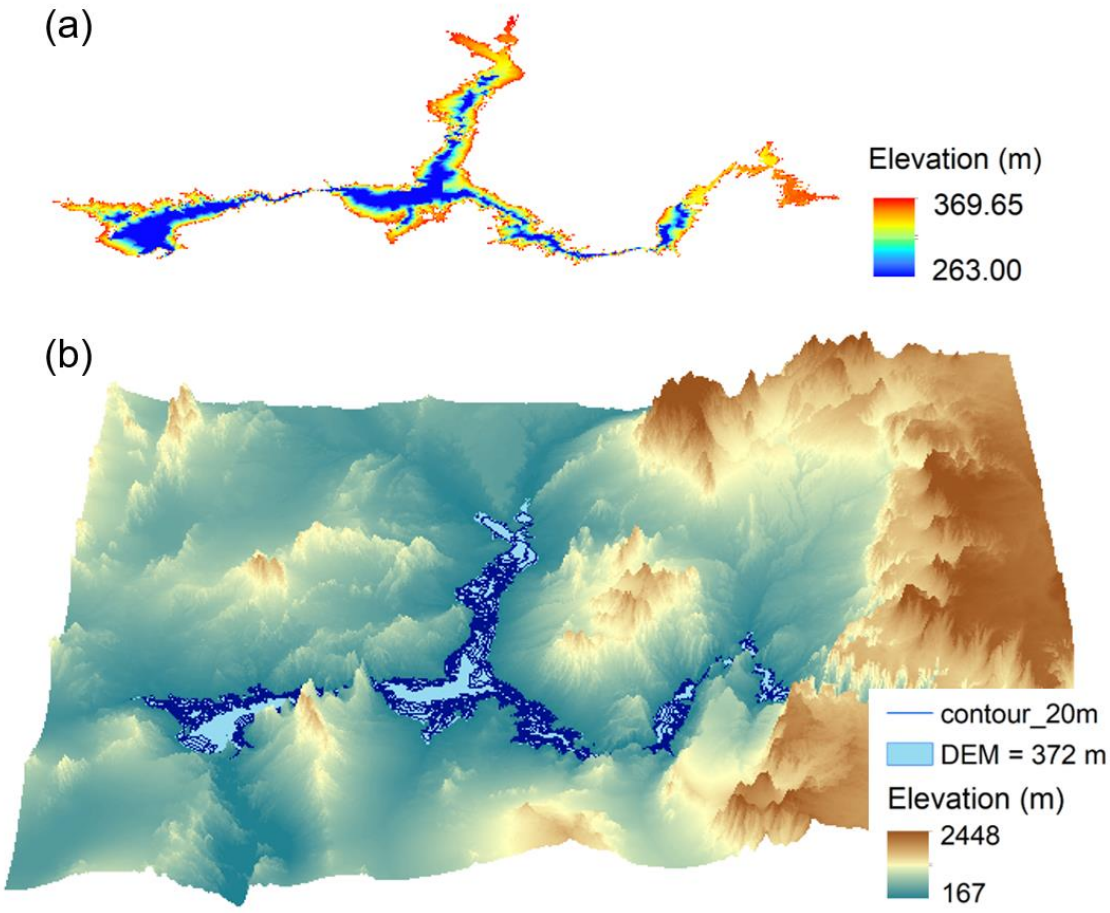

Figure 2.6 (a) Full bathymetry and (b) SRTM DEM data over Lake Mead. The contour map (with a 20 m interval) is derived from the bathymetry information, and the DEM elevation is constant (372 m) over the entire lake.

2.3.2. Validation of the bathymetry

The remotely sensed bathymetry product was validated using survey lidar data by comparing elevation values over selected transects and over the entire reservoir (by percentile band). Moreover, the full bathymetry was indirectly validated by comparing the A-E and E-V curves from this study with those derived from the sedimentation survey.

First, for the remotely sensed bathymetry, the elevations at four representative transects (whose locations are shown in Figure 2.4a) were evaluated. The elevation

profiles and scatter plots for these four transects using the data from this study (and the lidar data) are shown in Figure 2.7 and Figure 2.8, respectively. The estimated elevations show a good correlation with those from the lidar survey, with R^2 values of 0.99, 0.99, 0.98, and 0.82 for Transects 1 to 4, respectively. The corresponding Root Mean Square Error (RMSE) values are 2.36 m, 1.18 m, 2.35 m, and 1.54 m. The statistical results of these four transects are shown in Table 2.2. In addition, the Colorado River bottom can be clearly observed from the east transect profile (Figure 2.7d). In contrast, the river bottom according to the lidar measurements appeared to be flat. The three outliers appearing in Figure 2.8d are due to the disagreement over the Colorado bottom, which leads to the relatively low R^2 for this transect. Overall, the results indicate that the bathymetry product has relatively high accuracy.

Table 2.2 Statistical results of MABEL and lidar elevations for the validation transects

ID	Elevation data	Max (m)	Min (m)	Mean (m)	SD (m)	N	R^2	RMSE (m)	P-value
1	MABEL	366.73	334.95	349.17	9.71	20	0.99	2.36	4.62×10^{-19}
	lidar	368.81	334.67	351.02	10.77				
2	MABEL	368.86	337.24	342.23	8.46	76	0.99	1.18	7.49×10^{-72}
	lidar	368.24	335.89	341.96	9.05				
3	MABEL	368.60	336.31	351.30	8.75	49	0.98	2.35	2.95×10^{-42}
	lidar	369.42	334.67	353.17	9.48				
4	MABEL	367.75	348.40	358.27	2.80	87	0.82	1.54	6.82×10^{-33}
	lidar	368.24	345.79	358.03	3.48				

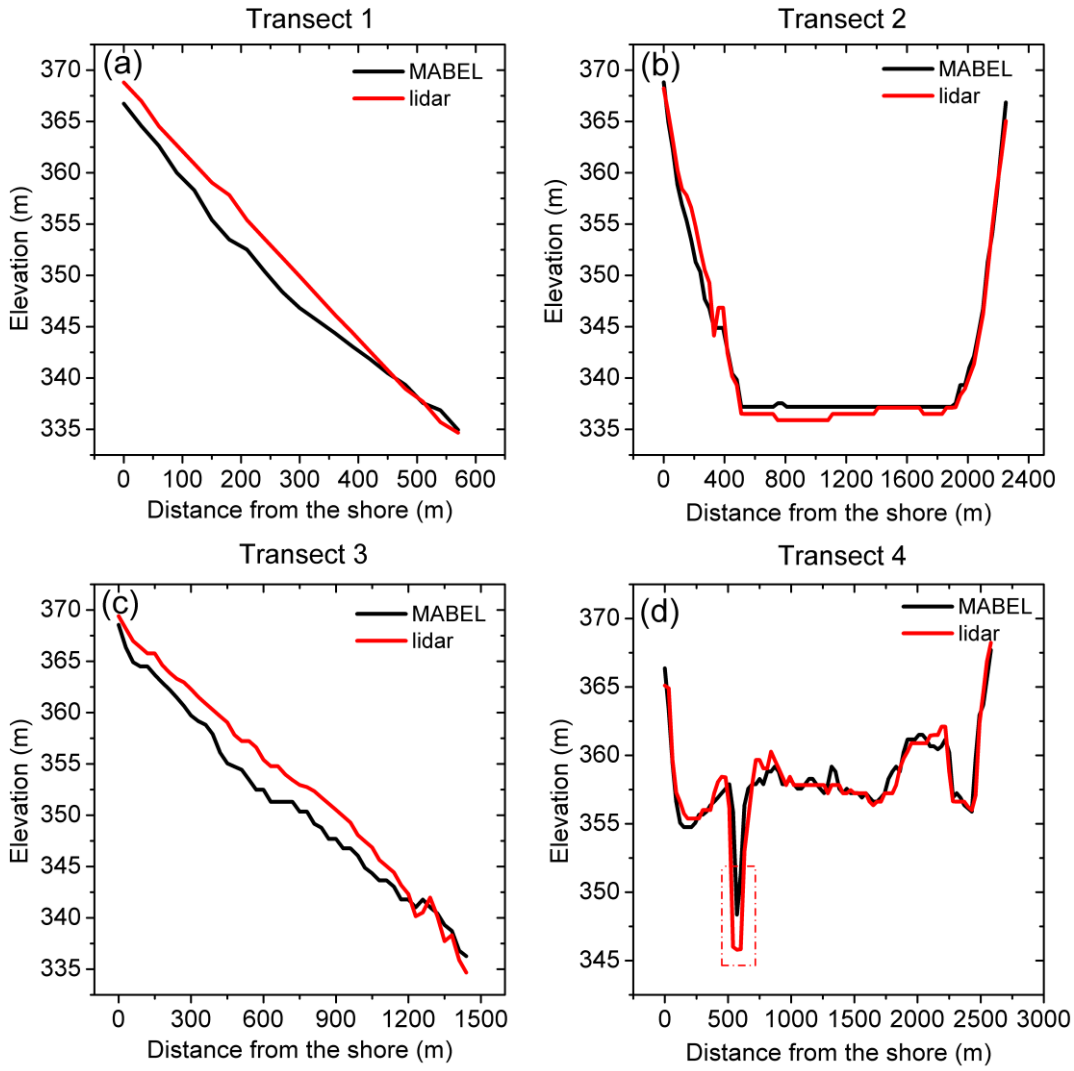

Figure 2.7 Elevation profiles for the four validation transects: (a) Transect 1 as shown in Figure 2.4, in the west part of Lake Mead, from southwest to northeast, (b) Transect 2 as shown in Figure 2.4, in the north part of Lake Mead, from west to east, (c) Transect 3 as shown in Figure 2.4, in the south part of Lake Mead, from south to north, and (d) Transect 4 as shown in Figure 2.4, in the east part of Lake Mead, from west to east.

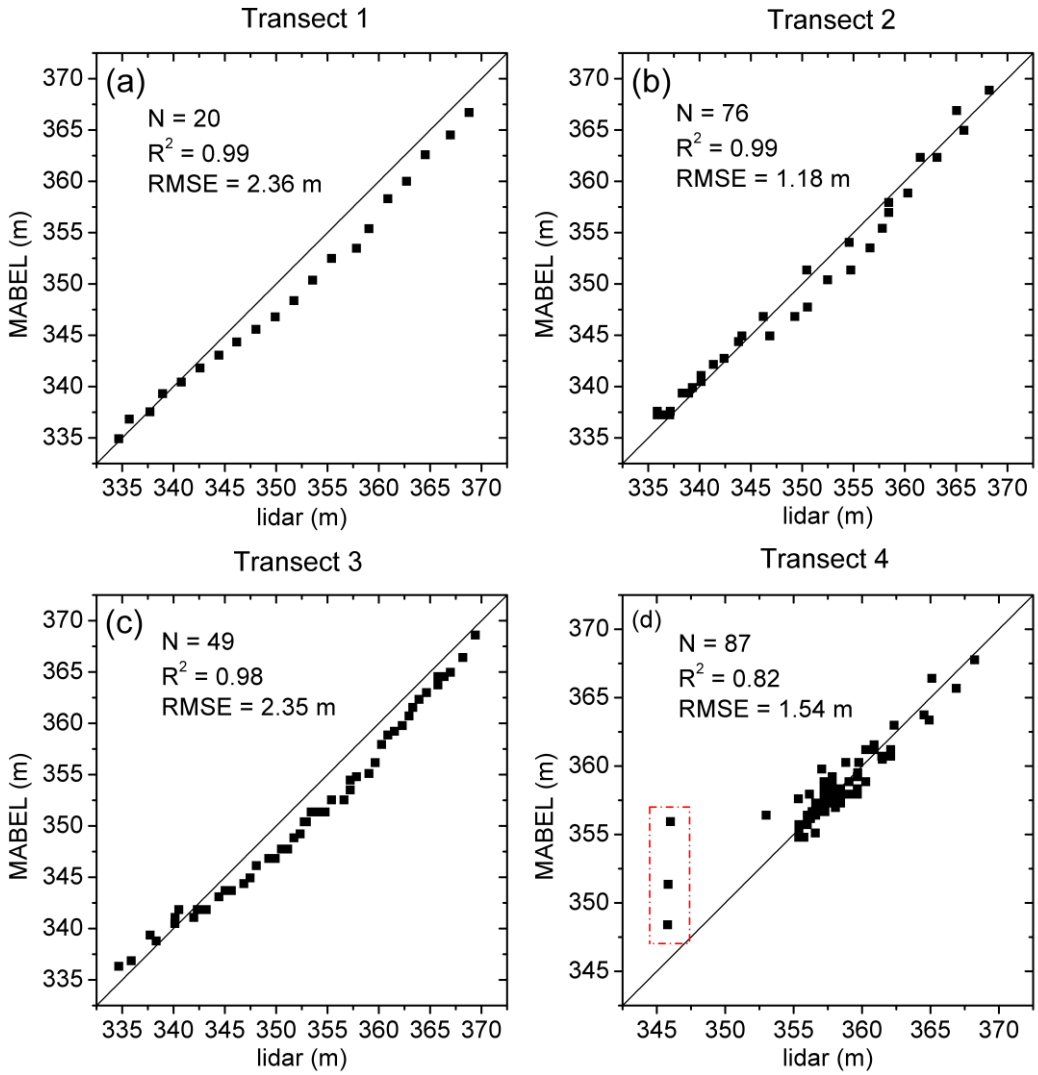

Figure 2.8 Scatter plots of the four validation transects: (a) Transect 1 as shown in Figure 2.4, in the west part of Lake Mead, from southwest to northeast, (b) Transect 2 as shown in Figure 2.4, in the north part of Lake Mead, from west to east, (c) Transect 3 as shown in Figure 2.4, in the south part of Lake Mead, from south to north, and (d) Transect 4 as shown in Figure 2.4, in the east part of Lake Mead, from west to east.

Figure 2.9 compares the statistical results of the elevations from the bathymetry obtained from this study with that obtained from the lidar survey within each percentile band (at a 10% interval). Although there is a clear overestimation in the 1-30% range and an underestimation in the 80-100% range, the derived bathymetry overall agrees very well with the lidar survey data. The survey data show a larger variation within each band, which

can be attributed to both the higher resolution and the measurement error of the raw data. However, it is unclear why the survey elevations in the 90-100% band are higher than those in the 80-90% band.

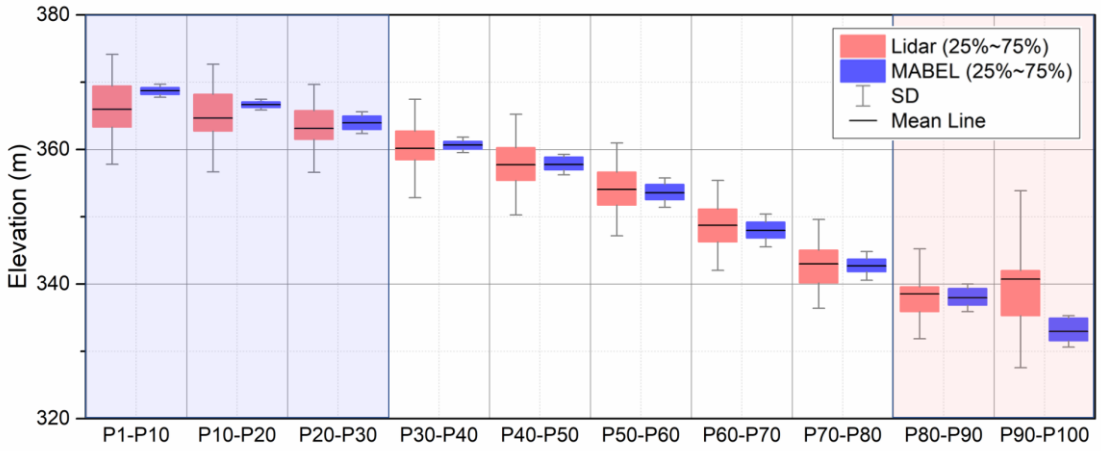

Figure 2.9 Comparisons of the statistical results of the elevations within each percentile band (at a 10% interval) over the entire lake area. For the 1-30% range, the mean elevation is overestimated by MABEL, whereas it is underestimated for the 80-100% range.

In addition, we also quantified the uncertainties of the remotely sensed bathymetry. Since the penetration depth of MABEL elevation measurements depends on the water conditions, we changed the number of underwater pairs used in the A-E relationship and calculated the uncertainties of the retrieved elevations. The resultant uncertainties are from -1.39 m (when the penetration depth was 9.2 m) to 1.30 m (when the penetration depth was 0 m), showing that our results are reliable.

Second, the A-E relationship—the critical factor affecting the reliability and accuracy of the bathymetry data—was examined to indirectly validate the product. Although the MABEL based A-E relationship appears to be more linear than the one from lidar, it has shown good overall consistency with the latter (with an R^2 of 0.99 and an RMSE of 1.56 m) (Figure 2.10a). With regard to the A-E relationship from the projected

bathymetry, although it has a good correlation with the A-E relationship from the sedimentation survey data (R^2 = 0.99), the vertical bias is relatively large (RMSE = 4.78 m). The survey reservoir storage values at each contour elevation were also utilized in the validation. Based on the elevation values and their corresponding areas from the bathymetry, the storage values can be calculated using equation (2.1). Figure 2.10b shows the E-V curves derived from the bathymetry and the survey lidar and sedimentation data. By comparing the E-V relationships between remotely sensed bathymetry and lidar survey data (with an R^2 of 1.00 and an RMSE of 0.08 km^3), it is evident that they are in very good agreement. Whereas for the comparison of the E-V relationships between the projected bathymetry and the sedimentation survey data, they have a good consistency (R^2 = 1.00) but a large vertical mismatch (RMSE = 1.05 km^3).

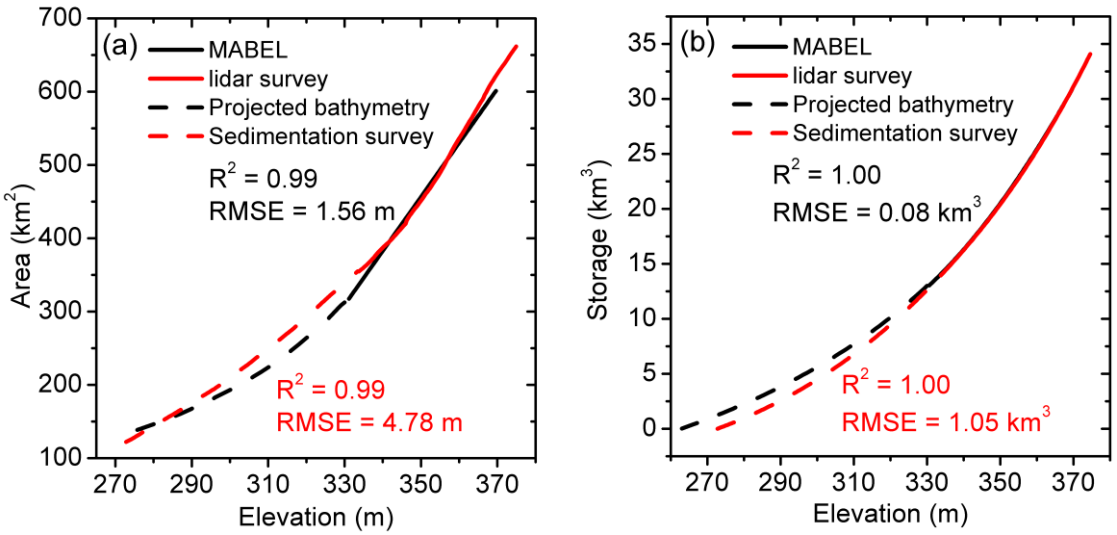

Figure 2.10 Comparison of (a) the Area-Elevation (A-E) relationship and (b) the Elevation-Volume (E-V) relationship for Lake Mead. The MABEL based A-E and E-V relationships were compared with those from the lidar survey (with statistical values labeled in black), and the A-E and E-V relationships derived from projected bathymetry were compared with those from the sedimentation survey (with statistical values labeled in red).

2.4. Discussion and Conclusions

Although ICESat-2 is a follow-on mission to ICESat, it differs from its predecessor in its reliance only on the 532 nm wavelength and photon-counting detector technology. These two features allow for both light penetration into the subsurface, and the high spatial resolution required for bathymetric sampling. The analysis of MABEL data in the current Lake Mead test case is thus not only representative of ICESat-2, but any future satellite lidar possessing a 532 nm wavelength with photon-counting technology.

This study is the first attempt to improve the process of measuring reservoir bathymetry using ICESat-2 data and has the potential of generating bathymetry for global reservoirs when ICESat-2 ATLAS data become available. With high vertical precision (5-10 cm per 100-m segment length), a small along-track sampling interval (0.7 m), a small footprint diameter (17 m), and narrow horizontal track spacing (three sets of beam pairs; 90 m between each neighboring pair, 3 km between each pair set) (Markus et al. 2017), ATLAS is expected to capture the topography around numerous inland water bodies with areas as small as a few tenths of a square kilometer. Figure 2.11 shows the ICESat-2 ground tracks over selected regions during two years. Over the Tibetan Plateau, even the smallest lake (0.4 km^2) reported by HydroLAKES—a global digital map database for lakes with surface areas greater than 10 ha— would have four overpasses. For lakes and reservoirs larger than 1 km^2, there are usually multiple tracks (for instance, there are 14 tracks over the Timnath Reservoir). A total of 423 tracks are found in two years for Lake Mead, as compared to 52 ICESat overpasses (from 2003 to 2009) and 119 radar altimeter overpasses (with five satellite radar sensors considered from 2000 to 2014). Particularly,

the spatial resolution and vertical precision of ICESat-2 are significantly better than those of ICESat and radar altimeters. Thus, ICESat-2 has a unique advantage for reducing the errors and uncertainties of the future bathymetry product.

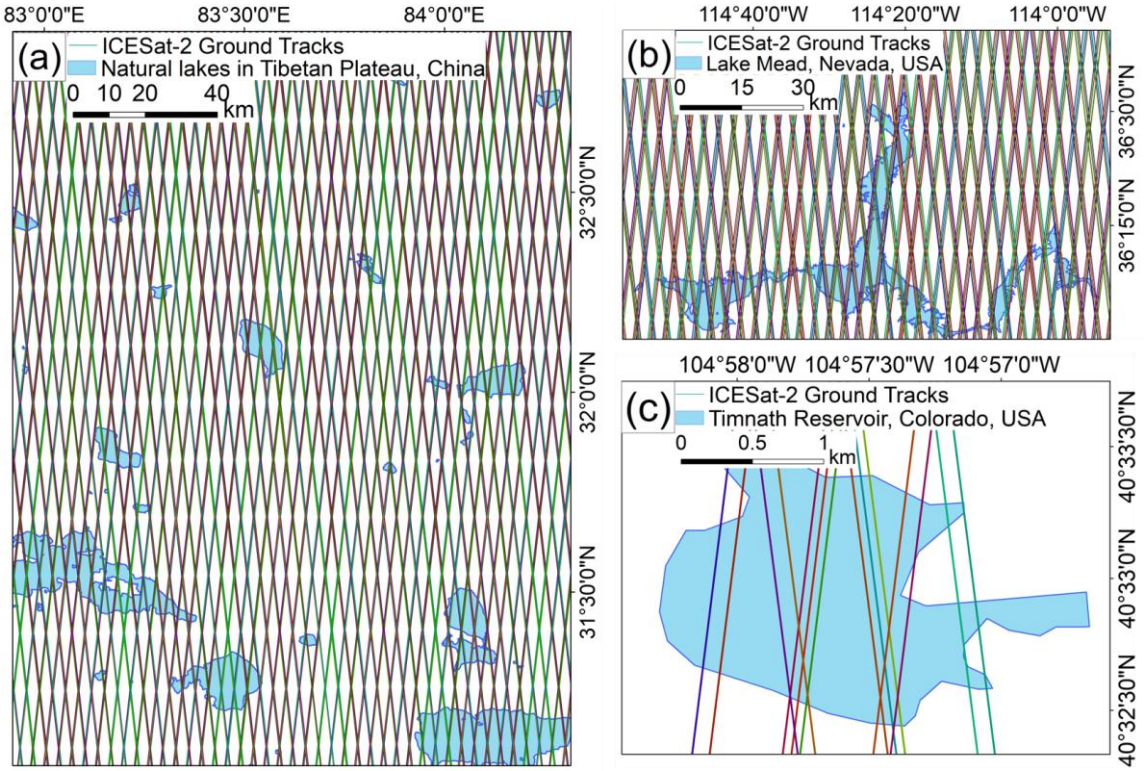

Figure 2.11 ICESat-2 ground tracks for (a) some natural lakes in the Tibetan Plateau, China (0.4 km^2< area < 498.06 km^2); (b) Lake Mead, Nevada, USA (area=580.95 km^2); and (c) the Timnath Reservoir, Colorado, USA (area=2.33 km^2). The line colors represent the different tracks from the different passes. ICESat-2 ground tracks were downloaded from https://icesat-2.gsfc.nasa.gov/science/specs

Previous studies have shown that the photon counting MABEL system can profile the subsurface light attenuation—depending on pulse strength, water clarity, and atmospheric conditions—down to about one Secchi disc depth (SDD) under clear skies (Jasinski et al. 2016). The 2012 experiment over Lake Mead, which exhibited a low turbidity of 1.6 NTU, was flown during clear night skies with low backscatter, resulting

in a penetration of 9.2 meters. Other water bodies with higher turbidity and less favorable meteorological conditions would exhibit less penetration. As shown in this study, the underwater elevation samples collected by MABEL have an added value to improve the elevation range of the resulted bathymetry (through a more accurate A-E relationship). It is true that the water clarity may not be ideal during every ICESat-2 overpass, and for some reservoirs the water clarity is always low. However, for the reservoirs where the laser cannot reach significant depth, the samples across the shoreline area can provide extra data points (because of the high spatial resolution of ICESat-2). For instance, the three highest points in Figure 2.1b actually are within/near Lake Mead's elevation at capacity, even though the percentile image did not cover them since none of the 410 selected Landsat images were collected when the reservoir level was the highest. Furthermore, during the 3-year expected operational life of ICESat-2, we will be able to obtain elevation values from multiple tracks. The minimum elevation to be sampled by each ICESat-2 track depends on both the penetration depth and the water surface level. Because water surface level varies both seasonally and interannually, a good range of nearshore elevation values can be collected from multiple tracks passing over a given reservoir—even for reservoirs with low clarity (penetration). Even if the ICESat-2 observations cannot cover the entire dynamic area of a given reservoir, an extrapolation of the derived A-E relationship using the contour area values of the percentile image (from 35 years of Landsat imagery covering a large range of area dynamics) will lead to a good representation of the reservoir bathymetry. Such bathymetry results can satisfy the demands of most applications (such as hydrologic modeling and reservoir management).

The projected bathymetry results have relatively large uncertainties because this method assumes that the underwater slope remains constant. The method linearly extrapolates the slope of the boundary, which was derived from the nearby grids (3 by 3 window). Therefore, the quality of the data (i.e., the elevation within the 90%-100% percentile) used to calculate the slope determines the performance of the projection. Although the projected bathymetry is not as robust as the remotely sensed bathymetry, it bridges the gap for the area far off the coast and helps to achieve the full bathymetry. The accuracy and uncertainties of the detected reservoir bottom depend on several factors. The first of these involves the errors and uncertainties associated with the capacity values of elevation and storage—which can directly result in biased bottom estimations. The second factor involves the A-E and E-V relationships in both the dynamic portion and the extrapolated portion. On one hand, the extrapolated portion tends to have much larger elevation errors due to the simplified assumption of constant slope. On the other hand, for the same elevation interval, the extrapolated portion is associated with a much smaller volume than that from the upper dynamic part. In this study, because the capacity values were adopted from the USBR, the A-E and E-V relationships performed reasonably well in the dynamic portion (Figure 2.10). Furthermore, the bottom elevation derived from this study (263.0 m) is close to that measured through the sedimentation survey (272.8 m).

The photon-counting lidar based bathymetry product also leads to high-quality A-E relationships, which will contribute to more accurate estimations of reservoir storage variations (when applied to either satellite imagery or altimetry data). Many studies suggest that the R^2 of the A-E relationship directly affects the performance of the

corresponding remotely sensed reservoir storage estimation (Gao 2015; Li et al. 2017; Zhang et al. 2014). A set of comparisons—all using the same Landsat water areas from Zhao and Gao (2018), but different A-E relationships (for Lake Mead)—clearly demonstrate the benefit of accurate elevation measurements (Figure 2.12). We used the RMSE and the standard deviation ratio (Stdev ratio)—the ratio between the standard deviations of estimated and *in situ* reservoir storage time series—to evaluate the storage estimations. By combining radar altimetry data with MODIS based area estimates, the A-E relationship from Gao et al. (2012) has the lowest R^2 value (0.83) and the largest storage estimation error (RMSE = 2.34 km^3, Stdev ratio = 0.73). The poor A-E relationship is mainly attributed to the low resolution of MODIS (250 m). By substituting MODIS with Landsat, the R^2 value of the A-E relationship from Duan and Bastiaanssen (2013) was improved to 0.99, which leads to better storage results (RMSE = 1.24 km^3, Stdev ratio = 0.92). With elevation values obtained from the photon counting lidar, the storage error was further reduced (RMSE = 1.16 km^3) and the Stdev ratio decreased to 0.84. Since the A-E relationships have different slopes and intercepts, each one has its own best-fit spectrum with the *in situ* A-E relationship. Even for the storage estimations using the least accurate A-E relationship from Gao et al. (2012), there is still very good agreement with the *in situ* observations when the area values are within a certain range. This can explain why the performances of the A-E relationships vary with the area values when estimating the storage values. Unlike the other two algorithms—which relied on radar altimetry data collected over multiple years—this algorithm leveraged elevations collected from just a

single lidar track. Using data from multiple ICESat-2 tracks, this algorithm can perform even better.

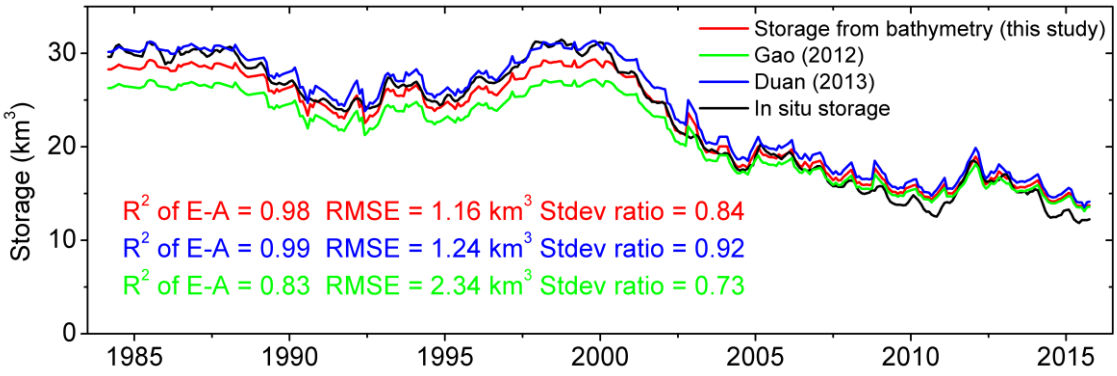

Figure 2.12 Storage estimations of Lake Mead from 1984 to 2015 using different Area-Elevation (A-E) relationships. The time-series surface area of Lake Mead was provided by Zhao and Gao (2018).

More recently, Getirana et al. (2018) derived the bathymetry for the lower portion of Lake Mead. A new contribution they made is to evaluate results from a suite of experiments. For the best performing one, they linearly interpolated the radar altimetry data (from 2002 to 2015) and then paired it up with the Landsat based water extent to obtain the bathymetry (with an elevation range of 23.90 m). By incorporating the gauge-based water levels (from 1983 to 2016), they improved the elevation range to 42.3 m. In comparison, our method generated the dynamic bathymetry at an elevation range of 39.03 m, solely based on remote sensing data (through overlaying a single, high-quality lidar track over the Landsat water occurrence image). To terminate the bathymetry extrapolation, Getirana et al. (2018) used the *in situ* downstream riverbed elevation, while we used the reservoir storage capacity. The use of *in situ* riverbed elevation values may be limited by data availability, but reservoir capacity values can be obtained from the GRanD database (Lehner et al. 2011a). Furthermore, by embedding the bathymetry onto

the SRTM DEM dataset, results from this study may be used to support the mapping and modeling of flood inundation in the vicinity of the reservoir (Moknatian et al. 2017).

This algorithm still has some limitations that need to be addressed. For example, even though the remotely sensed algorithm leverages 35 years of Landsat information to characterize the largest range of reservoir bathymetry values, it is impossible to derive the bathymetry of the very central area that is covered by water all of the time. Known as the "inactive pool", this bottom portion of a reservoir is intended for functions such as sedimentation containment and ecosystem protection (Zhao et al. 2016). Because we projected the bathymetry for the central area to represent the full reservoir, its quality may not satisfy the applications that need high-quality elevations (e.g., navigation). Another concern is the existence of mountain shadow. Many reservoirs are located in mountainous regions, and areas covered by shadows can be easily misclassified as water. Although DEM data can help eliminate the mountain shadow within the masked area, shadows near the boundary can still have a minor impact on the classification result.

In summary, we demonstrate that the 532 nm MABEL elevations and imagery datasets can be combined to generate high-resolution 3D reservoir bathymetry results for the dynamic area over the last three decades. The bathymetry for the central reservoir area can be projected by extrapolation, and then integrated with the remotely sensed results to obtain the full bathymetry. The highlight is that a 30 m resolution and high-quality bathymetry profile representing the complete range of the dynamic reservoir area over more than 30 years (i.e., 58% of Lake Mead's capacity) was produced exclusively from remote sensing data.

Until now, there has been no cost-effective approach to derive reservoir bathymetry at a global scale. This approach was motivated by a need to fill in this gap and to eventually lead to a global bathymetry product suitable for applications across disciplines. It can be immediately usable once the ICESat-2 ATLAS data become available.

3. A HIGH-RESOLUTION BATHYMETRY DATASET FOR GLOBAL RESERVOIRS USING MULTI-SOURCE SATELLITE IMAGERY AND ALTIMETRY*

3.1. Introduction

With ongoing rapid population growth and socio-economic development, the demand for fresh water is continually increasing (Cook and Bakker 2012). It has been projected that two-thirds of the world's population might face water stress by the year 2025. Future water scarcity could be further exacerbated by prolonged droughts under the changing climate (Seckler et al. 1999; Zhao et al. 2018). Serving as a buffer against climate extremes, numerous reservoirs have been constructed to facilitate water supply, flood control, and hydropower generation (Cheng et al. 2008; Fu 2008; Grigg 1996; Lehner and Döll 2004; Li et al. 2010; Moy et al. 1986). Meanwhile, reservoirs constitute an essential component of global hydrological and carbon cycles (Falkowski et al. 2000; Mulholland and Elwood 1982), as well as climate regulation (Oki and Kanae 2006; Tranvik et al. 2009). Given the fact that reservoir observations and characteristics are rarely shared on a large scale (Zhang et al. 2014), reservoir information inferred from satellite remote sensing is especially valuable. To date, the temporal variations of reservoir water elevation, surface area, and storage have been successfully monitored from space at both regional

*Reprinted from Remote Sensing of Environment, Volume 244, Yao Li, Huilin. Gao, Gang Zhao, and Kuo-Hsin Tseng, "A high-resolution bathymetry dataset for global reservoirs using multi-source satellite imagery and altimetry", Pages 1-19, Copyright (2020), with permission from Elsevier

and global scales (Birkett et al. 2011; Busker et al. 2019; Crétaux et al. 2011; Gao et al. 2012; Khandelwal et al. 2017; Yao et al. 2019; Zhang et al. 2014; Zhao and Gao 2018). However, there are no validated datasets for global 3-D lake/reservoir bathymetric maps available within the public domain (Messager et al. 2016), which hampers many water resource related studies and applications.

Bathymetry, which characterizes the underwater terrain, delineates the 3-D features of reservoirs. The development of 3-D reservoir bathymetry is beneficial for multiple applications across different regions at various spatial scales. First, the Area-Volume-Elevation (AVE) relationship, one of the most important physical characteristics of a reservoir, can be derived from bathymetry data. AVE relationships play a key role in modeling hydrological processes, such as inundation mapping (Shin et al. 2019), evaporation loss estimation (Zhao and Gao 2019), sediment deposition estimation (Langland 2009; Rowan et al. 1995), storage monitoring (Gao 2015), and global hydrological modeling (Bierkens et al. 2015). Second, 3-D reservoir bathymetry can help characterize and understand different processes of aquatic systems. Additionally, it has been an essential input for various other purposes, such as circulation and thermal structure modeling (Bai et al. 2013; Beletsky et al. 2006), water quality and hydrodynamic modeling (Lindim et al. 2011; Tufford and McKellar 1999), macrophyte distribution (Britton-Simmons et al. 2012; Lehmann 1998), and phytoplankton prediction (Alex Elliott et al. 2005). Therefore, spatially explicit knowledge of reservoir bathymetry and its associated parameters is of critical importance to understand and model various Earth system

processes, as well as their interactions with the environment (Bierkens et al. 2015; Messager et al. 2016; Wood et al. 2011).

Bathymetry values are typically collected by sedimentation surveys taken with echo sounders (Dunbar et al. 1999), Light Detection and Ranging (lidar) instruments (Hilldale and Raff 2008; Muirhead and Cracknell 1986), and optical remote sensing techniques (Brando et al. 2009; Lafon et al. 2002). However, it is impractical to use these traditional methods to develop a global scale reservoir bathymetry database (Li et al. 2019b). Recent studies have attempted to combine satellite altimetry and imagery data to derive reservoir bathymetries, but these studies have mainly focused on just a few reservoirs. For example, Arsen et al. (2013) used Ice, Cloud, and land Elevation Satellite (ICESat) and Landsat data to derive the bathymetry of Lake Poopó, but the resulting bathymetry dataset was not validated by ground truth data, so the uncertainties associated with the procedure of mesh gridding and interpolation could not be quantified. Tseng et al. (2016) projected the bathymetry of Lake Mead using Digital Elevation Model (DEM) data by extrapolating the slope above the water surface into the underwater area, and then incorporated this with the Landsat-based water surface area to estimate the water level variations from 1984 to 2015. Getirana et al. (2018) evaluated fourteen different approaches to estimate Lake Mead's bathymetry by combining multi-satellite datasets. Li et al. (2019b) developed an algorithm aimed at deriving high-resolution bathymetry by projecting the elevation track collected by the airborne ICESat-2 prototype onto a water occurrence percentile image generated from time series Landsat observations over Lake Mead.

Even though some global databases can provide reservoir geometry information, locally practical 3-D bathymetry data remain unavailable. Global DEM datasets, such as the Shuttle Radar Topography Mission (SRTM) DEM (Farr et al. 2007) and the TanDEM-X DEM (Krieger et al. 2007), can provide detailed terrestrial topography over the Earth's land surface area. However, because radar bands cannot penetrate into water, bathymetry is inaccessible except for cases when the given reservoirs are almost empty or are not yet constructed during the data collection period (Zhang et al. 2016). Yamazaki et al. (2017) corrected multiple height error components from existing DEMs and generated a high-accuracy map of global terrain elevations. However, reservoir bathymetry information is still unattainable using this technique. More recently, Yigzaw et al. (2018) developed a global Storage-Area-Depth dataset for over 6,800 reservoirs using five hypothesized reservoir profile shapes. However, this dataset cannot provide 3-D reservoir bathymetry information, and the accuracy of the Area-Depth relationships is limited by the simplified representation of reservoir profile shapes.

In this study, we leveraged satellite radar and lidar altimetry data in combination with Landsat-based water surface area datasets to generate a remotely sensed high-resolution global reservoir bathymetry dataset. The Surface Water Occurrence (SWO) image provided by the Global Surface Water (GSW) dataset (Pekel et al. 2016) served as the base map for this bathymetry dataset. By incorporating the Area-Elevation (A-E) relationships derived by combining satellite altimetry and imagery observations into SWO images, the bathymetry maps were obtained. When the remotely sensed bathymetry could not represent the full bathymetry in terms of storage capacity, the method of Tseng et al.

(2016) was adopted to project the rest of the bathymetry values. The validation results indicate that the remotely sensed bathymetry values have high accuracy and reliability, while the projected bathymetry values have relatively large uncertainties and errors.

3.2. Data

This study used multiple satellite datasets (summarized in Table 3.1), which can be categorized as satellite altimetry datasets and surface area datasets. These datasets are described in detail in Sections 3.2.1 and 3.2.2, respectively. It should be noted that the water elevation is, hereafter, referred to as elevation.

Table 3.1 Summary of the satellite datasets used in this study

Dataset	Abbreviation	Link	Parameter
Ice, Cloud, and land Elevation Satellite	ICESat	https://nsidc.org/data/icesat/data.html	Water elevation
Global Reservoir and Lake Monitor	G-REALM	https://ipad.fas.usda.gov/cropexplorer/global_reservoir/	Water elevation
Hydroweb	Hydroweb	http://hydroweb.theia-land.fr/	Water elevation
JRC Global Surface Water Dataset	GSW	https://global-surface-water.appspot.com/	Surface Water Occurrence
Global Reservoir Surface Area Dataset	GRSAD	https://doi.org/10.18738/T8/DF80WG	Monthly water area

3.2.1. Satellite altimetry datasets

3.2.1.1. ICESat/GLAS lidar altimetry dataset

The Geoscience Laser Altimeter System (GLAS) aboard ICESat was the first lidar instrument used to measure ice sheet mass balance, cloud and aerosol height, land topography, and canopy characteristics (Schutz et al. 2005). GLAS transmits infrared (1064 nm) and visible (532 nm) laser pulses to measure the distance between the host satellite and the Earth's surface, which is then converted to the elevation of a reference ellipsoid. This instrument was operated in campaign mode from 2003 to 2010, with a 91-

day revisit period. ICESat/GLAS collected elevation data with an approximately 70 m footprint and 170 m along-track spacing. With a much higher spatial resolution than traditional radar altimeters, ICESat is capable of measuring relatively small inland water bodies. Meanwhile, it should be noted that due to some technical issues that affected the laser diode pump arrays shortly after launch, the ICESat mission was re-planned to operate with three campaigns per year to maximize its duration (Schutz et al. 2005), which reduced its duty cycle from 100% to 27% per year (Abshire et al. 2005). This issue, along with its orbital design, led to sparse spatial sampling. This, in turn, led to the few available observations needed to generate the time series, thereby hindering the consistent spatial-temporal observations of global waters (Zhang et al. 2014). In this study, ICESat/GLAS L2 Global Land Surface Altimetry Data version 34 (GLAH14) (Zwally et al. 2011) were acquired for water level measurements.

The ICESat data were processed using the following three steps:

(1) Selection of the reservoirs: Reservoirs recorded in the HydroLAKES database (Messager et al. 2016) with ICESat overpasses were selected.

(2) Creation of the reservoir masks: Polygons of the selected reservoirs were obtained from the HydroLAKES database. As most of the reservoir polygons were generated from the static SRTM, they may reflect a low-fill or dry-season state with smaller area values than the maximum. Therefore, the masks were created using a 1 km buffer to ensure that the maximum extents of the reservoirs were covered. It should be noted that we manually corrected some polygons that were

found to have large discrepancies from Google maps. These alterations are reported in the bathymetry dataset.

(3) Extraction of the elevation values within the reservoir masks: During this process, only the elevations indicated to be of 'good quality' (i.e., with elev_use_flg values of 0) were kept. The raw elevation values were then converted to orthometric heights using the Earth Gravitational Model 2008 (EGM08). This step was repeated for each ICESat overpass from 2003 to 2009.

3.2.1.2. Radar altimetry datasets

Compared to lidar altimeters, radar altimeters use a longer wavelength (i.e., radio waves) to measure the range, which can operate in all weather conditions, both day and night. In this study, the radar altimetry data were adopted from two datasets: G-REALM (Birkett et al. 2011) and Hydroweb (Crétaux et al. 2011).

G-REALM is operated by the U.S. Department of Agriculture (USDA), in cooperation with NASA and the University of Maryland. The dataset contains the water level variation information for 291 (as of June 2019) large global lakes and reservoirs (all with areas greater than 100 km2). It provides near real-time inland water elevation data from the Jason-3 altimetry mission, along with archived data collected since 1992 from the Jason-2/OSTM, Jason-1, Topex/Poseidon, and ENVISAT missions. Depending upon the sensors, the temporal resolutions of these elevation data vary from 10 days to 35 days (Birkett et al. 2011). In this study, we selected the 10-day product because it provides temporally sufficient data and covers more reservoirs. The raw data were converted to orthometric heights with reference to the EGM08 datum using the associated converting

factors. The monthly elevation value was generated by averaging the observations within each month.

The Hydroweb dataset was developed by and is maintained by the Laboratoire d'Etudes en Géophysique et Océanographie Spatiales (LEGOS). At the time of this research, Hydroweb contained time series of water level observations for 155 lakes and reservoirs, as well as for 2810 rivers using 'virtual stations' at a global scale. The water surface elevations, which reference the EGM08 datum, are based on the merged Topex/Poseidon, Jason-1, Jason-2, Jason-3, ENVISAT, and GFO measurements (Crétaux et al. 2011). The elevation observations within each month were averaged to generate the overall monthly values.

3.2.2. Surface area datasets

Two area datasets were used in this study according to the altimetry data source. The first is the SWO image from the GSW by Pekel et al. (2016). Based on the three million Landsat images acquired from 1984 to 2015, GSW quantifies the Earth's surface water's temporal distributions and variations at a 30 m spatial resolution. The SWO image was calculated as the ratio of the times detected as water vs. the total observation times from 1984 to 2015, which represents the frequency that each pixel was classified as water. The SWO is essentially a remotely sensed contour image of a reservoir without the actual elevation assigned to each contour. As ICESat/GLAS can delineate the topography above the water with a high spatial resolution but a low temporal resolution, overlaying all of the ICESat tracks onto the SWO image allows us to take full advantage of the multiple elevation values from each ICESat track. Even though the temporal resolution of Landsat

is relatively low, SWO can capture a large dynamic range of reservoirs due to their interannual and seasonal variations. Using an approach similar to Li et al. (2019b), the SWO contour image was combined with GLAS water elevation values to generate the bathymetry for each of the reservoirs with ICESat overpasses (see Section 3.3.1.1 for details).

The second area dataset contains the time series values from the Global Reservoir Surface Area Dataset (GRSAD) by Zhao and Gao (2018). Built upon the GSW monthly water classifications, GRSAD uses an enhancement algorithm to correct the underestimated reservoir area values in GSW due to contamination from clouds, cloud shadows, and Landsat-7's Scan Line Corrector (SLC) failure. The radar altimetry data can only provide one average elevation value for the entire reservoir at the observation time. However, radar altimeters have relatively higher temporal resolutions over longer periods, which can provide sufficient elevation observations to be paired with area values from the GRSAD time series. For a reservoir with water levels from radar altimeters (reported by G-REALM or Hydroweb), the Area-Elevation (A-E) relationship was first generated by pairing an elevation observation with its corresponding water area (see Section 3.3.1.2 for details).

3.3. Methodology

3.3.1. Bathymetry generation approach

Figure 3.1 shows the flow chart of the reservoir bathymetry approach. During this process, the A-E relationship was the key factor determining the accuracy of the bathymetry product. For reservoirs with ICESat/GLAS overpasses, their elevations were

paired with SWO contour areas to generate a set of A-E relationships. For reservoirs whose elevations were from the G-REALM and Hydroweb radar altimetry datasets, the monthly mean water levels were associated with the monthly surface area values from GRSAD to establish A-E relationships. Then, the A-E relationships were incorporated into the corresponding SWO images to generate dynamic bathymetry data, which represents the extent between the largest and smallest area from 1984 to 2015. Finally, as a last resort, bathymetry projection was carried out when the dynamic part (described above) did not cover the full bathymetry as compared with reservoir capacity (section 3.3.1.3).

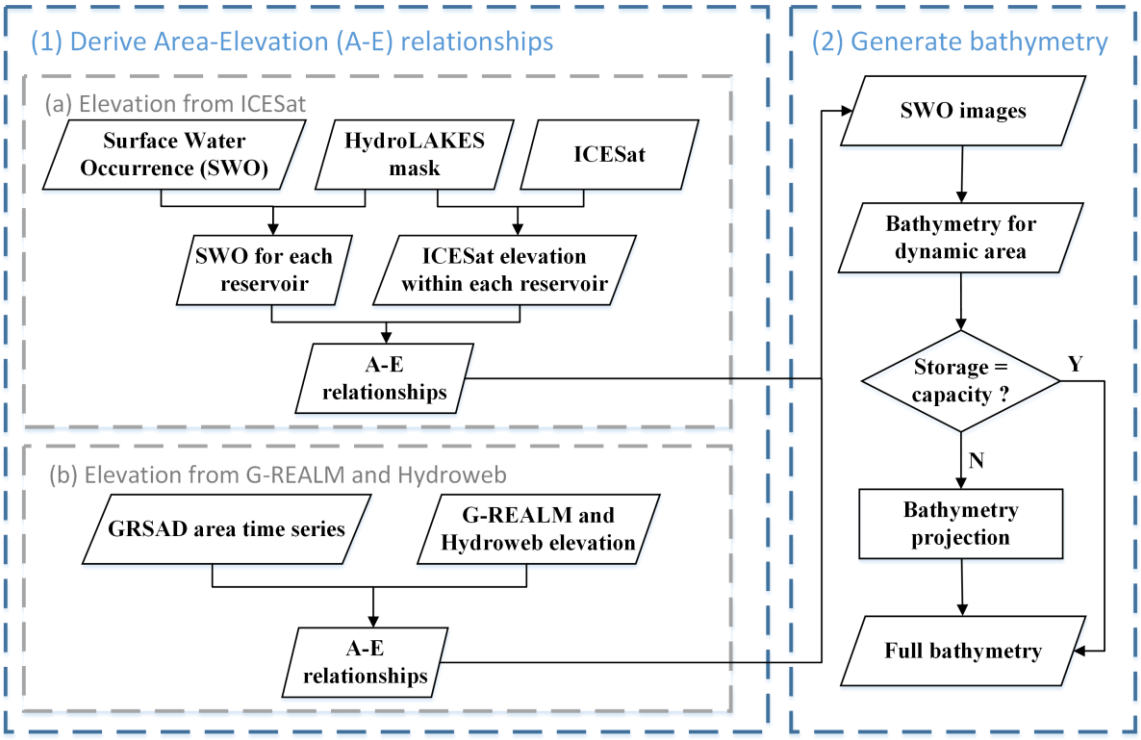

Figure 3.1 Flowchart of the bathymetry estimation algorithm.

3.3.1.1. A-E relationships with elevations from the ICESat database

Because the ICESat data are only available for about 7 years, with a repeat time of 91 days, it is difficult to collect sufficient ‘couplings’ of water elevations and surface areas

to build A-E relationships. To overcome this limitation, an algorithm similar to the one developed by Li et al. (2019b) was adopted. This algorithm can maximize the use of ICESat data by taking advantage of the SWO generated from the 32-year span of Landsat images. For each reservoir, the ICESat elevation samples within the masked area were first projected onto the SWO image. This allowed each sample to correspond to a specific SWO percentile value. The elevation values that were collected over the water surface during an ICESat pass were excluded because they could not reflect the real bathymetry. If one overpass contained less than five valid consecutive elevation values across the SWO of a reservoir, the data collected from this entire overpass would be eliminated. Each elevation value was paired with the area value enclosed by its corresponding percentile (i.e., the contour). Then, the A-E relationship for each reservoir was established through linear regression. By assuming a linear A-E relationship, the reservoir cross-section was a second-order polynomial, which is more realistic than a linear cross-section (Gao et al. 2016). It is worth noting that a non-linear relationship may perform better for some reservoirs, but linear relationships were found to perform well for most of the reservoirs (Busker et al. 2019; Gao et al. 2016; Zhang et al. 2014).

Here, Lake Mead is selected as an example to illustrate the process of deriving the A-E relationship. During the lifetime of ICESat, there were 40 tracks that overpassed Lake Mead, and these were projected onto the SWO image (Figure 3.2). Each elevation sample corresponds to a specific occurrence percentile value, each of which can be regarded as a contour. Only the samples on the terrain slopes were used, which can better represent the contour gradients of the lake. Figure 3.3a shows the elevation profile for one track over

Lake Mead on Oct 21, 2003 (from which, only the samples in solid were selected). The elevations from the selected samples, along with those from other tracks, were combined with their associated contour areas to derive the A-E relationship. Figure 3.3b suggests that the area and elevation values (which range from 346.73 m to 369.20 m) are highly correlated in Lake Mead, with an R^2 value of 0.99.

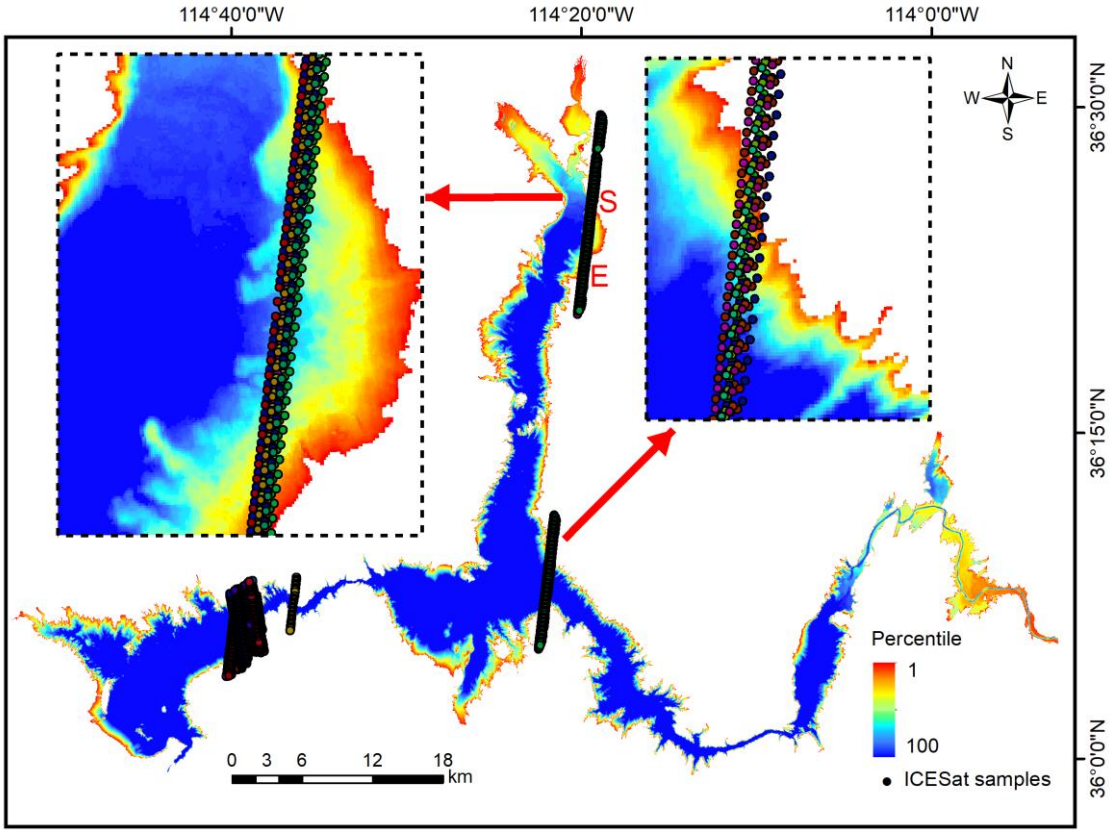

Figure 3.2 The ICESat tracks over Lake Mead from 2003 to 2010, with the Surface Water Occurrence (SWO) image as the base map.

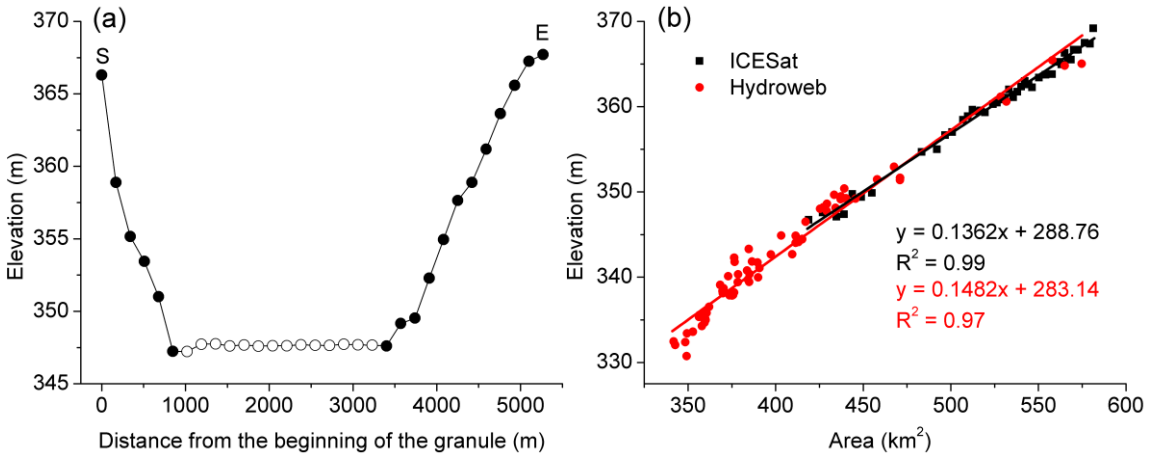

Figure 3.3 (a) The elevation profile of one ICESat track over Lake Mead on Oct 21, 2003, with the samples shown as solid dots being used to establish the Area-Elevation (A-E) relationship (the 'S' and 'E' represent the start and end of the transect, respectively, with the locations shown in Figure 3.2); and (b) the A-E relationships derived from the ICESat and Hydroweb datasets in black and red, respectively.

3.3.1.2. A-E relationships with elevations from radar altimetry datasets

For the A-E relationships derived from the radar altimetry datasets, the algorithm developed by Gao et al. (2012) was adopted. As described in section 3.2.1.2, the G-REALM and Hydroweb datasets provide the monthly mean surface elevation values over each reservoir, which can be paired with the monthly mean area values obtained from GRSAD to establish A-E relationships. Attributed to the longer data record and the more frequent revisit period of radar altimetry compared to ICESat, there were plenty of radar elevation values over various reservoirs to choose from. Therefore, only the monthly area values with cloud contaminations less than 5% were selected for the generation of the A-E relationship for each reservoir.

For comparison purposes, we also used Lake Mead to show the radar altimetry-based A-E relationship. Monthly surface water elevation data from 2000 to 2014 were

adopted from Hydroweb, while the associated monthly water surface areas were obtained from GRSAD. The R^2 of the A-E relationship based on Hydroweb is 0.97, with elevations ranging from 332.06 m to 365.03 m (Figure 3.3b). This is a larger range (32.97 m) than that from ICESat (22.47 m) because of the longer period of observations (2000–2014).

3.3.1.3. Bathymetry generation

When the elevation data for a given reservoir were available from more than one data source (ICESat, G-REALM, and Hydroweb), the A-E relationships were evaluated in terms of their R^2 values and the elevation range needed to select the one with the best performance. The R^2 of the A-E relationship was set as the first criteria. If the R^2 values were close (within 0.05), the A-E relationship with the larger elevation range was selected. To ensure the quality of the bathymetry product, we only selected reservoirs with an R^2 value greater than 0.5.

The SWO image for each reservoir was extracted using the mask described in Section 3.2.1.1. The sets of pixels in the SWO image with the same percentile values were treated as a contour line. The elevation at each percentile contour was decided by applying the A-E relationship to the area enclosed within that contour. Because the SWO image is based on 32 years of Landsat observations, it represents a large range of reservoir area/storage variation. If the range of an A-E relationship could not cover the full range of the SWO due to a shorter period of altimetry data, an extrapolation of the A-E relationship was conducted to represent the full range of dynamic bathymetry values.

Even though the SWO can capture a large dynamic range of the reservoir's area variations, the remotely sensed dynamic bathymetry results may not represent the full

bathymetry for some reservoirs. Therefore, to solve this problem, we used an extrapolation method to obtain the full bathymetry values. For those reservoirs, we first estimated the total storage that the dynamic bathymetry represented. The cumulative storage associated with the bathymetry (V_n) was calculated using equation (3.1) after Li et al. (2019b):

$$V_n = \sum_{i=1}^{n-1} \frac{(h_{i+1} - h_i)(A_{i+1} + A_i)}{2} \quad (3.1)$$

where n is the number of contours below the elevation at capacity (h_c), A_i is the surface area enclosed by the i^{th} contour, and h_i is the elevation of the i^{th} contour. The cumulative storage was calculated by integrating the storage values associated with all of the layers, starting from the top-most layer, which corresponds to the elevation at capacity. If only the area or elevation at capacity was available, the A-E relationship was used to calculate the other value. It should be noted that we did not extrapolate the bathymetry values between the SWO extent and the capacity area in cases where the SWO did not cover the full amplitude. If the cumulative storage derived from the dynamic bathymetry was smaller than the reservoir capacity, the algorithm of Tseng et al. (2016) was adopted to project bathymetric values by extrapolating the elevations using the slope derived from the remotely sensed dynamic bathymetry. The prediction process was then terminated when the accumulative storage reached the capacity, a modification of the Tseng et al. (2016) algorithm that was introduced by Li et al. (2019b). The values at capacity were collected from a combination of the Global Reservoir and Dam (GRanD) database (Lehner et al. 2011a, b) and other sources (e.g., water management agencies, web sources like Wikipedia, and the literature). In the few cases when the capacity value from GRanD for

a given reservoir did not match that from the other sources, the value from the most reliable source was selected.

3.3.2. Validation scheme

3.3.2.1. Validation of remotely sensed dynamic bathymetry

The bathymetry results were validated in two ways: (1) comparing the A-E relationships and E-V relationships to those derived from *in situ* observations and (2) comparing elevation values from arbitrarily selected transects and SWO zones with their counterparts from the surveyed bathymetry.

The A-E and E-V relationships, which together play a significant role in representing the overall physical characteristics of the reservoirs, are important byproducts of this study. More importantly, the accuracy of the A-E relationship determines the overall quality of the resulting bathymetry. Here, validations against the A-E and E-V relationships were first carried out over six U.S. reservoirs (Mead, Fort Peck, Oahe, Success, Sakakawea, and Powell) and ten Indian reservoirs (Hirakud, Jayakwadi, Malaprabha, Matatila, Sriram Sagar, Srisailam, Tawa, Tungabhadra, Gandhi Sagar, and Indravati). The *in situ* elevation and storage values were provided by the U.S. Bureau of Recreation (USBR, https://www.usbr.gov/lc/region/g4000/hourly/mead-elv.html), the U.S. Army Corps of Engineers (USACE, http://www.nwd-mr.usace.army.mil/rcc/projdata/projdata.html), the California Data Exchange Center (CDEC, http://cdec.water.ca.gov/), and the Indian Central Water Commission (CWC, http://cwc.gov.in/). The observed E-V relationships (equation (3.2)) can be directly established from *in situ* data. By taking the derivative of the water volume against the

water level (equation (3.3)), the water surface area for each incremental elevation can be calculated.

$$V = f(E) \tag{3.2}$$

$$A = \frac{dV}{dE} = f'(E) \tag{3.3}$$

The RMSE (equation (3.4)) was used as the error metric to evaluate the A-E and E-V relationships:

$$\mathrm{RMSE} = \sqrt{\frac{\sum_{i=1}^{n}(\hat{x}_i - x_i)^2}{n}} \tag{3.4}$$

where n is the number of contours of the remotely sensed bathymetry, $\hat{x}_i$ is the elevation (or storage) associated with the i^{th} contour, and x_i is the corresponding elevation (or storage) value derived from the observed A-E (or E-V) relationship.

Meanwhile, the normalized RMSE (NRMSE) (equation (3.5)) was also adopted to assess the E-V relationship:

$$\mathrm{NRMSE} = \frac{RMSE}{V_{max} - V_{min}} \times 100\% \tag{3.5}$$

where V_{max} and V_{min} are the maximum and minimum *in situ* storage values.

For most of the reservoirs, especially for those located in remote regions, bathymetry information is very scarce. Bathymetry surveys are only conducted for a small number of lakes and reservoirs by organizations such as the USBR and the U.S. Geological Survey (USGS). In this study, survey bathymetry data for four U.S. reservoirs (Lake Mead, Lake Roosevelt, Cascade Reservoir, and Clear Lake), provided by the USBR (https://www.usbr.gov/tsc/techreferences/reservoir.html) and the USGS

(https://pubs.usgs.gov/of/2003/of03-320/index.htm) (Twichell et al. 2003), were used to directly validate the bathymetry results. The survey data for these lakes were collected in different ways, which are summarized in Table 3.2. Although the lidar survey cannot provide the bathymetry information for the entire reservoir due to its weak water penetration capacity, its range is sufficient to evaluate the dynamic bathymetry and is a better choice than the low-resolution sediment survey data. For each of these four reservoirs, four transects across the shoreline were used to compare the elevations from the remotely sensed bathymetry with their counterpart values from the surveyed bathymetry. Meanwhile, in order to assess the overall performance of the remotely sensed bathymetry, the SWO image of each reservoir was divided into 10 zones with a 10% increment. Then, the elevation statistics for each zone were compared between the remotely sensed bathymetry and the survey data.

Table 3.2 Summary of the survey methods used to collect the *in situ* data for the four validated reservoirs

Reservoir name	Survey methods
Lake Mead	lidar survey, sedimentation survey
Lake Roosevelt	lidar survey, aerial photogrammetry, hydrographic survey
Cascade Reservoir	sedimentation survey, aerial photogrammetry
Clear Lake	aerial photogrammetry, hydrographic survey

3.3.2.2. Validation of the projected bathymetry

Since sedimentation survey is the single approach used to measure the full bathymetry (i.e., all the way to reservoir bottom), it is the only data source that the projected part of the bathymetry can be validated against. However, relatively costly sedimentation surveys are extremely limited. Therefore, we were only able to evaluate the performance of the projected bathymetry over Lake Mead and the Cascade Reservoir.

Similar to the validation of the remotely sensed bathymetry, the projected bathymetry was also validated against the survey values along arbitrarily selected transects. Moreover, the projected bathymetry of Lake Mead was also validated using A-E and E-V relationships.

3.4. Results

3.4.1. Overview of the global reservoir bathymetry dataset

In this study, we generated bathymetry for 347 global reservoirs (274 from ICESat, 42 from G-REALM, 31 from Hydroweb), with a total volume of 3123 km^3, representing 50% of the total global reservoir capacity according to the GRanD database. The locations of these 347 reservoirs are shown in Figure 3.4. Their attributes in each geographical region and in selected countries (with the greatest number of reservoirs) are summarized in Table 3.3. These attributes of the area, shoreline length, and storage are adopted from the HydroLAKES database.

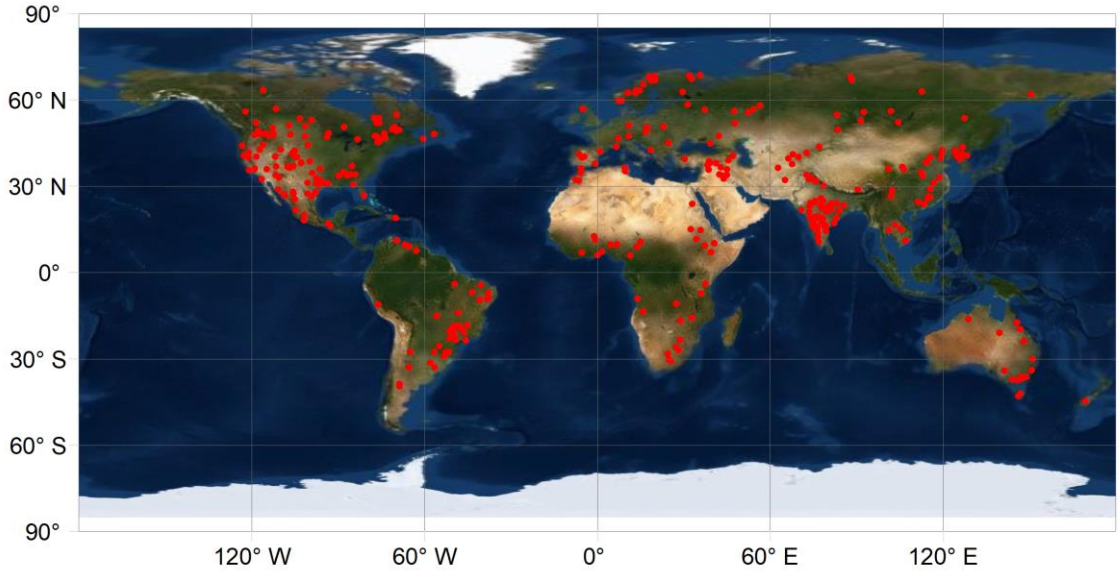

Figure 3.4 Locations of the 347 reservoirs with the bathymetry generated from this study.

Table 3.3 Distribution and attributes of the global reservoir bathymetry dataset

	Number of reservoirs	Average R^2 of A-E	Area (km^2)	Shoreline length (km)	Storage (km^3)
World	347	0.89	166487	177666	3123
Continent					
Africa	35	0.92	25170	26419	662
Asia	105	0.91	24450	23567	603
Europe	52	0.84	59725	31192	603
North America	102	0.90	33556	58631	663
Oceania	16	0.91	2079	2743	50
South America	37	0.86	21506	35113	542
Countries with most reservoirs					
U.S.	58	0.91	9720	12693	221
India	45	0.93	6065	8022	121
Canada	31	0.85	22259	42985	393
China	27	0.91	3661	5368	113
Brazil	24	0.85	13476	26072	334
Russia	22	0.78	58070	28613	586
Australia	15	0.94	1931	2632	48

For each continent (except Antarctica), we selected one representative reservoir to show the dynamic bathymetry result (Figure 3.5). Because Guri (Figure 3.5f) is relatively large, only partial results are provided in order to show more detail. Overall, the remotely sensed bathymetry results show clear patterns and gradients. Detailed topography can be nicely captured, especially around the areas where the floodplains are very dynamic (Figure 3.5a, 3.5c, and 3.5f). The remotely sensed dynamic area, dynamic area fraction, dynamic storage, and dynamic storage fraction values of these reservoirs were also calculated. The dynamic area is the area difference between the maximum water area and the permanent water area (i.e., the area enclosed by the most inner percentile of the SWO image). The dynamic area fraction is the ratio of the dynamic area over the maximum water extent from the SWO image, which represents the magnitude of area variation from

1984 to 2015. The dynamic storage and storage fraction are defined in relation to those area terms.

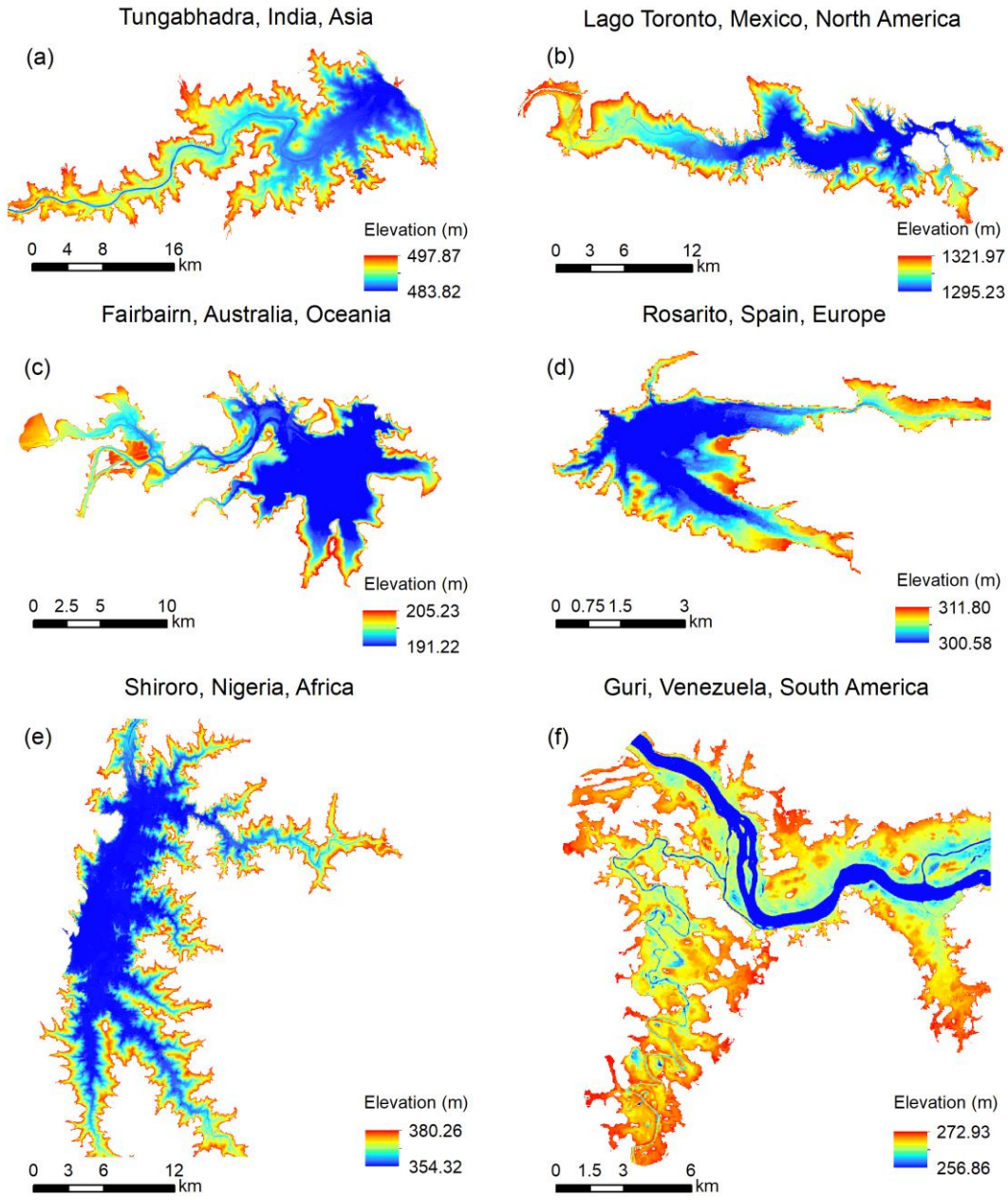

Figure 3.5 Remotely sensed bathymetry values for reservoirs (a) Tungabhadra, (b) Lago Toronto, (c) Fairbairn, (d) Rosarito, (e) Shiroro, and (f) Guri. For Guri, only partial bathymetry is displayed here due to the reservoir's large size.

In addition, the remotely sensed bathymetry maps for sixteen reservoirs, for which the A-E and E-V relationships are also validated in Section 3.4.2.1, are shown in Figures S1 to S16 in Appendix A, and their attributes are summarized in Table S1 in Appendix A. Among these reservoirs, the remotely sensed results captured the largest dynamic area at Srisailam (96.81%) and the smallest at Sakakawea (35.38%). Moreover, the dynamic bathymetry of these sixteen reservoirs represents over half of the storage at capacity, with the largest at Success (100%) and the smallest at Oahe (57.70%). Therefore, most of these reservoirs have had relatively large dynamics over the last three decades. It is worth noting that our method (ICESat + SWO) can detect relatively small reservoirs (with areas less than 50 km^2 by Lehner and Döll (2004)) due to the high spatial resolution and vertical accuracy of ICESat. In this dataset, the smallest reservoir detected by ICESat is Mehgaon Tola Tank (India), which has an average area of 1.47 km^2. Clear patterns can be observed from the bathymetry map (Figure S17 in Appendix A).

3.4.2. Bathymetry validation

First, the A-E relationships and the E-V relationships derived from observations were used to validate their counterparts generated from this study. This is because the A-E relationships and E-V relationships are the most important byproducts of this dataset and are good indicators of the quality of the 3-D bathymetry results (section 3.4.2.1). Then, the survey data were used to validate the remotely sensed portion of bathymetry over four U.S. reservoirs (section 3.4.2.2). Last, the sediment survey data were used to evaluate the performance of the projected portion of bathymetry over Lake Mead and the Cascade Reservoir (section 3.4.2.3).

3.4.2.1. Validation of the remotely sensed A-E and E-V relationships

The A-E relationships derived from remote sensing data and *in situ* observations are summarized in Table 3.4 and plotted in Figure 3.6. It is evident that these two kinds of A-E relationships are in good agreement, with RMSE values of elevation ranging from 0.10 m to 1.99 m. Since the ICESat and Hydroweb datasets are both available for Lake Mead, we validated the A-E relationships derived from each for comparison. The A-E relationships from ICESat and Hydroweb both agree well with the *in situ* results (Figure 3.6a), but the relationship from ICESat performed better than that from Hydroweb. Moreover, it is worth noting that R^2 values alone cannot fully represent the quality of the A-E relationship in some cases. For example, the R^2 value for the Hirakud reservoir (0.68) is relatively low, but its A-E shows good consistency with the *in situ* measured values. The remotely sensed A-E relationships of Fort Peck (Figure 3.6b), Matatila (Figure 3.6k), Sriram Sagar (Figure 3.6l), and Tawa (Figure 3.6n) have clear shifts compared to their *in situ* counterparts. These shifts can be attributed to three sources of biases. The first is the bias associated with the misspecification of the static water extents by HydroLAKES over some reservoirs. The second source is related to the uncertainties from both satellite and *in situ* measurements. Last, the remotely sensed and *in situ* elevations might have used different geoids, which could also lead to a bias. These shifts can explain the relatively high RMSE values seen when the A-E relationships were validated. However, the slopes of the remotely sensed A-E relationships are in good agreement with the *in situ* values, indicating that they can characterize the elevation gradients well. Overall, the A-E

relationships derived in this study are reliable and lay the foundation for the generation of bathymetry.

Table 3.4 The A-E relationships derived from remote sensing data and *in situ* observations.

Reservoir name	Country	Elevation dataset	A-E relationship (remotely sensed)	A-E relationship (*in situ*)	RMSE (m)
Mead	U.S.	ICESat	$y = 0.1362x + 288.76$, $R^2=0.99$	$y = 0.1369x + 287.26$, $R^2=1.00$	1.27
Mead	U.S.	Hydroweb	$y = 0.1482x + 283.14$, $R^2=0.97$	$y = 0.1369x + 287.26$, $R^2=1.00$	1.46
Fort Peck	U.S.	ICESat	$y = 0.0438x + 643.32$, $R^2=0.97$	$y = 0.0443x + 644.65$, $R^2=0.99$	1.85
Oahe	U.S.	ICESat	$y = 0.0217x + 462.73$, $R^2=0.87$	$y = 0.0209x + 463.74$, $R^2=1.00$	0.80
Success	U.S.	ICESat	$y = 3.8029x + 172.98$, $R^2=0.99$	$y = 3.8258x + 172.98$, $R^2=1.00$	0.06
Sakakawea	U.S.	G-REALM	$y = 0.0247x + 528.65$, $R^2=0.89$	$y = 0.0220x + 532.57$, $R^2=1.00$	0.89
Powell	U.S.	G-REALM	$y = 0.1357x + 1045.1$, $R^2=0.97$	$y = 0.1317x + 1046.2$, $R^2=1.00$	1.99
Gandhi Sagar	India	ICESat	$y = 0.0337x + 379.03$, $R^2=0.95$	$y = 0.0339x + 379.30$, $R^2=1.00$	0.69
Hirakud	India	ICESat	$y = 0.0220x + 177.26$, $R^2=0.68$	$y = 0.0221x + 177.54$, $R^2=1.00$	0.69
Jayakwadi	India	ICESat	$y = 0.0320x + 451.67$, $R^2=0.77$	$y = 0.0314x + 451.72$, $R^2=1.00$	0.80
Malaprabha	India	ICESat	$y = 0.1281x + 618.72$, $R^2=0.93$	$y = 0.1298x + 618.29$, $R^2=1.00$	0.76
Matatila	India	ICESat	$y = 0.1003x + 297.22$, $R^2=0.94$	$y = 0.0982x + 297.05$, $R^2=1.00$	0.47
Sriram Sagar	India	ICESat	$y = 0.0400x + 319.95$, $R^2=0.98$	$y = 0.0419x + 318.54$, $R^2=1.00$	1.17
Srisailam	India	ICESat	$y = 0.0308x + 253.30$, $R^2=1.00$	$y = 0.0308x + 253.38$, $R^2=1.00$	0.10
Tawa	India	ICESat	$y = 0.1110x + 336.49$, $R^2=0.89$	$y = 0.1140x + 335.17$, $R^2=1.00$	1.45
Tungabhadra	India	ICESat	$y = 0.0412x + 483.34$, $R^2=0.98$	$y = 0.0410x + 483.40$, $R^2=1.00$	0.41
Indravati	India	G-REALM	$y = 0.3347x + 604.63$, $R^2=0.94$	$y = 0.3418x + 604.43$, $R^2=1.00$	1.20

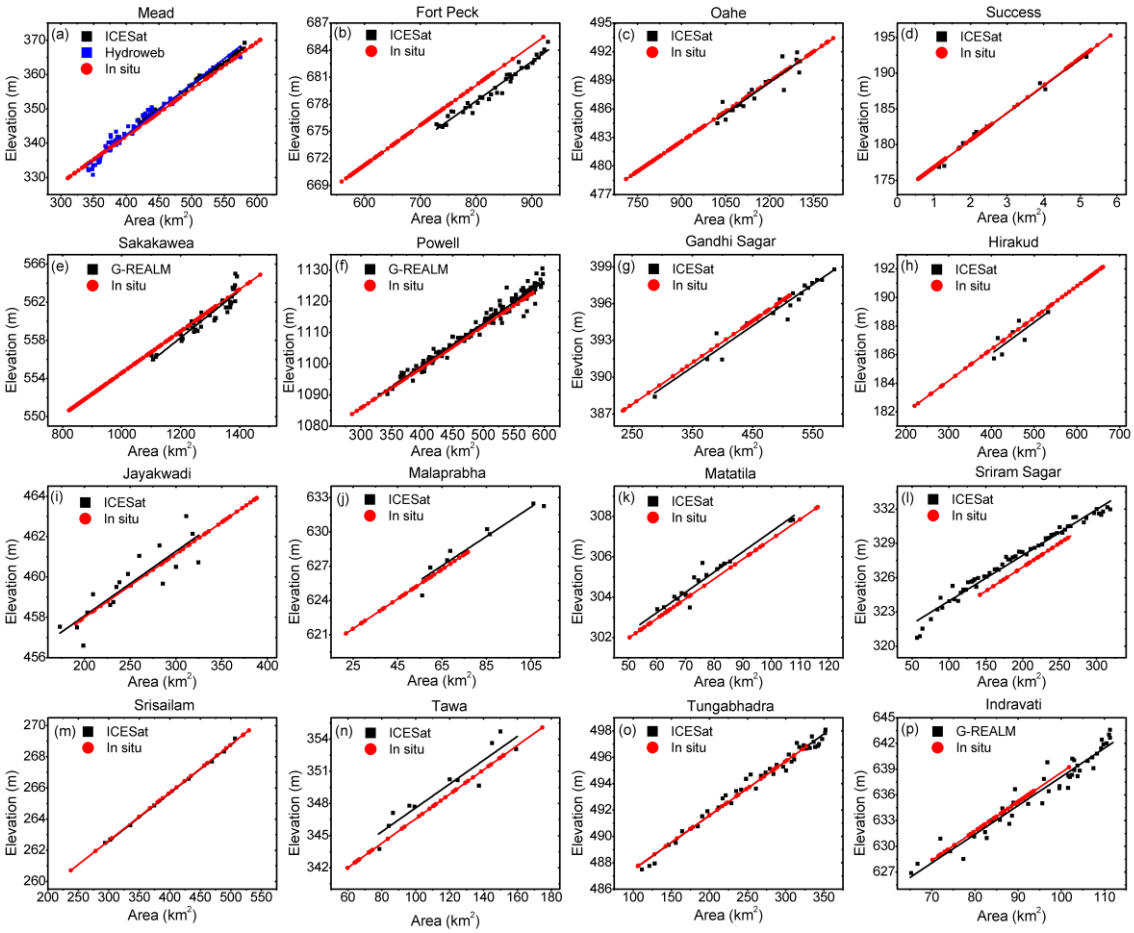

Figure 3.6 Comparisons of the Area-Elevation (A-E) relationships derived from remote sensing data and *in situ* observations over (a) Mead, (b) Fort Peck, (c) Oahe, (d) Success, (e) Sakakawea, (f) Powell, (g) Gandhi Sagar, (h) Hirakud, (i) Jayakwadi, (j) Malaprabha, (k) Matatila, (l) Sriram Sagar, (m) Srisailam, (n) Tawa, (o) Tungabhadra, and (p) Indravati Reservoirs.

Figure 3.7 indicates that the E-V relationships derived from the remote sensing data are in good agreement with those based on *in situ* observations. The error statistics show that all of the R^2 values are greater than 0.99, the RMSE values of storage are from 0.0029 km^3 to 0.35 km^3, and the NRMSE values are from 0.56% to 4.40%. In some cases, especially for some of the relatively smaller reservoirs in terms of capacity, the estimated storage may have a relatively large bias when the elevation level reaches the reservoir

bottom (e.g., Sriram Sagar and Tawa). It should be noted that even though the remotely sensed A-E relationship for Lake Success agrees with the *in situ* value (Figure 3.6d), the E-V relationship shows a relatively large bias (Figure 3.7d), with an NRMSE of 4.40%. This is because Lake Success is a small reservoir with a maximum area of 7.92 km^2 and a storage capacity of 0.10 km^3. Therefore, the estimations of storage are more sensitive to elevation and area measurements, and even a small RMSE value of storage (0.0029 km^3) would result in a relatively large NRMSE value (4.40%).

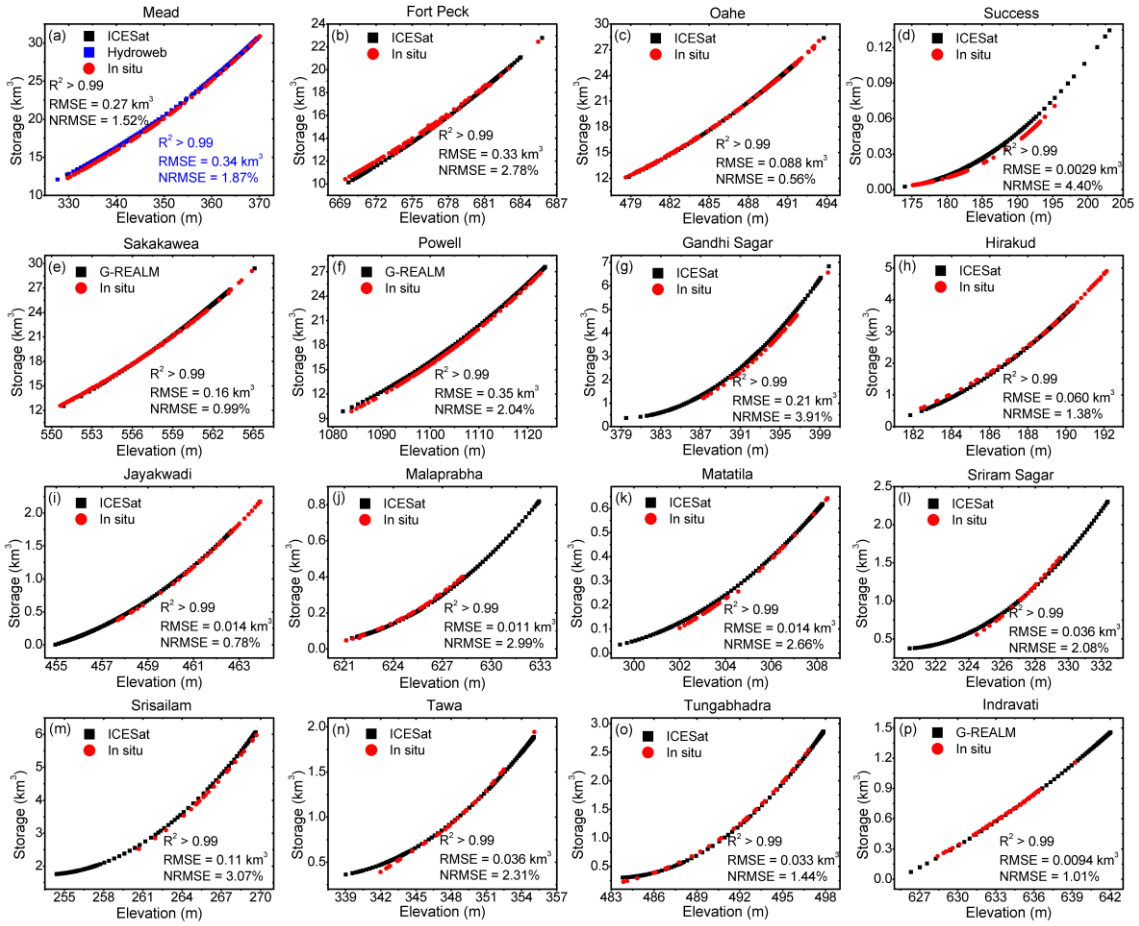

Figure 3.7 The validation of the remotely sensed Elevation-Volume (E-V) relationships over (a) Mead, (b) Fort Peck, (c) Oahe, (d) Success, (e) Sakakawea, (f) Powell, (g) Gandhi Sagar, (h) Hirakud, (i) Jayakwadi, (j) Malaprabha, (k) Matatila, (l) Sriram Sagar, (m) Srisailam, (n) Tawa, (o) Tungabhadra, and (p) Indravati Reservoirs.

3.4.2.2. Validation of the remotely sensed bathymetry results against survey data

The survey data for Lake Mead, Lake Roosevelt, Cascade Reservoir, and Clear Lake Reservoir were used to directly validate the bathymetry values. The remotely sensed bathymetry maps and the locations of the validation transects for these reservoirs are shown in Figure 3.8 and Figures S18 to S20 in Appendix A. The characteristics of the remotely sensed bathymetry for these four reservoirs are summarized in Table 3.5. For Lake Mead, the bathymetry results based on ICESat and Hydroweb elevations were also compared. The elevation range of the remotely sensed dynamic bathymetry of these four reservoirs varies from 5.54 m to 41.94 m. Among these reservoirs, the remotely sensed results captured the largest dynamic area fraction at Lake Mead (48.48%) and smallest at the Cascade Reservoir (26.65%). Most importantly, the dynamic bathymetry associated with the dynamic area of these four reservoirs represents more than half of the storage at capacity, with the largest value at the Clear Lake Reservoir (94.27%) and the smallest at the Cascade Reservoir (57.10%). The small dynamic storage range of the Cascade Reservoir is attributed to the fact that the reservoir has relatively small seasonal and interannual variations. It is worth noting that the dynamic bathymetry of the Clear Lake Reservoir can almost represent the full bathymetry. The average depth at maximum capacity of the Clear Lake Reservoir is about 6.10 m (https://www.usbr.gov/projects/index.php?id=27, accessed 22 January 2020), which is close to the elevation range of the remotely sensed bathymetry (7.62 m).

Table 3.5 Summary of the remotely sensed bathymetry over the four validated reservoirs

Reservoir name	Lake Mead		Lake Roosevelt	Cascade Reservoir	Clear Lake Reservoir
Elevation dataset	ICESat	Hydroweb	G-REALM	G-REALM	ICESat
R^2 of A-E	0.99	0.97	0.69	0.94	0.97
Minimum elevation (m)	329.71	327.70	370.60	1466.82	1357.84
Maximum elevation (m)	368.25	369.64	392.95	1471.14	1365.46
Elevation range (m)	38.54	41.94	22.35	5.54	7.62
Total area (km^2)	583.64	583.64	292.53	99.11	98.45
Dynamic area (km^2)	282.97	282.97	78.18	26.41	38.17
Dynamic area fraction	48.48%	48.48%	26.73%	26.65%	38.77%
Storage capacity (km^3)	34.07	34.07	6.60	0.80	0.65
Dynamic storage (km^3)	21.36	23.24	5.67	0.46	0.61
Dynamic storage fraction	62.69%	68.22%	85.86%	57.10%	94.27%

First, the resulting bathymetry of Lake Mead is visually inspected. As the results derived from ICESat and Hydroweb radar altimetry have the same spatial patterns, only the ICESat-based bathymetry was examined (Figure 3.8). The lidar survey for Lake Mead was conducted by USBR in 2009 and covered 445.48 km^2 of the emergent shoreline areas. This survey contains detailed contour values (Figure 3.8f) from 334.06 m (1096 feet) to 374.90 m (1230 feet) at a 0.61 m (2 feet) interval. Overall, the elevation patterns are very similar to those of the contour map collected by the lidar survey (i.e., Figure 3.8a vs. Figure 3.8f and Figure 3.8 (b–e) vs. Figure 3.8 (g–j)). For the western region (Figure 3.8b), the bathymetry has steep gradients across the shorelines, and the shapes of the islands within this area are clearly captured. For the northern region (Figure 3.8c), the gradients are relatively gradual, indicating that this portion is relatively flat compared to the west. As shown in Figure 3.8e, the topography surrounding the Colorado River can be distinctly captured, whereas the river bottom measured by lidar appeared to be flat (Figure 3.8j). This disagreement led to three outliers in the corresponding scatter plot of Transect 4

(Figure 3.9a), which contributed to the relatively low R^2 value for this transect. Overall, the remotely sensed bathymetry values have relatively high reliability and accuracy.

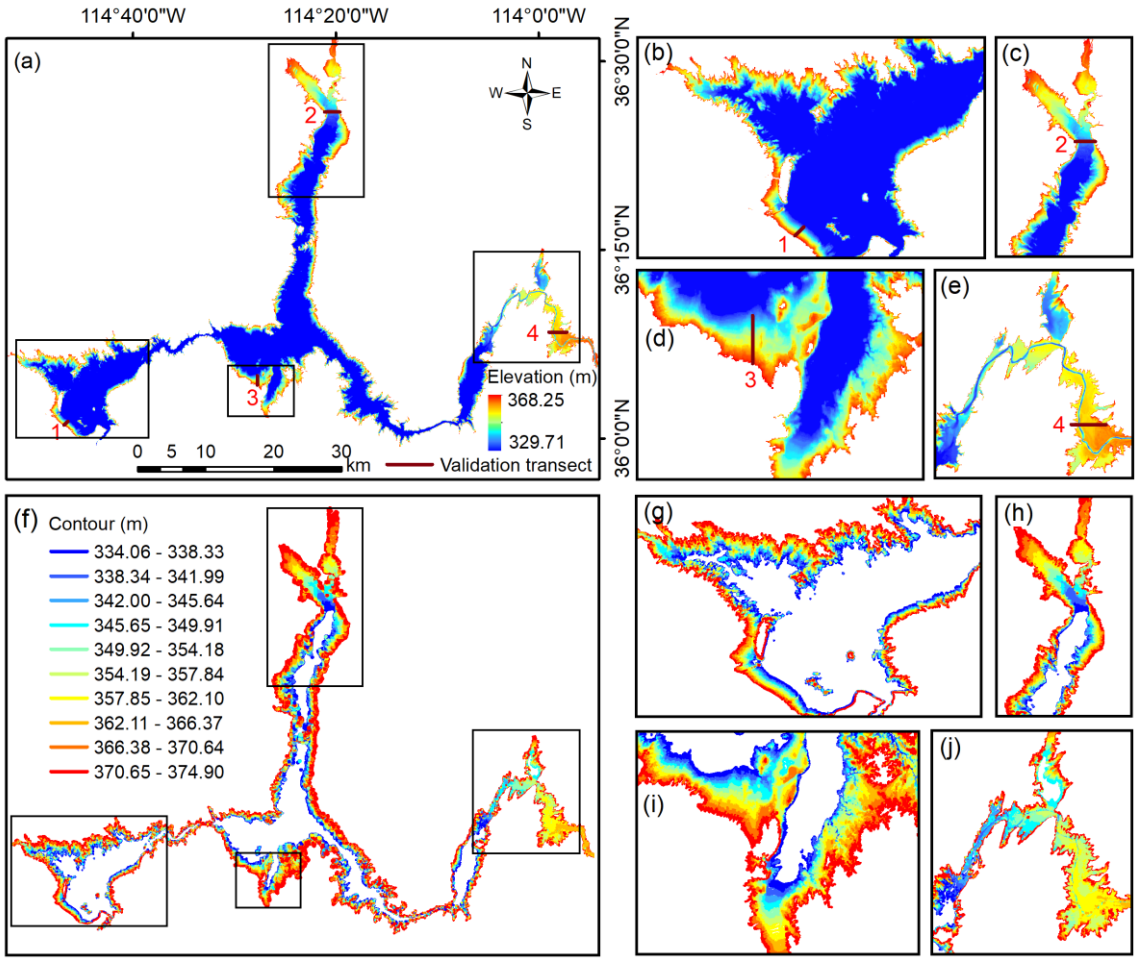

Figure 3.8 The bathymetry of Lake Mead using the Area-Elevation (A-E) relationship derived from the ICESat database (a–e): (a) Overall bathymetry; (b-e) close up views of the four sub-regions in (a); and lidar survey contour maps (f–j): (f) Overall bathymetry; (g–j) close up views of the four sub-regions in (f).

Visual inspection was found to be unsuitable for the other three reservoirs. For Lake Cascade and Clear Lake, the surveyed data are disconnected points, which makes it difficult to discern patterns. Although the surveyed bathymetry of Lake Roosevelt is a

continuous image, this reservoir is very sinuous and narrow, making it difficult to make visual comparisons.

The validations against the surveyed data were carried out at two spatial scales: the individual transects and the remotely sensed bathymetry over the entire reservoir.

At an individual transect level, the elevation values from this study are in good agreement with the surveyed data (Figure 3.9). Clearly, the remotely sensed bathymetry can capture the elevation gradients of the reservoirs. With regard to the scatter plots, most samples are centered along the 1:1 line, except for the Clear Lake Reservoir, which features an overall underestimation of the elevation values. This nearly constant underestimation was due to the bias of the vertical datum. When the USBR conducted the hydrographic survey over the Clear Lake Reservoir in 2007, they used their own project's datum, while the bathymetry generated in this study references the EGM08 datum. Nonetheless, the variations in the remotely sensed results are consistent with those of the surveyed data. It should be noted that this constant discrepancy does not influence the volume estimation because we used the elevation difference when calculating the storage values with equation (3.1). For Lake Mead, even though the A-E relationship derived from ICESat seems to be more accurate than that from Hydroweb, the ICESat-based bathymetry does not necessarily perform better for the entire reservoir. Indeed, for elevations less than 352.55 m, the Hydroweb-based bathymetry values are closer to the survey elevations. For elevations greater than 352.55 m, the ICESat-based bathymetry performs better. This explains why the Hydroweb-based bathymetry values have smaller errors in some regions (e.g., transect 2 with an RMSE of 1.33 m for Hydroweb vs. 1.78 m for ICESat).

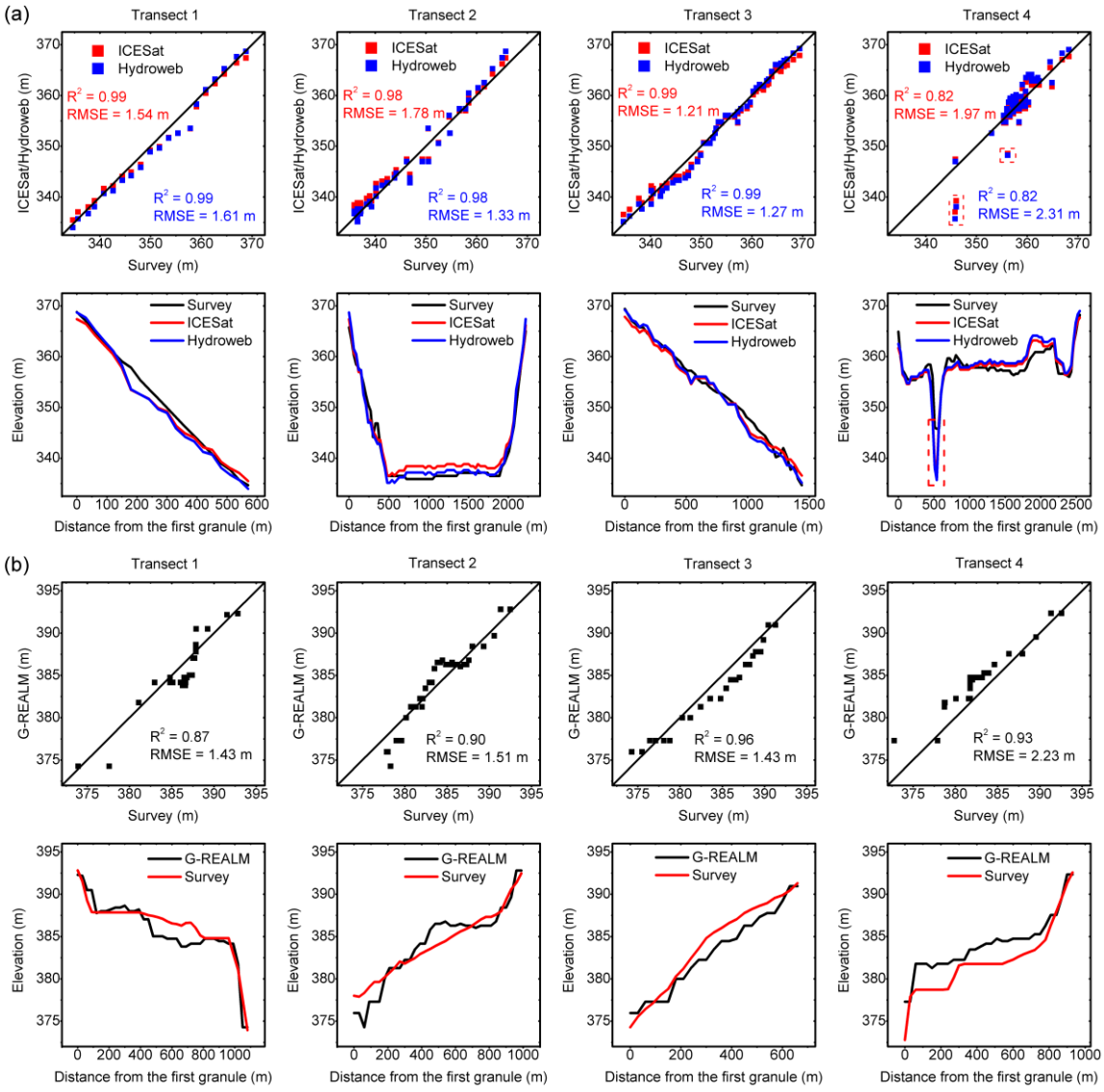

Figure 3.9 Scatter plots and elevation profiles of the validation transects over: (a) Lake Mead, (b) Lake Roosevelt, (c) Cascade Reservoir, and (d) Clear Lake Reservoir.

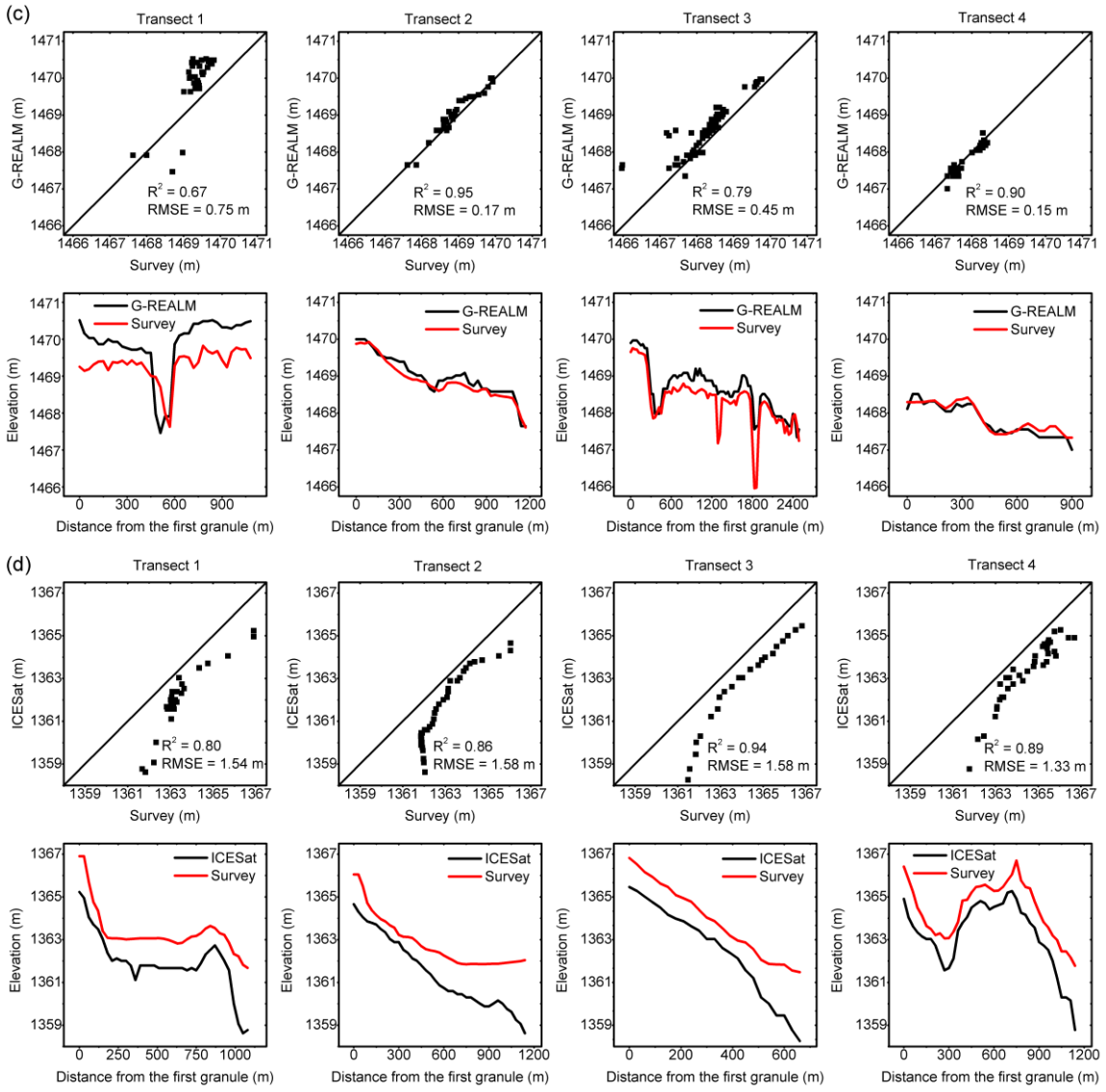

Figure 3.9 Continued.

The statistics of the validation results over the selected transects are summarized in Table S2 in Appendix A. The elevation values from the remotely sensed bathymetry agree well with those from the survey data for all four of these reservoirs, with R^2 values from 0.82 to 0.99 and RMSE values from 0.13 m to 2.31 m. Even though the R^2 value of the A-E relationship for Lake Roosevelt is only 0.69, the resulting bathymetry is satisfactory (with R^2 values from 0.87 to 0.96, and RMSE values from 1.43 m to 2.23 m).

To evaluate the results over the entire reservoir, we also compared the statistics of the satellite-derived bathymetry and ground surveys within each 10% SWO percentile zone (Figure 3.10). For Lake Mead, the remotely sensed bathymetry from both radar and ICESat altimetry performed the best within the 51%–90% zones. It slightly overestimated the elevations for the 1%–50% zone and underestimated them for the innermost zone (91%–100%). Between the two datasets, ICESat-based bathymetry performed better than the radar-based bathymetry from Hydroweb. This is because ICESat was capable of measuring the topography along the ground track with its 70 m resolution footprint, while the radar altimeter can only provide one averaged elevation value per observation time for the entire reservoir due to its larger footprint. Moreover, ICESat-derived elevations have been found to be more accurate than those from radar altimeters due to ICESat's high vertical accuracy (Brenner et al. 2007).

For Lake Roosevelt, the remotely sensed bathymetry overestimated over the entire reservoir, except in the 91%–100% zone. For the Cascade Reservoir, the bathymetry overestimation dominated, with the discrepancy decreasing from the outer zone to the inner zone (with the exception of the 81%–100% zones). For the Clear Lake Reservoir, the satellite results are underestimated across all zones, especially in the 71%–100% range (by 4.26 m). Overall, the remotely sensed bathymetry values are in good agreement with the survey data, with the largest biases usually found in the shoreline and central regions.

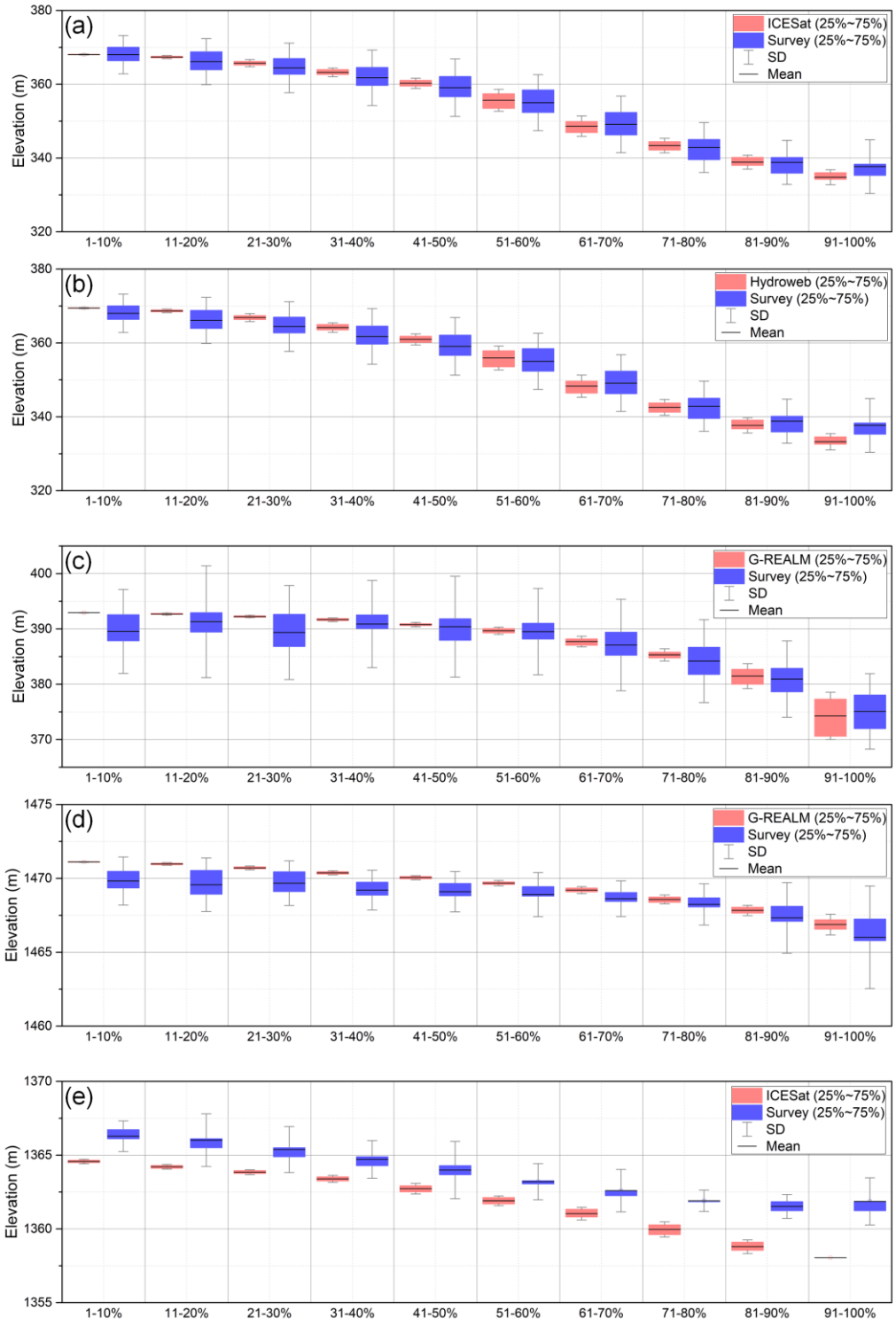

Figure 3.10 Comparisons of the statistical results of the elevations within each percentile zone over the entire reservoir for (a) Lake Mead (ICESat), (b) Lake Mead (Hydroweb), (c) Lake Roosevelt, (d) the Cascade Reservoir, and (e) the Clear Lake Reservoir.

3.4.2.3. Evaluation of the projected bathymetry

In this study, we selected Lake Mead and the Cascade Reservoir to evaluate the performance of the projected portion of the bathymetry. Lake Roosevelt and the Clear Lake Reservoir were not used to assess the projection because their remotely sensed portion already represents nearly full bathymetry in terms of storage (Table 3.5). Figure 3.11a shows the full bathymetry of Lake Mead, including the remotely sensed part (329.71 m to 368.25 m) and the projected part (263.00 m to 329.70 m). The projected portions in Figure 3.11d and Figure 3.11e have more realistic patterns, as the abrupt changes in Figure 3.11b and Figure 3.11c are not very natural. The full bathymetry of Cascade Reservoir is shown in Figure S21 in Appendix A, with a remotely sensed portion (1466.82 m to 1471.14 m) and a projected portion (1461.00 m to 1466.81 m). It is worth noting that the bottom elevations estimated in this study (263.00 m for Lake Mead and 1461.00 for Cascade Reservoir) are close to the measured values from the sedimentation surveys (272.80 m for Lake Mead and 1459.23 m for Cascade Reservoir). The projected bathymetry results show good overall patterns, but the changes in elevation are not consistent with the surrounding areas in some cases. This is because the algorithm by Tseng et al. (2016) assumed that the slope does not change once determined.

Similarly, we selected four transects evenly distributed over both Lake Mead (Figure 3.11) and the Cascade Reservoir (Figure S21 in Appendix A) to compare the elevation values of the projected bathymetry with their counterparts from the sedimentation survey data. It should be noted that, in both cases, these four transects only cover the projected bathymetry area. For Lake Mead, the scatter plots and elevation

profiles of these four transects are shown in Figure 3.12. The projected bathymetry for transect 1P matches the survey data well because the slopes are relatively constant in this area. For transect 4P, the results are acceptable except for locations near the end of the transect. However, for transects 2P and 3P, the projected bathymetry largely missed the slopes from the survey, especially for the area relatively far away from the shore. According to Figure 3.12, the topography at transect 2P is relatively flat, and the elevation values at transect 3P have relatively large fluctuations. It was found that there exists an abrupt jump at transect 2P—from 295 m to 263 m. This is because the slopes used for extrapolation varied with region, and the elevation did not reach to 263 m when the extrapolation was terminated. However, for other transects the elevation variations are continuous. Even though transect 3P has a relatively large bias (RMSE = 18.87 m), it reached the lowest elevation simultaneously with the surveyed bathymetry. Results for the Cascade Reservoir are shown in Figure S22 in Appendix A. Among these four transects, transects 1P and 4P are in relatively good agreement with the survey data, while transects 2P and 3P have large vertical errors. Because the method by Tseng et al. (2016) assumes a constant slope, the extrapolated elevations cannot capture the underwater topography when it is either flat or has a great variation (e.g., bulge and cavity). Thus, the projected bathymetry values should be used with caution.

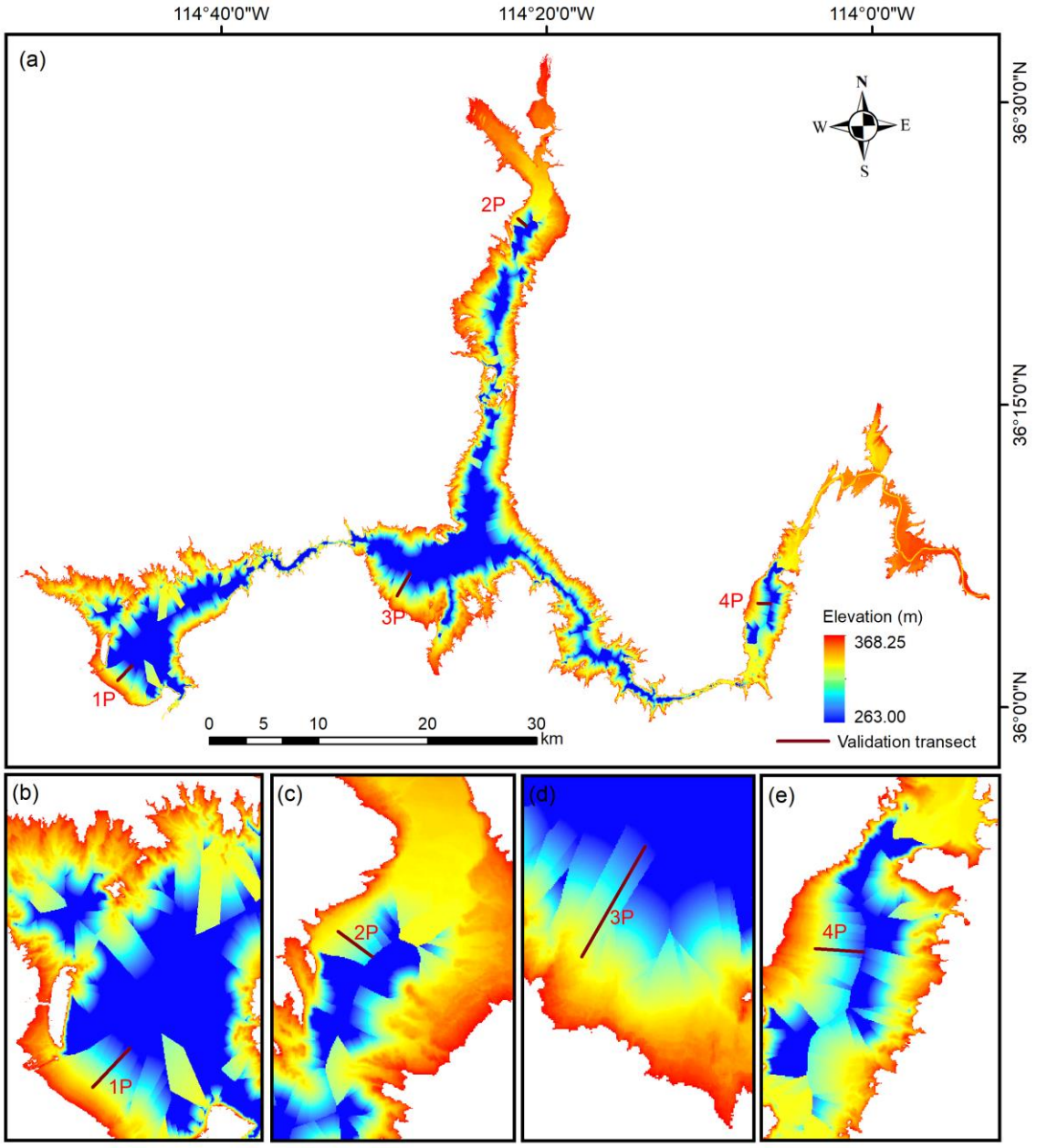

Figure 3.11 (a) Full bathymetry of Lake Mead (remotely sensed bathymetry plus projected bathymetry) and close up views of the four sub-regions: (b) the west, (c) the north, (d) the south, and (e) the east. The transects 1P, 2P, 3P, and 4P only cover the projected bathymetry values.

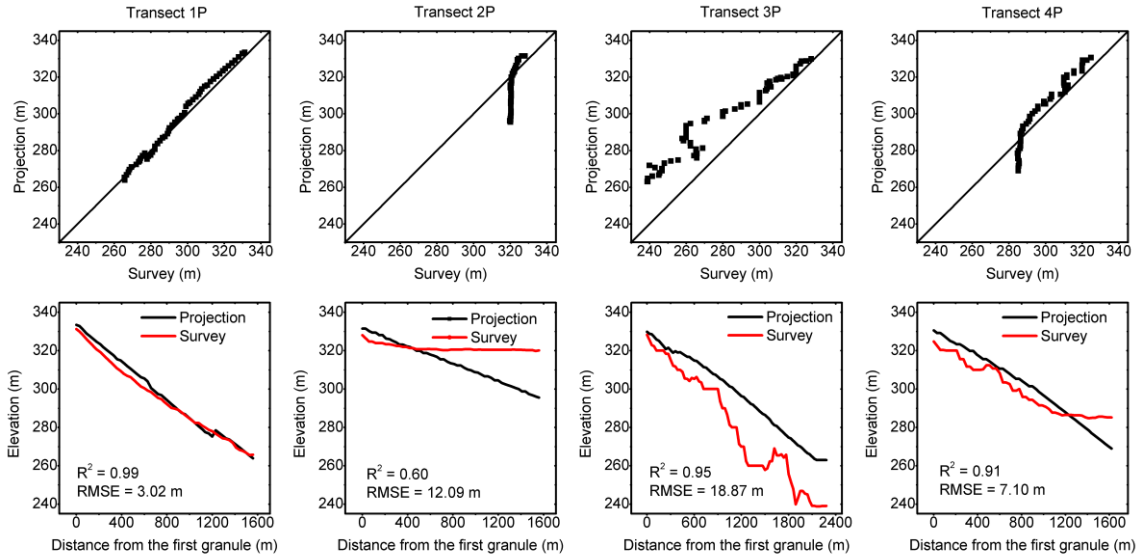

Figure 3.12 Scatter plots and elevation profiles for transects 1P, 2P, 3P, and 4P over Lake Mead.

Moreover, the A-E and E-V relationships from the projected portion of Lake Mead were also compared with those from the sedimentation survey (Figure 3.13). The underwater elevations and their associated areas and volumes were obtained from the look-up tables provided by the USBR (2011). Though the A-E and E-V relationships from the projected bathymetry have good correlations with the survey (with R^2 values of 0.99 and 1.00), they have relatively large vertical discrepancies (with an RMSE of elevation 6.49 m, and an NRMSE of storage 17.92%). Moreover, by comparing the accumulative storage of the bathymetry with the capacity, the bottom elevation of the live storage (i.e., dead storage elevation) was detected at 263.00 m but was 272.80 m (with an absolute bias of 9.80 m) according to the sedimentation survey (USBR 2011). In general, considering the limitations and uncertainties of the extrapolation method, the performance of the projected bathymetry is acceptable.

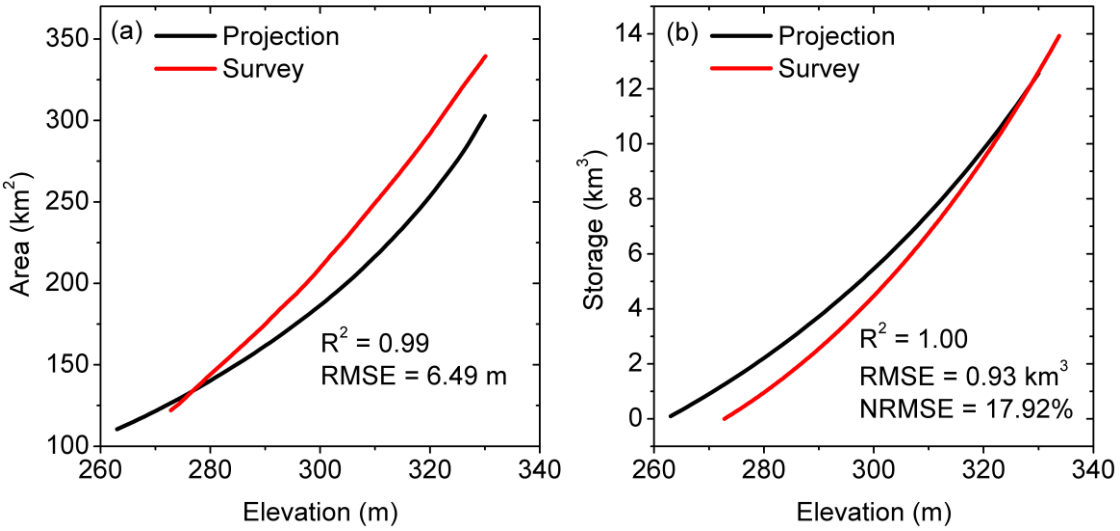

Figure 3.13 Comparison of (a) the Area-Elevation (A-E) relationship and (b) the Elevation-Volume (E-V) relationship between the projected bathymetry and the sedimentation survey over Lake Mead.

3.5. Discussion

3.5.1. Accuracies and sources of uncertainty

The reliability and accuracy of the remotely sensed bathymetry values depend on the quality of the SWO image and the A-E relationships. The SWO image provides the base map of a reservoir showing the initial spatial patterns. The bathymetry values were determined by applying the A-E relationship to the area associated with each SWO contour.

The SWO dataset was a byproduct of the state-of-the-art GSW (Pekel et al. 2016), which used an expert system classifier to generate the monthly surface water maps from Landsat images from 1984 to 2015. To our knowledge, the GSW is the most reliable high-resolution inland water product, given its extremely low omission and commission errors (less than 5% and 1%, respectively). Although Zhao and Gao (2018) reclassified the contaminated pixels (i.e., 'no data') to 'water' or 'not water' in the monthly GSW maps,

the GSW still has some limitations that need to be addressed. For the reservoirs located in the tropics, the number of clear satellite views is relatively small, as cloud cover is persistent during the monsoon season. As a result, the large reservoir area variations due to monsoon rainfall cannot be captured. In addition, the vegetation canopy is another issue for determining the exact water extent. These errors could have affected the accuracy of SWO in Pekel et al. (2016). However, because SWO is based on 32 years of Landsat classifications, with an average of 537 views globally, these effects on the contour patterns can be considered minor.

Depending on the availability of the altimetry data, two different methods were adopted to generate the A-E relationships. Validations against *in situ* observations demonstrated the reliability of these derived A-E relationships. As the radar altimetry data (G-REALM and Hydroweb) were aggregated to a monthly time step to coincide with that of the GRSAD dataset, some of the errors may be attributed to the fact that the collection times of Landsat and radar altimetry do not exactly match within a given month. However, it is difficult to quantify this kind of uncertainty due to the different temporal resolutions of the various satellites involved. Whereas for the A-E relationships derived from ICESat, the advantage of long-term Landsat observations (1984–2015) was fully leveraged by projecting the ICESat tracks onto the SWO image. The high spatial resolution and accuracy of the ICESat data allow for the coverage of more reservoirs and result in high-quality A-E relationships. To guarantee the quality of the bathymetry products, we only mapped the reservoirs with R^2 values of A-E relationships greater than 0.5.

Compared to the remotely sensed portion, the projected portion of the bathymetry has relatively large uncertainties and errors. The performance of the extrapolation method heavily relies on the assumption that the shoreline slope can represent the underwater slope. However, this assumption is not applicable for some parts of a reservoir. Comprehensive evaluations of these extrapolation methods have been presented in Tseng et al. (2016) and Getirana et al. (2018). It should be noted that a 5x5 window was used to compute the average slope for extrapolation; thus, the extrapolation cannot be applied to the reservoirs that do not have sufficient dynamic area to derive the slope. Moreover, additional uncertainty can be introduced due to the inaccurate capacity values that were obtained using different methods and instruments, some of which may not be reliable. In addition, the bottom part of the reservoir bathymetry is often affected by sedimentation, which is very difficult to quantify (Schleiss et al. 2016).

3.5.2. Advantages and limitations

Airborne lidar survey has been an important tool for mapping bathymetry since the early 1970s (Muirhead and Cracknell 1986). This approach is relatively accurate but limited by water clarity and depth. Typically, a bathymetric lidar instrument can only collect data within three times the Secchi depth at the site (Irish and Lillycrop 1999). While a sedimentation survey can take measurements all the way to the bottom, it cannot access the shoreline area. Therefore, the common practice is to combine lidar survey data and sedimentation survey data to generate integrated bathymetry for lakes and reservoirs. However, this kind of bathymetry is very expensive, especially for lakes with relatively large areas. The high costs and the lack of data sharing are the main reasons that

bathymetry information is still relatively unused from a global perspective. Under this condition, our approach solely based on freely available satellite data has a unique advantage. Remotely sensed bathymetry can satisfy the needs of most applications since dynamic variations are generated from a long period from 1984 to 2015. Moreover, for reservoirs that have experienced dramatic changes in the last three decades (e.g., Tungabhadra and Gandhi Sagar), nearly full bathymetry can be achieved through remote sensing. Even though the projected bathymetry values have relatively large uncertainties and errors, the algorithm of Tsing et al. (2016) adopted in this study still outperformed other alternative approaches (Getirana et al. 2018).

Even though some small reservoirs (e.g., Lake Success and Mehgaon Tola Tank) are included in this bathymetry dataset, the majority of these small reservoirs cannot be represented due to the limitations of altimetry data. Small water bodies cannot be detected by radar altimeters due to their low spatial resolutions. Although ICESat can capture much smaller lakes, its technical issues after launch significantly reduced its observation capabilities. However, the A-E relationships of the reservoirs from other studies can be adopted to extend the coverage of the bathymetry dataset. For example, Busker et al. (2019) evaluated the volume variations for 137 lakes and reservoirs at a global scale. This study included 66 reservoirs, 36 of which overlapped with our dataset and had similar data quality. For the other 30 reservoirs in Busker et al. (2019), 21 of them have R^2 values of their A-E relationships greater than 0.5. Figure S23 in Appendix A compares the Area-Volume relationships derived from the bathymetry (this study) with those of Yigzaw et al. (2018). Since our results are based on multi-satellite observations instead of hypothetical

bathymetries, they have better overall performance. Thus, the AVE curves derived in this study, representing more than half of the global storage capacity, can be used to supplement the dataset of Yigzaw et al. (2018).

Nonetheless, this dataset has a few limitations that are worth noting. First, for applications that need accurate bathymetry maps (e.g., navigation), the projected bathymetry should be used with caution. Second, results for regulated natural lakes located in high-latitude areas have relatively low quality because they are occasionally covered with ice, which leads to low-quality area estimates. Third, the algorithm did not consider the effects of sedimentation on bathymetry, which could be significant for reservoirs whose dynamic storage fraction is small.

3.5.3. Potential contributions

The dataset from this study can benefit multiple applications across multiple disciplines. First, the high-quality A-E and E-V relationships can better represent the reservoirs in global hydrological models and Earth System Models (Yigzaw et al. 2018). Second, these A-E and E-V relationships can be combined with area estimations from satellite imagery or satellite altimetry data to generate long-term reservoir storage records. The capability to monitor global reservoir storage variations from space has been limited by the availability of radar and lidar altimetry data (Busker et al. 2019; Crétaux et al. 2011; Gao et al. 2012; Yao et al. 2019; Zhang et al. 2014). By introducing ICESat as an additional elevation data source for generating A-E relationships, many more reservoirs can be monitored. By applying these A-E relationships to satellite observations with high temporal resolutions, such as those from the Visible Infrared Imaging Radiometer Suite

(VIIRS) and the Moderate Resolution Imaging Spectroradiometer (MODIS), reservoir storage variations can be estimated in near real-time. Third, the bathymetry maps can be embedded into the SRTM DEM dataset to replace the constant values in water covered areas, which only represent the water elevations during the acquisition time in 2000 (Li et al. 2019b). The DEM with the reservoir bathymetry represented can better support hydrology and hydraulic modeling, especially with regard to flood inundation.

This algorithm is also applicable to large natural lakes whose elevations are available from the G-REALM, Hydroweb, and ICESat datasets. More importantly, this approach can be easily applied to data collected by the newly launched ICESat-2 (September 2018). The Advanced Topographic Laser Altimeter System (ATLAS) onboard ICESat-2 is capable of capturing numerous small lakes and reservoirs, attributed to its improved along-track sampling interval (0.7 m), footprint diameter (17 m), and horizontal track spacing (as narrow as 2 km or less) (Markus et al. 2017). Thus, it is anticipated that the bathymetry dataset can be extended via the addition of thousands of relatively small reservoirs and lakes (Li et al. 2019b). In addition, the Surface Water and Ocean Topography (SWOT) mission (planned for launch in 2022), which can detect water bodies with areas greater than 250 m by 250 m (Biancamaria et al. 2016), will provide full global capabilities for bathymetry mapping. To date, small inland water bodies are normally ignored in almost all global processes and cycles (Downing 2010; Downing et al. 2006; Lehner and Döll 2004), even though they play important roles in various processes, such as climate regulation, carbon cycle, and biodiversity conservation (Downing 2010; Smith et al. 2005; Tranvik et al. 2009).

3.6. Conclusions

In this study, an approach was presented to generate reservoir bathymetry by combining satellite altimetry and imagery data. We utilized multiple satellite altimetry datasets (ICESat, G-REALM, and Hydroweb) in combination with Landsat-based surface water datasets, such as SWO from GSW and monthly water area from GRSAD, to develop a consistent high-resolution 3-D bathymetry dataset for global reservoirs. Meanwhile, for the central part of each reservoir that could not be captured by Landsat, an extrapolation method was adopted to help achieve full bathymetry. The resulting dataset includes 347 reservoirs with a total capacity of 3123 km^3, representing 50% of the global reservoir capacity. Validation against the surveyed bathymetry over four reservoirs indicates the relatively high accuracy and reliability of the remotely sensed bathymetry values, with R^2 values ranging from 0.82 to 0.99 and RMSE values from 0.19 m to 1.65 m. An indirect validation, which compared the remotely sensed A-E and E-V relationships with those derived from *in situ* data for 16 reservoirs, also suggests good agreement. These relationships could be used to monitor the storage variations of global reservoirs, either from satellite altimetry or imagery data. Compared to remotely sensed bathymetry, projected bathymetry has relatively large uncertainties and errors; thus, it should be used with caution, especially for navigation. In addition to reservoirs, the bathymetry values for hundreds of global natural lakes can be obtained using this method. More importantly, this approach can be easily applied to the extensive data provided by ICESat-2, which will cover thousands of small lakes and reservoirs thanks to its high spatial resolution and dense ground tracks. This dataset fills a knowledge gap with regard to comprehensive

bathymetry information across spatial scales and provides important data for future studies involving many aspects of hydrological processes, biogeochemical cycles, and water resources management.

4. TRACKING THE STORAGE VARIATIONS OF GLOBAL RESERVOIRS FROM SPACE

4.1. Introduction

According to the United Nations World Water Development Report (WWAP 2019), over 2 billion people are experiencing high water stress, and about 4 billion people are suffering severe water scarcity for more than one month each year. Due to increasing demand in the industrial and domestic divisions, it is expected that global water demand will continue raising at a nearly constant rate until 2050, contributing to a 20%–30% growth compared to the current water use. Moreover, the changing climate may even intensify this water stress and scarcity. Under this circumstance, reservoirs play an increasingly significant role in water management (e.g., irrigation, hydropower generation, water supply, and flood protection) (Biemans et al. 2011; Cooke et al. 2016; Grigg 1996; Plate 2002; Veldkamp et al. 2017; Votruba and Broža 1989). It was reported that about 30–40% of the global irrigated land relied on reservoirs, and approximately 12% of the global large reservoirs are designed for water supply purposes (WCD 2000). According to the Renewables 2019 Global Status Report (Murdock et al. 2019), hydropower accounted for 60.3% of the renewable electricity production in 2018. Researchers also suggested that the water retained by global reservoirs has long term impacts on global and regional water cycles (Yigzaw et al. 2018; Zhou et al. 2016). However, because gauge observations for reservoir storage are typically not shared and reservoir operation rules are not publicly available, a historical long-term record of

reservoir storage will both improve our understanding about the roles of reservoirs in altering the hydrological cycle and help to calibrate/validate reservoir operation rules in the hydrological models.

Satellite remote sensing provides an unprecedented alternative for monitoring reservoirs. Since the 1990s, satellite radar altimeters have been utilized to measure the water level for large lakes and reservoirs (Birkett 1995). To date, several databases have been developed to monitor the water level of inland waters at a global scale, for example, the Global Reservoir and Lake Monitor (G-REALM) (Birkett et al. 2011), the Hydroweb database (Crétaux et al. 2011), and the Database for Hydrological Time Series of Inland Waters (DAHITI) (Schwatke et al. 2015). Meanwhile, the global surface water area variations of lakes and reservoirs have been assessed from various satellite missions such as Landsat and Moderate Resolution Imaging Spectroradiometer (MODIS) (Donchyts et al. 2016; Khandelwal et al. 2017; Pekel et al. 2016; Yao et al. 2019; Zhao and Gao 2018). Recently, several studies have focused on generating consistent satellite-based reservoir storage estimations using elevation and area data collected from multiple missions. (Busker et al. 2019; Crétaux et al. 2011; Gao et al. 2012; Li et al. 2019a; Song et al. 2013; Yao et al. 2018; Zhang et al. 2014). For example, Gao et al. (2012) monitored storage values for 34 global reservoirs from 1992 to 2010 by combining water surface areas from MODIS with water elevations from satellite radar altimetry which represented 15% of the total global reservoir capacity. The Hydroweb database (http://hydroweb.theia-land.fr/) estimates the storage changes for about 60 large lakes and reservoirs since 1992, using multi-source satellite imagery (e.g., Modis, Landsat) and radar altimetry data (Crétaux et

al. 2011). More recently, Busker et al. (2019) analyzed the volume variations between 1984 and 2015 for 137 lakes and reservoirs at a global scale by combining water area values from the JRC Global Surface Water (GSW) dataset (Pekel et al. 2016) and elevation values from the DAHITI. However, these studies are limited to the spatial distribution and the number of reservoirs, which cannot fully represent the global storage variations.

Meanwhile, global reservoir information has been incorporated into some databases, such as the Global Lakes and Wetlands Database (GLWD) (Lehner and Döll 2004), the Global Reservoir and Dam database (GRanD) (Lehner et al. 2011a, b), and the HydroLAKES database (Messager et al. 2016). While these databases provide attribute information and digital maps for global reservoirs, they only offer static values (e.g., area, elevation, shoreline length, and storage). More recently, Yigzaw et al. (2018) selected five hypothesized reservoir geometric shapes to develop a global storage-area-depth data set for over 6,800 reservoirs, but storage variation data of these global reservoirs are still not available.

With the ongoing climate change and the escalating water crisis, the response of reservoirs is still unclear across spatial scales. Previous studies mainly have used reservoir capacity values—but not the storage variations—to estimate the global reservoir water impoundments (Chao et al. 2008; Lettenmaier and Milly 2009). For example, Chao et al. (2008) reported that the cumulative impounded water by global reservoirs increased from under 1000 km^3 in 1950 to about 10,800 km^3 in 2007, reducing the magnitude of global sea level rise by 30 mm. Meanwhile, our knowledge of storage variations at the basin scale is still lacking. To our knowledge, Zhou et al. (2016) is the only study that focused on

analyzing global reservoir storage variations at the basin scale (32 global river basins), with the 166 largest reservoirs simulated using the Variable Infiltration Capacity (VIC) model from 1948 to 2010. However, the modeled storage values have large uncertainties and errors because it is challenging to accurately represent the reservoir operating rules in the models. In addition, they scaled the simulated reservoir storage values to the basin scale, which can introduce extra uncertainties. Moreover, the construction of reservoirs slowed down during the late 20th century (Lettenmaier and Milly 2009), with most new reservoirs in the developing countries of Asia, South America, and Africa (Zarfl et al. 2015). Given this change, it is important to evaluate the performance and effects of the newly built reservoirs, which can provide valuable information for future planning and reservoir management.

Therefore, long-term storage records for global reservoirs are critically needed for water management applications across scales. In this study, we used multi-source remote sensing data—in combination with an approved area-depth-storage database—to estimate the monthly storage variations for global 7245 reservoirs. Validation against the *in situ* data for 277 reservoirs indicates that the estimated storages have an overall good accuracy. Based on the individual storage records, we evaluated the storage variations and their responses to climate variability—using the El Niño-Southern Oscillation (ENSO) as an indicator—at the global, continental, and river basin scales. Furthermore, the impacts of newly constructed reservoirs in the 21st century were also assessed. Lastly, we analyzed the storage variations for reservoirs with different functions.

4.2. Data and Methods

4.2.1. Data

4.2.1.1. Global Reservoir and Dam Database (GRanD)

GRanD (Lehner et al. 2011a, b) describes geospatially referenced dams and their associated reservoirs, most of which have a storage capacity of more than 0.1 km^3. It also provides multiple attributes, such as dam height and length, reservoir area, and storage. GRanD v1.1 contains 6,862 records with a cumulative reservoir storage capacity of 6,197 km^3. The recently updated GRanD v1.3 extends the database by 458 dams (7320 in total), which increases the total capacity to 6811 km^3. In addition, it integrates some changes and corrections to the attribute information and updates many reservoir polygons of the previous versions. It should be noted that 70 dams do not have an associated reservoir so that the GRanD v1.3 contains 7250 reservoir polygons.

4.2.1.2. Global Reservoir Surface Area Dataset (GRSAD)

Based on Landsat imageries acquired from 1984 to 2015, GSW dataset provides Earth's surface water maps at a 30 m high resolution (Pekel et al. 2016). However, the water area may be underestimated because of the effects of clouds contamination and Landsat-7's Scan Line Corrector (SLC) failure. GRSAD (Zhao and Gao 2018) corrected the underestimations and estimated the monthly water area for each reservoir included in GRanD v1.1. Recently, with GRanD updated to version 1.3 and GSW dataset extended to the year of 2018, GRSAD was also updated accordingly to a new version which provides surface water areas for 7245 reservoirs from 1984 to 2018. It should be noted that five very small reservoirs (with area values less than 1 km^2) were not included in GRSAD

because they have dried up and their surface water areas were not available from GSW dataset. The estimated areas were applied to the Area-Storage (A-V) relationships to generate the storage time series. Although Landsat observations for areas such as the United States and Australia are sufficient for seasonal and interannual evaluations from the early 1980s onward, the temporal coverage for other regions is relatively low before the launch of Landsat-7 in 1999 (Arvidson et al. 2001; Pickens et al. 2020; Wulder et al. 2016). Therefore, the seasonal and interannual variations of reservoir storage were analyzed starting from 1999 in this study.

4.2.1.3. Global Reservoir Bathymetry Dataset (GRBD)

GRBD (Li et al. 2020) includes high-resolution bathymetric maps for 347 global reservoirs, which were generated from multi-source satellite datasets. To generate the bathymetry, the Surface Water Occurrence (SWO) image provided by GSW was used as the base map. Two methods were adopted to generate the A-E relationships according to the altimetry data source—lidar altimetry data (i.e., Ice, Cloud, and land Elevation Satellite (ICESat)) and radar altimetry datasets (i.e., G-REALM and Hydroweb datasets). Then, the A-E relationship was in turn applied to the SWO image to obtain the bathymetry values. From the 3-D bathymetric maps, the Area-Volume-Elevation (AVE) relationships can be derived, which have been validated to have high accuracy and reliability (Li et al. 2020).

4.2.2. Methods

In this study, the monthly storage time series from 1999 to 2018 was generated by applying GRSAD area estimations to the A-V relationships for 7245 reservoirs (from

GRanD v 1.3). The A-V relationships were adopted from two sources: the global bathymetry dataset (for 347 reservoirs) by Li et al. (2020), and the modified simulation method of Yigzaw et al. (2018) (for the remaining 6898 reservoirs).

4.2.2.1. Storage estimation using the A-V relationships from the reservoir bathymetry dataset

From the 3-D reservoir bathymetry information, the storage at a given area value (A) can be obtained by integration. First, the corresponding elevation can be calculated from the A-E relationship, which is regarded as the baseline contour. Then, the storage between the baseline and elevation at capacity can be obtained, which is subtracted from the storage capacity to calculate the storage value (V) corresponding to A (equation (4.1)).

$$V = V_c - \sum_{i=1}^{n-1} \frac{(h_{i+1} - h_i)(A_{i+1} + A_i)}{2} \quad (4.1)$$

where n is the number of contours between the elevation at capacity and the elevation associated with the observed area (i.e., the number of contours between h_c and h) for a given month; A_i is the surface area enclosed by the i^{th} contour; and h_i is the elevation of the i^{th} contour.

4.2.2.2. Storage estimation from simulated A-V relationships

In this study, we modified the simulation method developed by Yigzaw et al. (2018) in the following ways: First, we improved the representation of reservoir area at capacity. Yigzaw et al. (2018) assumed that the polygon area represented the area that reached the storage capacity. However, the reservoir polygons were mostly generated from the static Shuttle Radar Topography Mission (SRTM) DEM, which may have

occurred in a low fill or dry season for a given reservoir. To minimize this kind of uncertainty, we calculated the 95th percentile area value for each reservoir from the GRSAD dataset, and compared it with the areas provided in GRanD. The larger one was selected to represent the area at capacity. Second, Yigzaw et al. (2018) simulated the surface shapes of reservoirs. However, it is difficult to simulate the surface shapes due to their complexity. Therefore, we combined the dam profile and bottom shapes to represent the surface area. Specifically, we selected three possible bottom shapes (i.e., parabolic, linear, and square root), in combination with four dam profile shapes (i.e., prism, bowl, wedge, and concave wedge), to obtain twelve reservoir geometries. This provides more options than the method by Yigzaw et al. (2018), which selected five geometries with a parabolic bottom. The schematic of a reservoir geometry with a parabolic bottom and a prism profile is shown in Figure 4.1a, and the selected bottom and profile shapes are demonstrated in Figure 4.1b.

The storage estimation using simulated reservoir geometry is summarized in the following steps:

Step 1. Determining the optimal reservoir geometry

For each reservoir, the total storage was calculated for all of the twelve possible geometries (Figure 4.1b) by integrating the area with respect to depth. The geometry with the estimated total storage closest to the reported capacity value in GRanD was selected as the optimal geometry.

In Figure 4.1a, the reservoir geometry with a parabolic bottom and a prism profile is selected to demonstrate the simulation process. As shown in Figure 4.1c, A_0 represents

the area at capacity that is associated with a depth of D_0, which was derived from the dam height H ($D_0 = 0.95\,H$). It should be noted that for reservoirs with no available dam heights, D_0 was substituted by the average depth, which was calculated using the storage and area values at capacity. Then, we defined a random layer with an area of A_i, which is z meters below the top layer. Based on the profile and bottom shapes, A_i can be expressed as a function of z (equation (4.2)).

$$A_i = A_0 \sqrt{1 - \frac{z}{D_0}} \tag{4.2}$$

The estimated total storage (V_0) was calculated by integrating the area (A_i) with respect to the depth using equation (4.3).

$$V_0 = \int_0^D A_0 \sqrt{1 - \frac{z}{D_0}}\; dz = \frac{2}{3}\, A_0 D_0 \tag{4.3}$$

Similarly, the estimated total storage (V_0) values for the other geometries were obtained using the equations in Table 4.1. Then, the reported storage capacity value (V_c) was compared with the estimated total storages, and the geometry with the closest estimated value was selected. It should be noted that some geometries have the same estimated storage values, such as a prism profile with a linear bottom and a bowl profile with a parabolic bottom (Table 4.1). In this case, either one was selected, but the storage calculation (Step 2) was not affected by the selection of geometry.

Step 2. Generate the storage time series from the area values

For a given area value (A) from GRSAD, equations (4.2) and (4.3) were combined to calculate its corresponding storage value (V) from equation (4.4).

$$V = \frac{2}{3}AD = \frac{2}{3}A\,(D_0 - z') = \frac{2}{3}AD_0(\frac{A}{A_0})^2 \quad (4.4)$$

where D is the depth associated with the layer of A; and $z' = D_0 - D$, which is the vertical distance between the layers A and A_0. The storage time series was then obtained by applying the area values to equation (4.4). The storage equations for other geometries are summarized in Table 4.1.

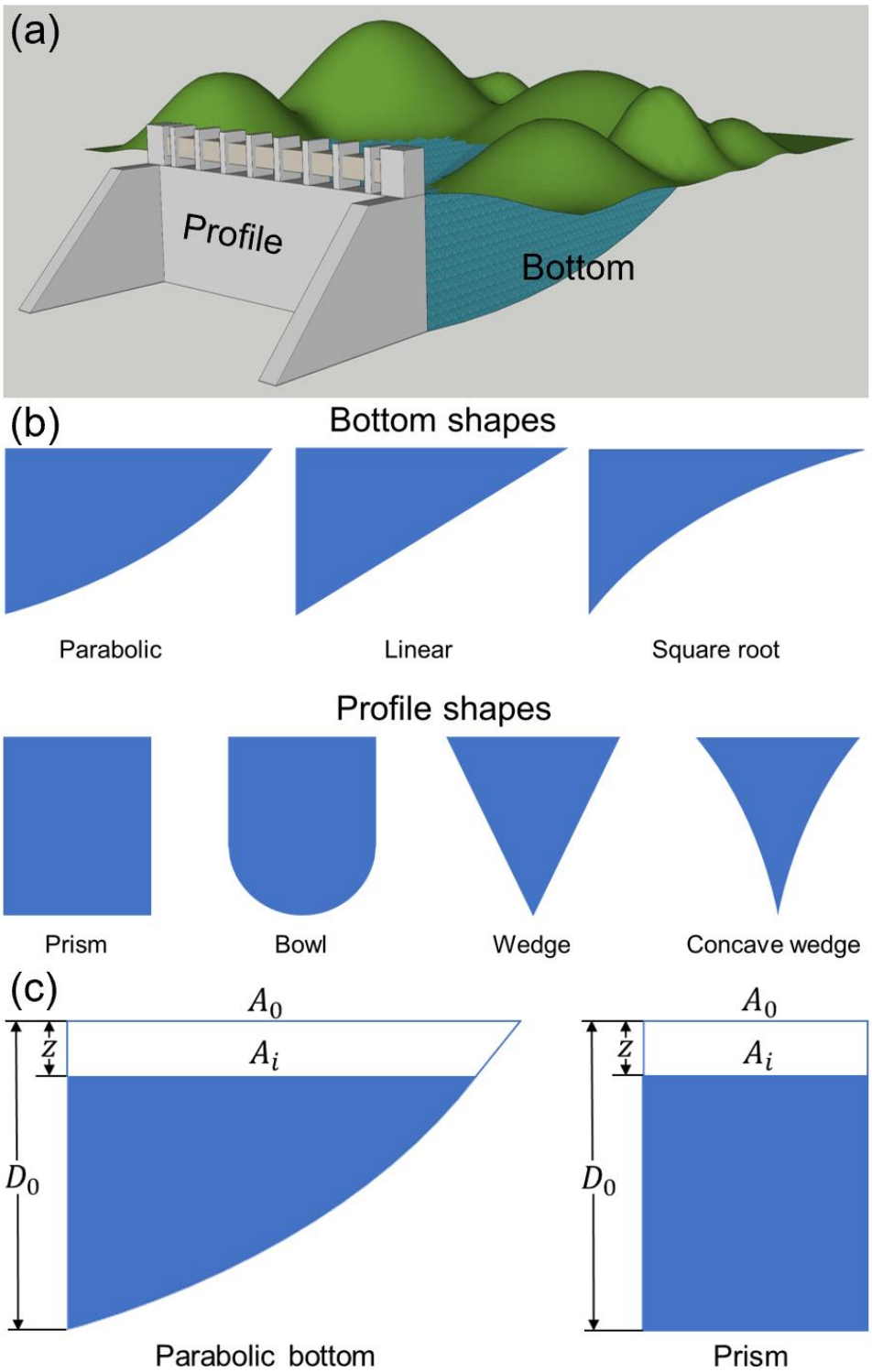

Figure 4.1 (a) A schematic of a reservoir geometry with a parabolic bottom and a prism profile, (b) all of the selected bottom and profile shapes, and (c) the parameters that correspond to the geometry in (a).

Table 4.1 Summary of simulated area and storage equations for each of the geometry combinations

	Parabolic	Linear	Square root
Prism	$A_i = A_0\sqrt{1-\frac{z}{D_0}}$ $V_0 = \int_0^{D_0} A_i\,dz = \frac{2}{3}\,A_0 D_0$ $V = \frac{2}{3}AD = \frac{2}{3}AD_0(\frac{A}{A_0})^2$	$A_i = A_0\,(1-\frac{z}{D_0})$ $V_0 = \int_0^{D_0} A_i\,dz = \frac{1}{2}\,A_0\,D_0$ $V = \frac{1}{2}AD = \frac{1}{2}AD_0\frac{A}{A_0}$	$A_i = A_0\,(1-\frac{z}{D_0})^2$ $V_0 = \int_0^{D_0} A_i\,dz = \frac{1}{3}\,A_0\,D_0$ $V = \frac{1}{3}AD = \frac{1}{3}AD_0(\frac{A}{A_0})^{\frac{1}{2}}$
Bowl	$A_i = A_0\sqrt{1-\frac{z}{D_0}}\sqrt{1-\frac{z}{D_0}}$ $V_0 = \int_0^{D_0} A_i\,dz = \frac{1}{2}\,A_0\,D_0$ $V = \frac{1}{2}AD = \frac{1}{2}AD_0\frac{A}{A_0}$	$A_i = A_0(1-\frac{z}{D_0})\sqrt{1-\frac{z}{D_0}}$ $V_0 = \int_0^{D_0} A_i\,dz = \frac{2}{5}\,A_0\,D_0$ $V = \frac{2}{5}AD = \frac{2}{5}AD_0(\frac{A}{A_0})^{\frac{2}{3}}$	$A_i = A_0\,(1-\frac{z}{D_0})^2\sqrt{1-\frac{z}{D_0}}$ $V_0 = \int_0^{D_0} A_i\,dz = \frac{2}{7}\,A_0\,D_0$ $V = \frac{2}{7}AD = \frac{2}{7}AD_0(\frac{A}{A_0})^{\frac{2}{5}}$
Wedge	$A_i = A_0\sqrt{1-\frac{z}{D_0}}\,(1-\frac{z}{D_0})$ $V_0 = \int_0^{D_0} A_i\,dz = \frac{2}{5}\,A_0\,D_0$ $V = \frac{2}{5}AD = \frac{2}{5}AD_0(\frac{A}{A_0})^{\frac{2}{3}}$	$A_i = A_0\,(1-\frac{z}{D_0})(1-\frac{z}{D_0})$ $V_0 = \int_0^{D_0} A_i\,dz = \frac{1}{3}\,A_0\,D_0$ $V = \frac{1}{3}AD = \frac{1}{3}AD_0(\frac{A}{A_0})^{\frac{1}{2}}$	$A_i = A_0\,(1-\frac{z}{D_0})^2(1-\frac{z}{D_0})$ $V_0 = \int_0^{D_0} A_i\,dz = \frac{1}{4}\,A_0\,D_0$ $V = \frac{1}{4}AD = \frac{1}{4}AD_0(\frac{A}{A_0})^{\frac{1}{3}}$
Concave wedge	$A_i = A_0\sqrt{1-\frac{z}{D_0}}\,(1-\frac{z}{D_0})^2$ $V_0 = \int_0^{D_0} A_i\,dz = \frac{2}{7}\,A_0\,D_0$ $V = \frac{2}{7}AD = \frac{2}{7}AD_0(\frac{A}{A_0})^{\frac{2}{5}}$	$A_i = A_0\,(1-\frac{z}{D_0})\,(1-\frac{z}{D_0})^2$ $V_0 = \int_0^{D_0} A_i\,dz = \frac{1}{4}\,A_0\,D_0$ $V = \frac{1}{4}AD = \frac{1}{4}AD_0(\frac{A}{A_0})^{\frac{1}{3}}$	$A_i = A_0\,(1-\frac{z}{D_0})^2\,(1-\frac{z}{D_0})^2$ $V_0 = \int_0^{D_0} A_i\,dz = \frac{1}{5}\,A_0\,D_0$ $V = \frac{1}{5}AD = \frac{1}{5}AD_0(\frac{A}{A_0})^{\frac{1}{4}}$

4.2.2.3. Error metrics

The coefficients of determination (R^2), the mean bias errors (MBE), and the normalized root-mean-square errors (NRMSE) were used as the error metrics to evaluate the storage estimations. The MBE and NRMSE are defined in equations (4.5) and (4.6), respectively.

$$\text{MBE} = \frac{\sum_{i=1}^{n}(\hat{V}_i - V_i)}{n} \tag{4.5}$$

$$\mathrm{NRMSE} = \frac{\sqrt{\frac{\sum_{i=1}^{n}(\hat{V}_i - V_i)^2}{n}}}{V_{max} - V_{min}} \times 100\% \quad (4.6)$$

where $\hat{V}_i$ and V_i represent the estimated and *in situ* storage values on a monthly basis, *n* is the number of pairs, and V_{max} and V_{min} are the maximum and minimum *in situ* storage values.

4.3. Results

4.3.1. Evaluation of storage estimations

In this study, we selected 49 reservoirs (United States: 22, Australia: 5, and India: 22) to validate the storage results using the A-V relationships from the bathymetry dataset, and to compare the performance from the two storage estimation methods. A total of 228 reservoirs from the United States and Australia were further used to evaluate the performance of the simulation method. The *in situ* data were acquired from the United States Geological Survey (USGS), the United States Bureau of Recreation (USBR), the United States Army Corps of Engineers (USACE), the California Data Exchange Center (CDEC), the Australia Bureau of Meteorology (BOM), and the India Water Resources Information System (WRIS). Because the *in situ* storages for reservoirs in the United States and Australia were from 1984 to 2015 and the Landsat observations for those reservoirs were available over this period, all these *in situ* values were used for validation. On the other hand, the gauge observations from India were generally from 2000 to 2018 (except some built after 2000). The validation results are shown separately according to the period of the *in situ* data. Figure 4.2 shows the comparison of the estimated storages (from the two methods) with the *in situ* values for the reservoirs in the United States and

Australia, and the corresponding statistics are summarized in Table 4.2. Figure 4.3 and Table 4.3 indicate the validation results for the reservoirs in India.

According to Figure 4.2, the estimated storage values are in overall good agreement with the observations. For the storage estimations using the bathymetry-based A-V relationships, the R^2, MBE, and NRMSE values range from 0.41 to 0.99, -1.32 km^3 to 0.63 km^3, and 4.40% to 25.90%, respectively. The results based on the simulation method have R^2, MBE, and NRMSE values range from 0.41 to 0.99, -1.84 km^3 to 1.40 km^3, and 6.26% to 58.65%, respectively. It should be noted that the storage estimates from the simulation method have a relatively large bias in some cases (such as with the Clear Lake Reservoir and the Navajo Reservoir). By comparison, the bathymetry-based method has a more reliable performance. Although only 347 reservoirs have bathymetry data, they represent a total capacity of 3217 km^3—accounting for 46.87% of total global capacity (according to GRanD v1.3), which can help reduce the overall uncertainty.

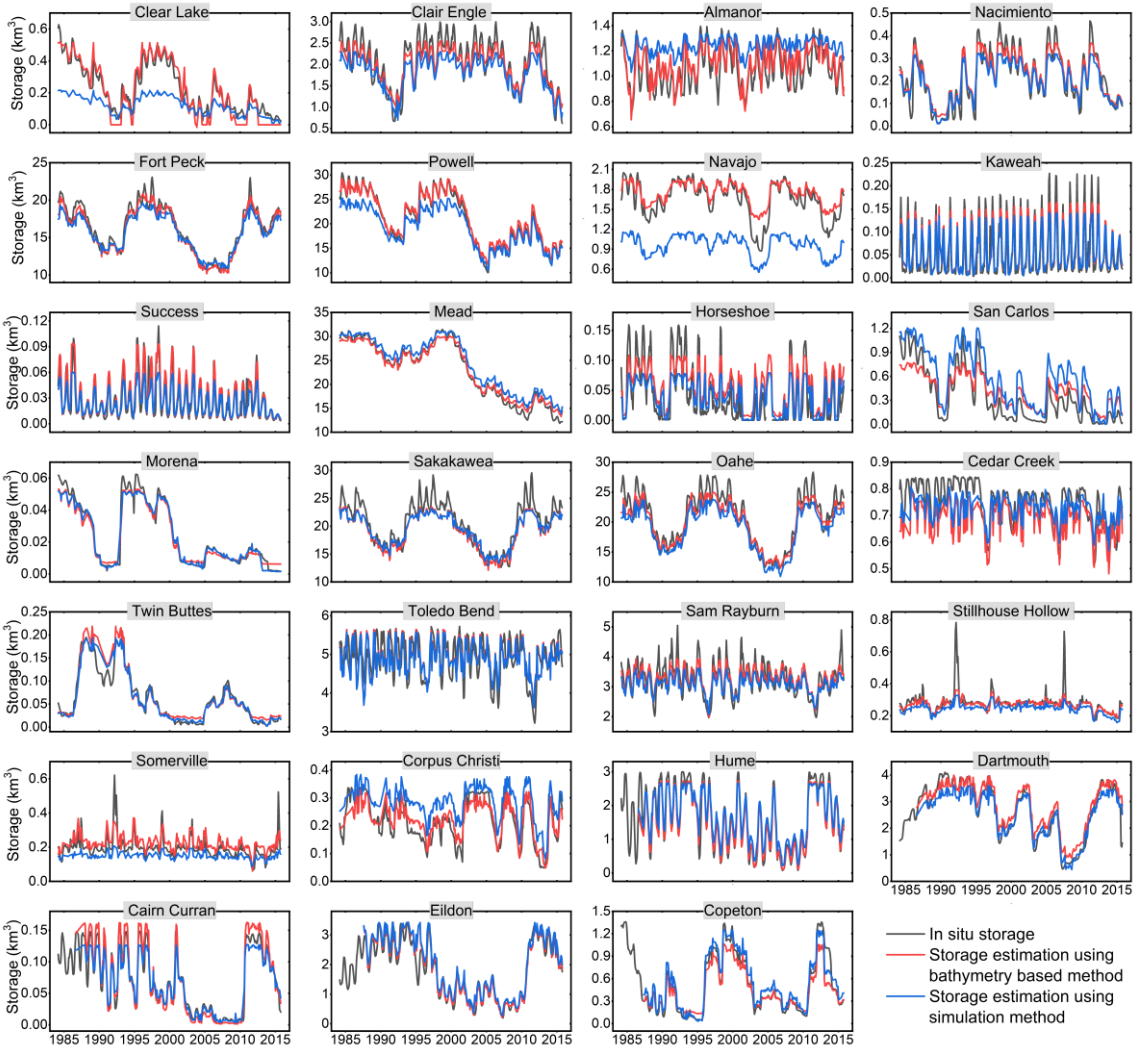

Figure 4.2 Comparison of storage estimations against *in situ* values for reservoirs in the United States and Australia.

Table 4.2 Validation results over the reservoirs in the United States and Australia.

GRanD ID	Reservoir name	Ctry	[a]Cap. (km^3)	R^2		MBE (km^3)		NRMSE	
				[b]Bathy.	[c]SIM.	Bathy.	SIM.	Bathy.	SIM.
119	Clear Lake	U.S.	0.56	0.93	0.90	-0.0052	-0.073	9.17%	23.42%
131	Clair Engle	U.S.	3.02	0.89	0.88	-0.087	-0.27	10.48%	15.52%
138	Almanor	U.S.	1.61	0.61	0.61	0.046	0.18	16.10%	32.44%
231	Nacimiento	U.S.	0.47	0.89	0.87	0.0070	-0.015	9.34%	11.23%
307	Fort Peck	U.S.	22.77	0.96	0.96	0.63	-0.68	6.27%	8.67%
597	Powell	U.S.	30.00	0.98	0.98	0.53	-1.60	4.74%	10.86%
601	Navajo	U.S.	2.11	0.94	0.95	0.097	-0.68	13.25%	58.65%
605	Kaweah	U.S.	0.23	0.73	0.71	0.0063	0.0034	13.25%	13.60%
609	Success	U.S.	0.10	0.82	0.80	0.0036	-0.0020	9.72%	10.76%
610	Mead	U.S.	34.07	0.99	0.99	0.094	1.40	4.40%	8.34%
640	Horseshoe	U.S.	0.13	0.73	0.68	0.014	-0.0002	17.74%	17.79%
656	San Carlos	U.S.	1.12	0.90	0.90	0.067	0.24	13.86%	22.23%
669	Morena	U.S.	0.062	0.98	0.97	-0.0012	-0.0011	6.54%	6.26%
753	Sakakawea	U.S.	29.38	0.90	0.89	-1.32	-1.05	11.43%	11.33%
870	Oahe	U.S.	28.35	0.92	0.92	-0.86	-1.84	9.87%	14.09%
1230	Cedar Creek	U.S.	0.80	0.44	0.44	-0.062	-0.022	25.90%	18.77%
1263	Twin Buttes	U.S.	0.23	0.91	0.93	0.0069	0.0019	10.36%	7.66%
1269	Toledo Bend	U.S.	5.52	0.41	0.41	0.0049	-0.023	15.94%	15.83%
1275	Sam Rayburn	U.S.	3.55	0.65	0.65	-0.026	-0.17	10.75%	12.79%
1277	Stillhouse Hollow	U.S.	0.28	0.57	0.53	-0.011	-0.036	8.21%	10.09%
1296	Somerville	U.S.	0.62	0.61	0.57	0.029	-0.046	8.79%	12.17%
1317	Corpus Christi	U.S.	0.32	0.81	0.79	0.0041	0.066	12.55%	26.22%
6628	Hume	AU.	3.04	0.93	0.92	-0.063	0.079	8.87%	10.44%
6637	Dartmouth	AU.	3.86	0.93	0.93	0.18	-0.14	9.71%	9.34%
6647	Cairn Curran	AU.	0.15	0.95	0.94	0.0042	-0.003	10.74%	8.66%
6653	Eildon	AU.	3.39	0.92	0.93	0.075	0.17	9.27%	9.98%
6733	Copeton	AU.	1.36	0.94	0.94	-0.038	0.056	9.75%	8.22%
	Average			0.82	0.81	-0.025	-0.17	11.00%	15.38%

[a]Cap. represents the reservoir storage capacity value, [b]Bathy. represents the results from the bathymetry-based method, and [c]SIM. represents the results from the simulation method.

Similarly, the validations over the Indian reservoirs also show encouraging results. For the storage estimations from the bathymetry, the R^2, MBE, and NRMSE range from 0.67 to 0.95, -0.16 km^3 to 0.51 km^3, and 6.96% to 30.80%, respectively. While for the simulation method, the R^2, MBE, and NRMSE range from 0.67 to 0.95, -0.11 km^3 to 4.92

km^3, and 9.00% to 127.73%, respectively. It is obvious that the simulation method has a large bias in some reservoirs, for example, the Rana Pratap Sagar, Yeleru, and Nagarjuna Sagar, with NRMSE values of 127.73%, 87.14%, and 73.09%, respectively. However, the simulated storage values for these reservoirs have good correlations with the *in situ* data, with R^2 values of 0.80, 0.89, and 0.81, respectively. Moreover, the simulation method has an overall overestimation with positive MBE values for all the reservoirs except Tawa.

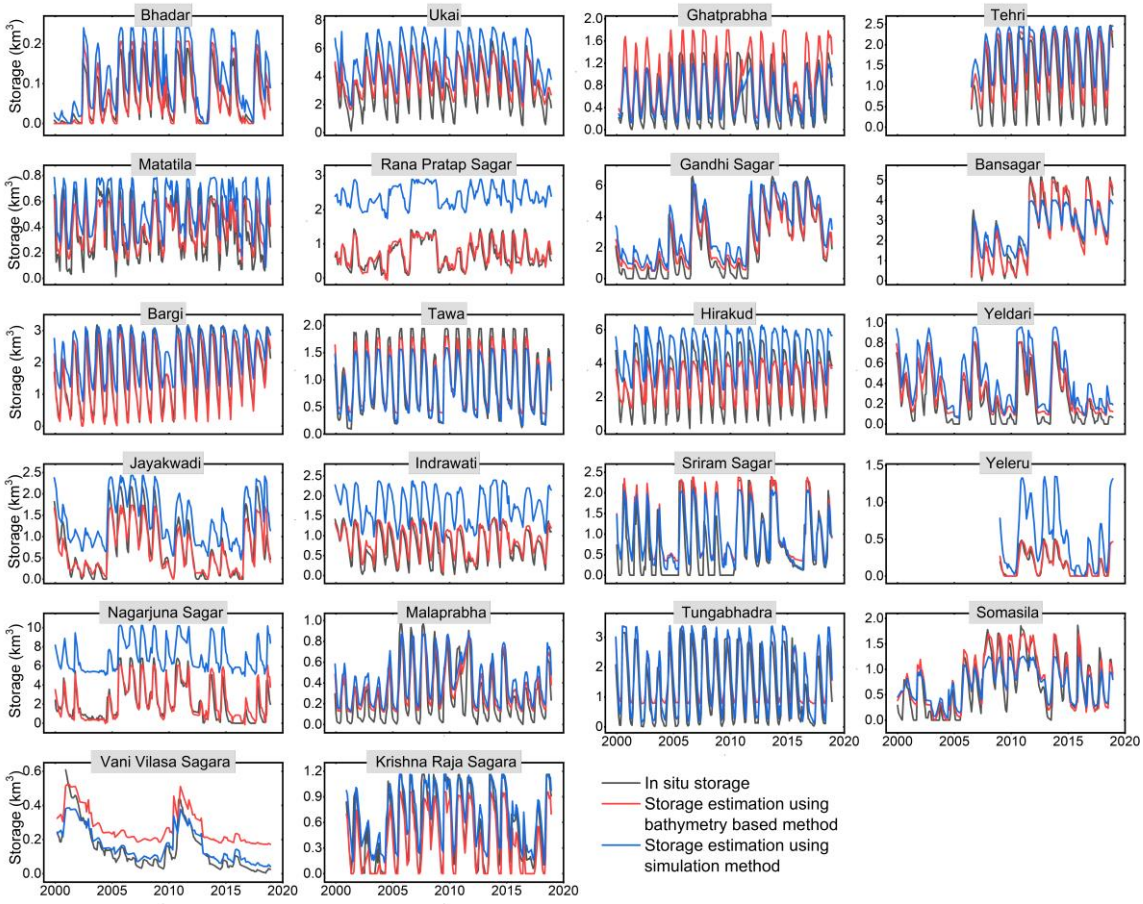

Figure 4.3 Comparison of storage estimations against *in situ* values for reservoirs in India.

Table 4.3 Validation results over the reservoirs in India.

GRanD ID	Reservoir name	[a]Cap. (km^3)	R^2		MBE		NRMSE	
			[b]Bathy.	[c]SIM.	Bathy.	SIM.	Bathy.	SIM.
4735	Bhadar	0.19	0.78	0.78	0.0076	0.050	18.78%	33.63%
4739	Ukai	6.62	0.86	0.86	0.51	1.91	13.60%	31.50%
4773	Ghatprabha	1.39	0.67	0.68	0.31	0.042	30.80%	20.34%
4795	Tehri	2.62	0.79	0.78	0.29	0.58	19.67%	29.29%
4826	Matatila	0.71	0.68	0.67	0.030	0.18	17.39%	31.32%
4836	Rana Pratap Sagar	1.44	0.80	0.80	0.058	1.74	13.32%	127.73%
4843	Gandhi Sagar	6.83	0.92	0.91	0.35	0.94	10.74%	17.32%
4859	Bansagar	5.17	0.95	0.95	-0.051	0.071	6.96%	12.10%
4881	Bargi	3.18	0.85	0.84	-0.021	0.64	12.29%	25.25%
4885	Tawa	1.94	0.82	0.82	-0.0074	-0.11	15.00%	16.51%
4898	Hirakud	5.38	0.80	0.79	0.0037	1.76	15.82%	36.46%
4938	Yeldari	0.82	0.90	0.88	0.078	0.20	13.57%	27.05%
4942	Jayakwadi	2.17	0.87	0.87	-0.074	0.65	12.01%	31.85%
4943	Indrawati	1.46	0.84	0.84	0.13	1.01	14.38%	70.76%
4946	Sriram Sagar	2.30	0.73	0.71	0.31	0.23	22.36%	21.10%
4978	Yeleru	0.51	0.90	0.89	-0.00046	0.35	10.38%	87.14%
4985	Nagarjuna Sagar	6.84	0.82	0.81	0.13	4.92	12.58%	73.09%
4992	Malaprabha	0.97	0.76	0.75	0.08	0.15	15.83%	20.53%
4994	Tungabhadra	3.28	0.75	0.77	0.48	0.36	22.16%	19.86%
4997	Somasila	1.99	0.82	0.80	0.12	0.022	13.64%	14.91%
5000	Vani Vilasa Sagara	0.80	0.91	0.89	0.13	0.021	22.19%	9.00%
5009	Krishna Raja Sagara	1.16	0.82	0.81	-0.16	0.13	20.13%	18.61%
	Average		0.82	0.81	0.12	0.72	16.07%	35.24%

[a]Cap. represents the reservoir storage capacity value, [b]Bathy. represents the results from the bathymetry-based method, and [c]SIM. represents the results from the simulation method.

To further validate the simulation method, we selected 228 reservoirs from the United States and Australia to compare the simulated storages with the in situ values (Figure 4.4). The total simulated storages of these reservoirs agree well with the counterpart gauge observations from 1984 to 2015 (Figure 4.4a), with an R^2 value of 0.96 (Figure 4.4b). In addition, we compared the monthly mean value of each reservoir during this period, which shows a very good agreement (Figure 4.4c). Therefore, it can be

indicated that the simulated storage values are overall accurate and reliable, which laid a solid foundation for evaluating the variations across spatial scales.

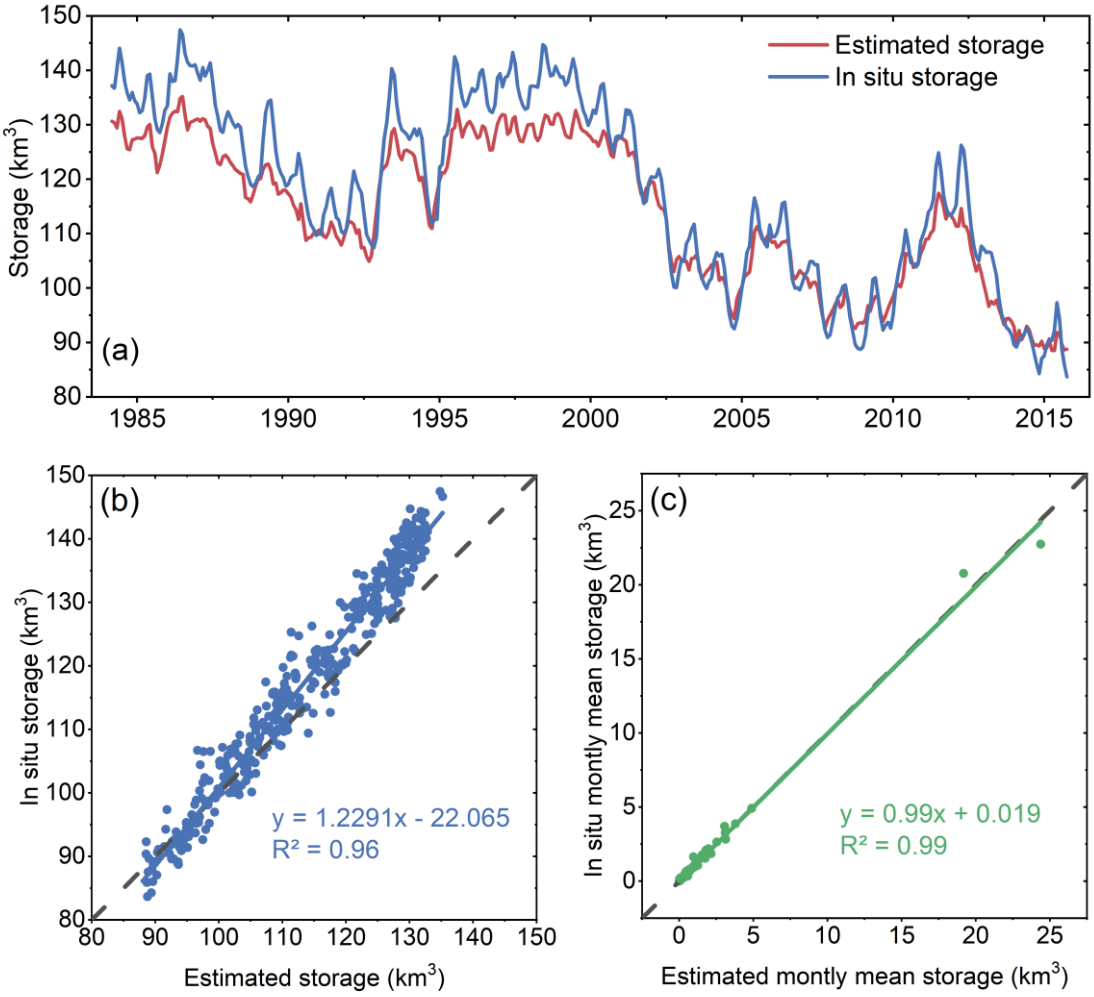

Figure 4.4 Comparison of the simulated storage values with the *in situ* observations from 1984 to 2015 over 228 reservoirs in the United States and Australia: (a) the total monthly storage time series, (b) the corresponding scatter plots of the storage pairs in (a), and (c) comparison of monthly mean storages for these reservoirs.

The above mentioned 277 reservoirs were used to evaluate the uncertainty of the storage dataset. For each month from 1984 to 2015, the total estimated storage of these 277 reservoirs was compared with the total *in situ* storage to calculate the NRMSE (i.e., 4.15%) to represent the overall uncertainty of the dataset. It should be noted that this

overall NRMSE value is smaller than the averaged NRMSE value (22.45%) of the 277 individual reservoirs. This is due to the offset of overestimation and underestimation for these 277 validated reservoirs. Because this study focused on the evaluation of storage variations across large scales (basin, continental, and global), it is reasonable to use 4.15% to represent the uncertainty of the storage estimations.

Because the simulation method relies on the inputs of dam height and the reservoir area and storage at capacity, the reliability of these attributes in GRanD determines the accuracy. The discrepancies of these inputs can explain the large bias observed in some reservoirs. However, for most of the reservoirs, the simulated storages agree well with the *in situ* observations. It is worth noting that these large biases have minor effects on the evaluation of change rate as the simulated storages have good correlations with the *in situ* values. For example, simulated storages resulted in a large error in Rana Pratap Sagar Reservoir with an NRMSE of 127.73%, but they correlated well with the *in situ* data with an R^2 value of 0.80. The change rate derived from the simulated time series is 0.006 km^3/yr, which is consistent with the value calculated from the *in situ* data (0.005 km^3/yr).

Overall, the simulation method performed better in the United States and Australia (with an average NRMSE of 15.38%) than that in India (with an average NRMSE of 35.24%). This is because the storage capacity values from GRanD are larger than those from India-WRIS (Figure S1a in Appendix B). According to the GRanD technical report, the storage capacity values in GRanD can be “maximum capacity”, “gross capacity”, “normal capacity”, “live capacity” or “minimum capacity”, and they are not distinguished in the dataset. While the capacity values provided by India-WRIS are “live capacity” and

the *in situ* observations are also live storages. The bias between the capacity values can explain the relatively large error of the simulation method. For example, the storage capacity value of Rana Pratap Sagar Reservoir from GRanD (2.90 km^3) is twice as much as the capacity from India-WRIS (1.436 km^3), which caused a large error (with an NRMSE of 127.73%). While for the reservoirs in the United States and Australia, the storage capacity values from GRanD have a good agreement with that from water management agencies (Figure S1b in Appendix B). Moreover, the comparison of storage capacity values also indicates that the attributes provided by GRanD are reliable.

4.3.2. Storage variations across spatial scales

The reservoir storage variations were first examined at the global and continental scales, with the time series and the associated statistics shown in Figure 4.5 and Table 4.4. In addition to the absolute storage, we also examined the reservoir normalized storage—which is defined as the ratio of the actual storage over the storage capacity—to evaluate the relative storage variations. Similarly, the normalized storage at the global (or continental) scale is defined as the ratio of the total estimated storage to the corresponding total capacity. The mean values were generated from the monthly estimations from 1999 to 2018, and the storage trends indicate the average annual change.

The global storage time series shows a nearly continuous increase during the last two decades (Figure 4.5), with a mean value of 4351.98 ± 181.35 km^3 (mean ± std) and a growth rate of 27.44 ± 0.96 km^3/yr (Table 4.4). However, the normalized storage has a clear decreasing trend with a rate of -9.08 ± 0.57 10^{-4}/yr. Asia holds the most number of reservoirs (2352) and the highest storage capacity (2382.57 km^3), which also experienced

the most rapid increase with a growth of 20.53 ± 0.73 km^3/yr, accounting for 74.82% of the global trend. In addition, Asia has a similar growth pattern as that of the entire globe (with an R^2 value of 0.89). However, the normalized storage in Asia does not show a significant trend. Compared to Asia, North America contains a similar number of reservoirs (2284) but with less capacity (1602.57 km^3) and a much slower expansion (3.07 ± 0.33 km^3/yr). However, its normalized storage shows a significant increase (8.84 ± 2.18 10^{-4}/yr), which makes it the only continent with an increasing trend. Africa and South America have similar storage capacities, which account for 15.59% and 14.07% of the global capacity, respectively. Additionally, their variations show consistent trends with regard to increasing storage (1.06 ± 0.33 and 1.50 ± 0.48 km^3/yr) but decreasing normalized storages (-11.02 ± 3.31 and -18.72 ± 5.08 10^{-4}/yr). The storage in Europe is relatively stable, with a low change rate (0.51 ± 0.09 km^3/yr). Although Oceania only accounts for 1.45% of global storage capacity, its storage has the largest interannual variation amongst all of the continents.

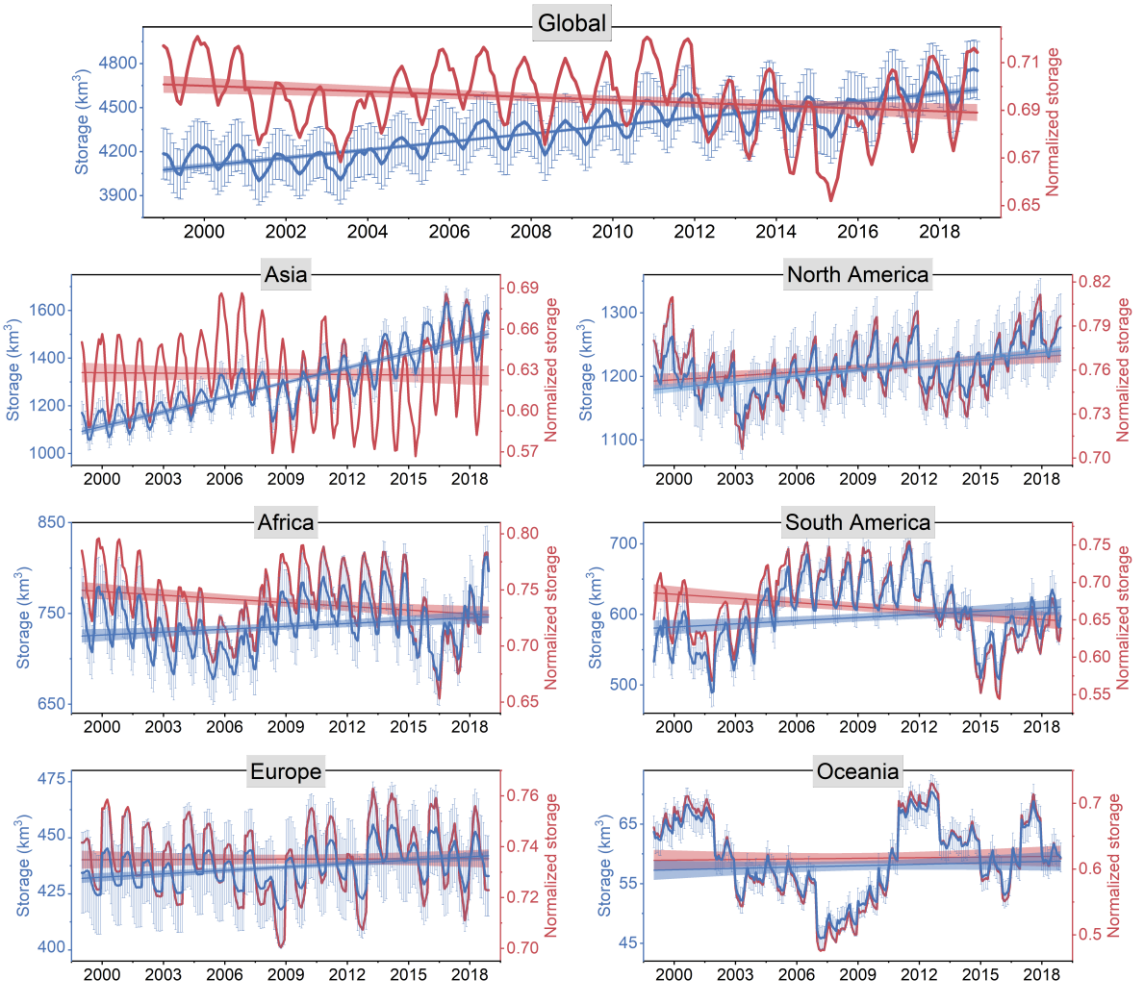

Figure 4.5 Monthly reservoir storage and normalized storage variations at the global and continental scales from 1999 to 2018. The error bars represent the storage uncertainty in terms of NRMSE (4.15%). Shading illustrates the 95% confidence intervals for the best-fit linear trends.

Table 4.4 Statistics of global and continental storage variations from 1999 to 2018

	Globe	Asia	North America	Africa	South America	Europe	Oceania
# reservoirs	7245	2352	2284	752	341	1265	251
Capacity (km^3)	6653.37	2382.57	1602.57	1037.02	935.92	598.88	96.41
Ave. capacity (km^3)	0.92	1.01	0.70	1.38	2.74	0.47	0.38
Mean storage (km^3)	4351.98 ± 181.35	1304.05 ± 140.11	1211.23 ± 34.38	737.96 ± 29.73	602.17 ± 44.93	437.24 ± 8.62	59.32 ± 6.07
Mean normalized storage	0.695 ± 0.014	0.627 ± 0.029	0.761 ± 0.020	0.739 ± 0.030	0.667 ± 0.047	0.735 ± 0.014	0.616 ± 0.063
Storage trend (km^3/yr)	27.44 ± 0.96 $p < 0.001$	20.53 ± 0.73 $p < 0.001$	3.07 ± 0.33 $p < 0.001$	1.06 ± 0.33 $p < 0.001$	1.50 ± 0.48 $p < 0.001$	0.51 ± 0.09 $p < 0.001$	0.077 ± 0.073 $p = 0.29$
Normalized storage trend (10^{-4}/yr)	-5.94 ± 1.57 $p < 0.001$	-1.11 ± 3.22 $p = 0.73$	8.84 ± 2.18 $p < 0.001$	-11.02 ± 3.31 $p < 0.001$	-18.72 ± 5.08 $p < 0.001$	0.23 ± 1.57 $p = 0.88$	3.11 ± 7.08 $p = 0.66$

All uncertainties are standard deviations. Ave. capacity represents the averaged storage capacity. Mean storage and normalized storage were derived from the monthly observations from 1999 to 2018.

The storage variations at the river basin scale are also evaluated (Figure 4.6). To reduce the uncertainties, only basins with more than five reservoirs were considered. Figure 4.6 shows the basins with significant trends ($p < 0.01$) of storage and normalized storage. According to Figure 4.6a, Asian basins have the most storage growth, while basins in southern Africa have suffered from storage losses. The highest increasing and decreasing rates are from the Yangtze (4.79 km^3/yr) and Colorado (-1.10 km^3/yr) river basins. Yangtze basin was reported to face the highest dam construction activity (e.g., Three Gorges Dam) in Asia (Zarfl et al. 2015). The rapid decrease in the Colorado basin can be explained by a historic, extended drought since 2000 (Udall and Overpeck 2017) and the increasing water use (Kuhn and Fleck 2019). According to Figure 4.6b, fewer basins in Asia show significant increases in normalized storage compared to that of storage, and the increasing rate is not very high. Moreover, it is observed that the majority of South America and Africa experienced decreasing normalized storages.

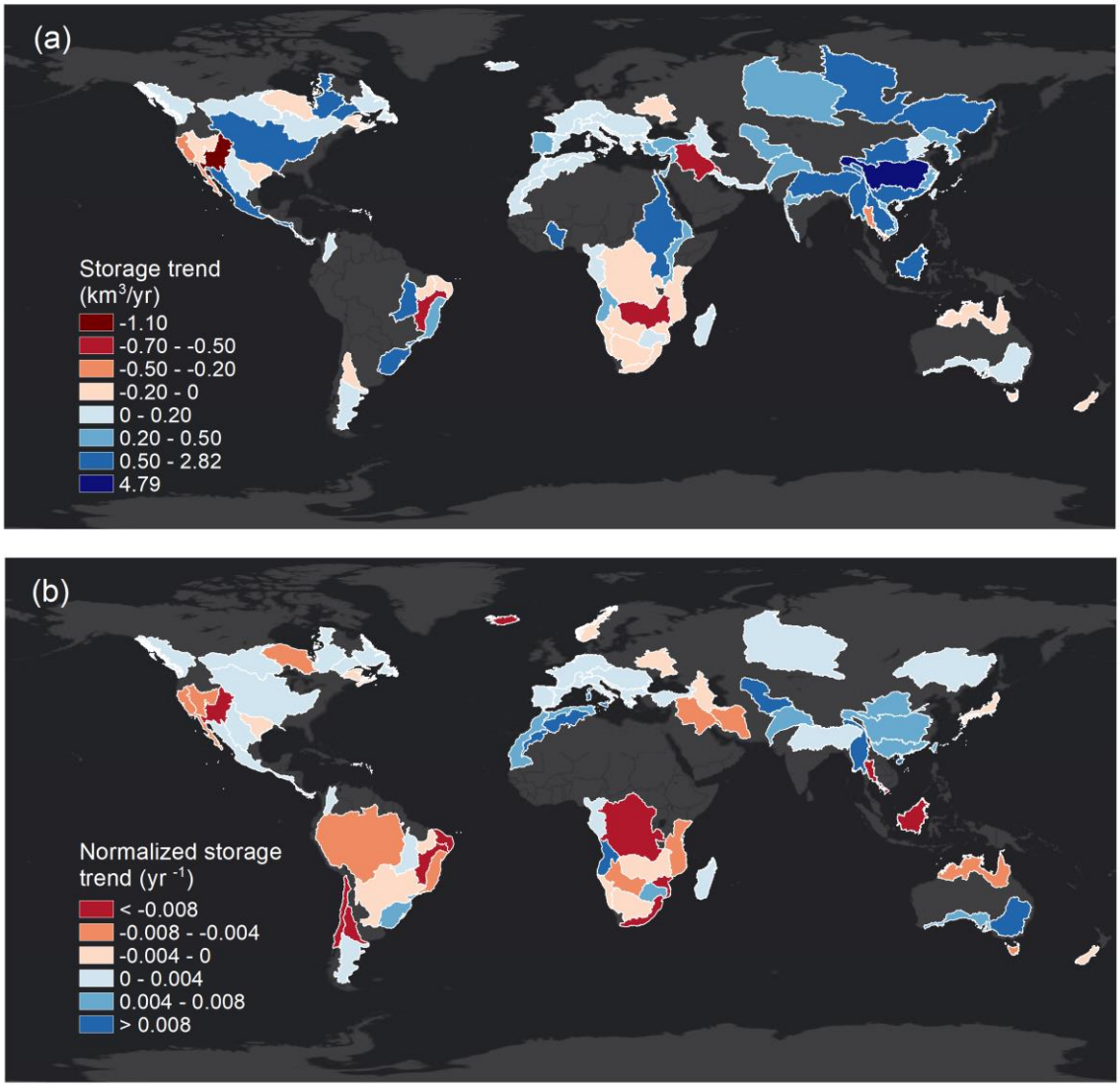

Figure 4.6 Significant treads ($p < 0.01$) of (a) storage and (b) normalized storage at the basin scale. To reduce uncertainty, only basins containing more than five reservoirs were considered.

4.3.3. Effects of newly constructed reservoirs in the 21st century

In this study, the effects of the reservoirs constructed after 1999 (hereafter referred to as "new reservoirs") were evaluated by comparison with those constructed before 1999 (hereafter referred to as "old reservoirs"). Figure 4.7 shows the storage and normalized storage time series for the old reservoirs at global and continental scales. At the global

scale, both the storage and normalized storage for the old reservoirs are relatively stable (i.e., without significant trends). This suggests that the increased storage and decreased normalized storage trends identified in Figure 4.5 are mainly attributed to the new reservoirs.

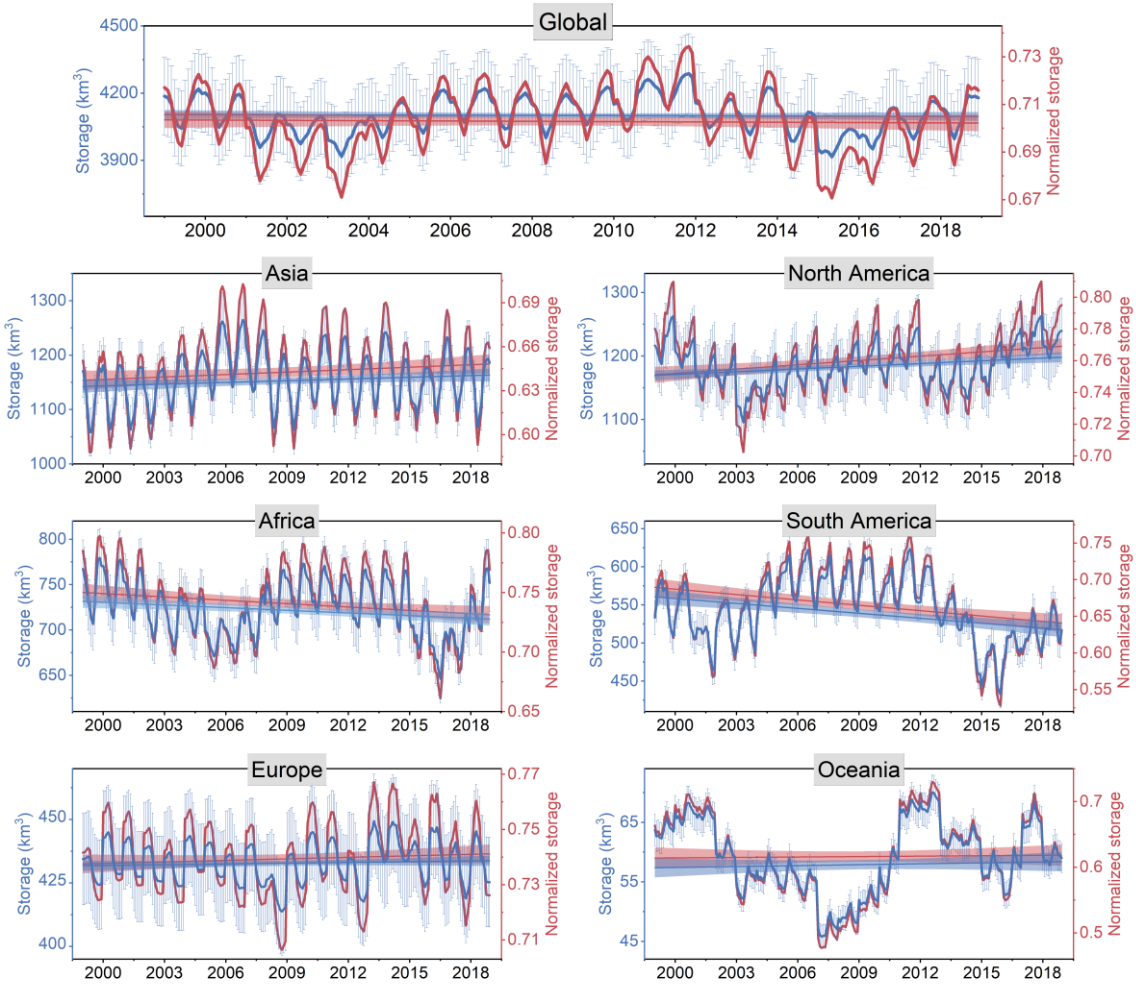

Figure 4.7 Monthly reservoir storage and normalized storage variations for old reservoirs at the global and continental scales from 1999 to 2018. The error bar represents the storage uncertainty in terms of NRMSE (4.15%). Shading illustrates 95% confidence intervals for the best-fit linear trends.

At the continental scale, by comparing the time series (Figure 4.5 vs Figure 4.7), Asia, Africa, and South America are found to be significantly influenced by new

reservoirs. Moreover, new reservoirs in these three continents account for the top three—71.44%, 14.29%, and 7.32%, respectively, in terms of storage capacity (Table 4.5).

Table 4.5 Statistics of old and new reservoirs at the global and continental scales

	Globe	Asia	North America	Africa	South America	Europe	Oceania
Reservoirs constructed before 1999							
# reservoirs	6737	1990	2261	715	282	1240	249
Capacity (km^3)	5837.66	1799.83	1559.39	977.34	819.34	585.75	96.00
Ave. capacity (km^3)	0.87	0.90	0.69	1.37	2.91	0.47	0.39
Mean storage (km^3)	4103.17 ± 79.58	1156.68 ± 47.04	1185.35 ± 32.01	723.90 ± 28.72	545.01 ± 41.31	433.07 ± 7.90	59.16 ± 6.03
Mean normalized storage	0.703 ± 0.014	0.643 ± 0.026	0.760 ± 0.021	0.741 ± 0.029	0.665 ± 0.050	0.739 ± 0.013	0.616 ± 0.063
Storage trend (km^3/yr)	-0.44 ± 0.89 $p = 0.62$	1.05 ± 0.52 $p < 0.05$	1.44 ± 0.35 $p < 0.001$	-0.98 ± 0.32 $p < 0.005$	-2.16 ± 0.44 $p < 0.001$	0.098 ± 0.089 $p = 0.27$	0.052 ± 0.072 $p = 0.47$
Normalized storage trend (10^{-4}/yr)	-0.66 ± 1.53 $p = 0.67$	5.56 ± 2.91 $p = 0.057$	9.02 ± 2.23 $p < 0.001$	-9.43 ± 3.24 $p < 0.005$	-24.41 ± 5.44 $p < 0.001$	1.83 ± 1.51 $p = 0.23$	2.18 ± 7.05 $p = 0.76$
Reservoirs constructed after 1999							
# reservoirs	508	362	23	37	59	25	2
Capacity (km^3)	815.71	582.74	43.18	59.68	116.58	13.13	0.41
Ave. capacity (km^3)	1.61	1.61	1.88	1.61	1.98	0.53	0.21

All uncertainties are standard deviations. Ave. capacity represents the averaged storage capacity. Mean storage and normalized storage were derived from the monthly observations from 1999 to 2018.

Figure 4.8 compares the monthly normalized storage values of new and old reservoirs, along with the accumulative storage capacity for new reservoirs. It should be noted that the new reservoirs in GRanD v1.3 were primarily constructed between 1999 and 2016. It is apparent that the normalized storage of new reservoirs is much lower (with larger seasonal variations) than that of old reservoirs. It is found that new reservoirs had a large variation of normalized storage from 1999 to 2003 because their accumulative capacity during that time was relatively small. Their normalized storage was relatively stable from 2004 and 2015, and it started to converge to that of the old reservoirs from 2016, which is mainly attributed to the storage increase in Asia. Although the annual peak normalized storage of new reservoirs approached that of the old reservoirs from 2016

onward, the new reservoirs still show larger seasonal variations than the old ones. The larger variations are also mainly attributed to the new reservoirs in Asia.

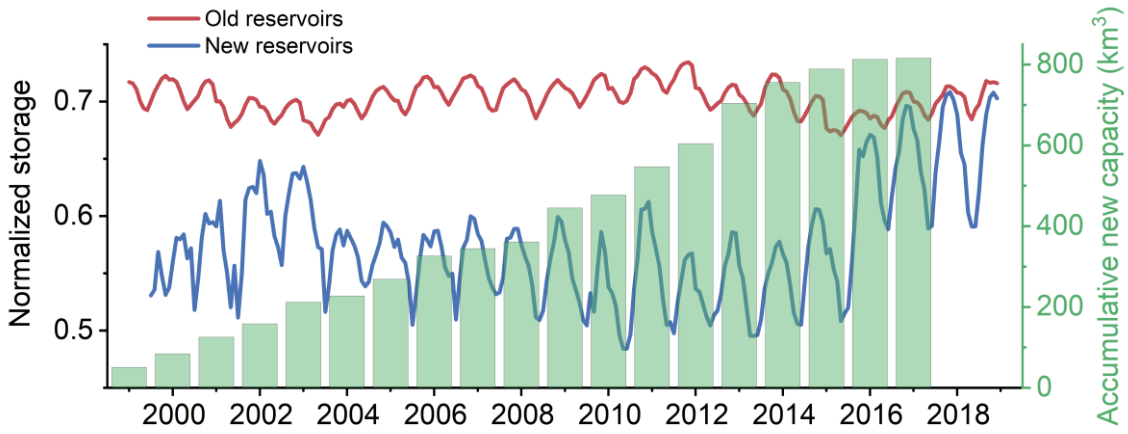

Figure 4.8 Comparison of the monthly normalized storage of new and old reservoirs, along with the accumulative storage capacity of new reservoirs.

In general, reservoirs with larger seasonal dynamics of normalized storages are under more pressure. The standard deviation of the normalized storages, which is based on the 12 monthly values in each year, can be used to evaluate the reservoir operation efficiency. Figure 4.9 compares the annual mean normalized storages and the corresponding standard deviations for all of the reservoirs with those for only the old reservoirs. It is found that global reservoir efficiency was affected by the construction of new reservoirs during the period from 1999 to 2018.

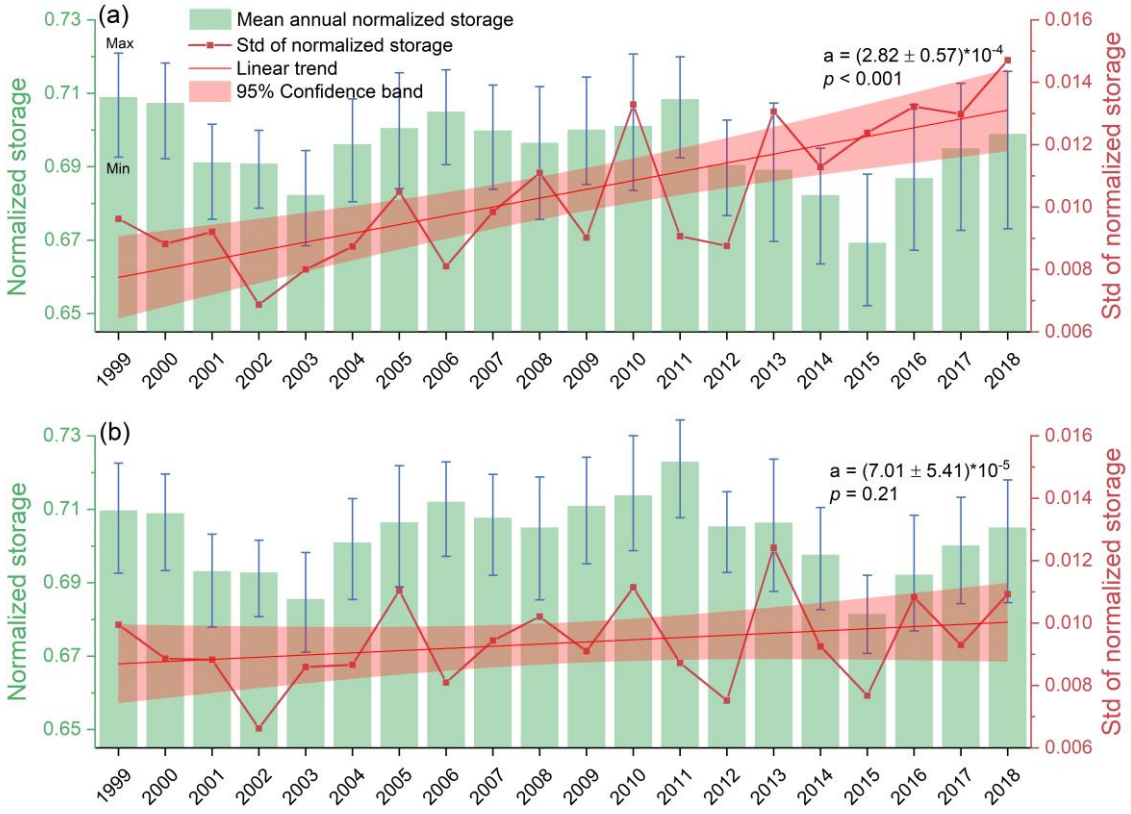

Figure 4.9 Mean annual normalized storage and the corresponding standard deviation for (a) all reservoirs, and (b) old reservoirs.

In addition, the effects of new reservoirs were evaluated at the continental scale. Europe and Oceania were not included because they had few new reservoirs, with relatively small capacity, and the trends of normalized storage were not significant. New reservoirs have the largest impacts on Asia. For the old reservoirs, the trend shows a significant increase as the p-value is 0.057 (very close to 0.05). However, the new reservoirs changed the direction of the trend to decreasing (though it is not significant, $p = 0.73$). While for North America, Africa, and South America, the trends of the normalized storage—both with and without the new reservoirs—are consistent. Therefore, hypothesis

tests were conducted to evaluate the trends by comparing the slopes and constant coefficients.

First, we need to determine whether the trends of normalized storage depend on the condition of new reservoir construction. To perform a hypothesis test on the difference between regression coefficients, an interaction term needs to be included into the model. In this case, an interaction term for Time*Condition was included. Condition A represents all reservoirs, while condition B represents the old reservoirs only. Then, the regression model was fit with Time (a continuous independent variable), Condition (the main effect), and Time*Condition (the interaction effect). The results of this model are shown in Table S1a in Appendix B. The p-value for Time is 0.000, which indicates that the relationship between Time and Normalized storage is statistically significant (i.e., the trend of normalized storage is significant). The Condition term tests for the difference between the constants, and is an indicator of the main effect. The coefficient of this term indicates that the difference between the constants is -0.00135, with a p-value of 0.707. This indicates that we cannot conclude that the constants are different. The coefficient of the interaction term (Time*Condition) is 0.000018, which represents the difference between the coefficients of the slopes for Condition A and Condition B. The corresponding p-value is 0.955, which indicates that this difference is not statistically significant (and we cannot reject the null hypothesis, i.e. that the difference is zero). In other words, it can be concluded that the Condition (i.e., the construction of new reservoirs) does not affect the relationship between the Time and Normalized storage. Therefore, the construction of new reservoirs in North America did not impact the trend of normalized storage. More details

about the hypothesis test used in this dissertation can be referred to at https://statisticsbyjim.com/regression/comparing-regression-lines/

Using the same approach, the hypothesis test results for Africa and South America are shown in Tables S1b and S1c in Appendix B. The conclusions for both of these continents are the same as that for North America. This suggests that the new reservoirs only impact the normalized storage of Asia, which contains more than 70% of new global reservoirs. Furthermore, the effects of new reservoirs on the global normalized storage are mainly attributed to Asia.

4.3.4. Connections between ENSO and reservoir storage variations

The El Nino Southern Oscillation (ENSO) is a recurring climate pattern that occurs at irregular intervals (2–7 years) in the central and eastern tropical Pacific Ocean. Previous studies have indicated that ENSO has a significant influence on terrestrial water storage (Ni et al. 2018; Phillips et al. 2012). In this study, the Multivariate ENSO Index Version 2 (MEI.v2) provided by NOAA (https://psl.noaa.gov/enso/mei/) was used to evaluate the effects of ENSO on the reservoir storage variations. MEI.v2 combines five different variables—sea level pressure (SLP), sea surface temperature (SST), zonal and meridional components of the surface wind, and outgoing longwave radiation (OLR)—over the tropical Pacific region (30°S–30°N and 100°E–70°W) to assess the ENSO intensity. Figure 4.10 compares the monthly MEI.v2 and normalized storage anomaly of global reservoirs from 1999 to 2018. Overall, MEI.v2 has a significantly negative correlation with the normalized storage anomalies ($R = 0.58$, $p < 0.001$). This relationship is even more significant during strong ENSO years ($R = 0.86$, $p < 0.001$).

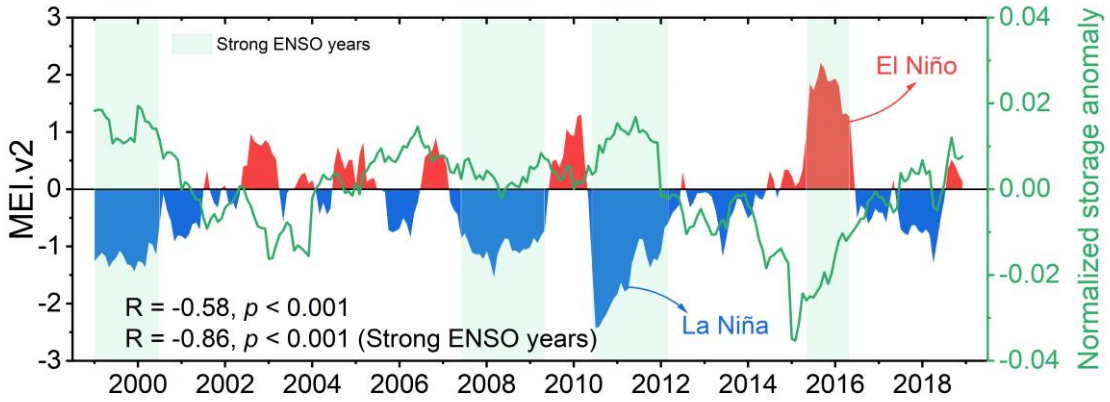

Figure 4.10 The link between the normalized storage anomaly of global reservoirs and Multivariate ENSO Index Version 2 (MEI.v2).

Moreover, the influence of ENSO on the normalized storage was also evaluated at the basin scale. Figure 4.11 shows basins with significant correlations ($p < 0.01$) between the normalized storage anomaly and MEI.v2 for strong ENSO years. To reduce the uncertainty, only basins containing more than five reservoirs were considered. It is obvious that most basins in the tropical areas have a strong negative correlation with MEI.v2. This is because tropical areas experience a large seasonal precipitation fluctuation, and the longitudinal precipitation center migrates with the ENSO phase (Walker Circulation) (Phillips et al. 2012). Basins with significantly negative correlations also prevail in South America and Africa. However, the correlations are generally positive in the high-latitude regions. It is worth noting that MEI.v2 shows a significant increase during the last two decades (Figure S2 in Appendix B). Therefore, it can be concluded that ENSO may be the main factor leading to the decrease of normalized storage in South America and Africa.

As shown in Figure 4.11, some coastal basins in North America are also susceptible to ENSO. In particular, there is a cluster of basins located along the Pacific

coast that are negatively correlated to MEI.v2 (while for most of the inland basins, the correlations are either positive or insignificant). The increase of the normalized storage in North America is mainly attributed to water storage growth that followed the region's recovery from a series of extreme droughts (Wang et al. 2013), especially in central North America (Figure 4.6). This water storage increase (in North America) was also reported by Wang et al. (2013) using Gravity Recovery and Climate Experiment (GRACE) observations.

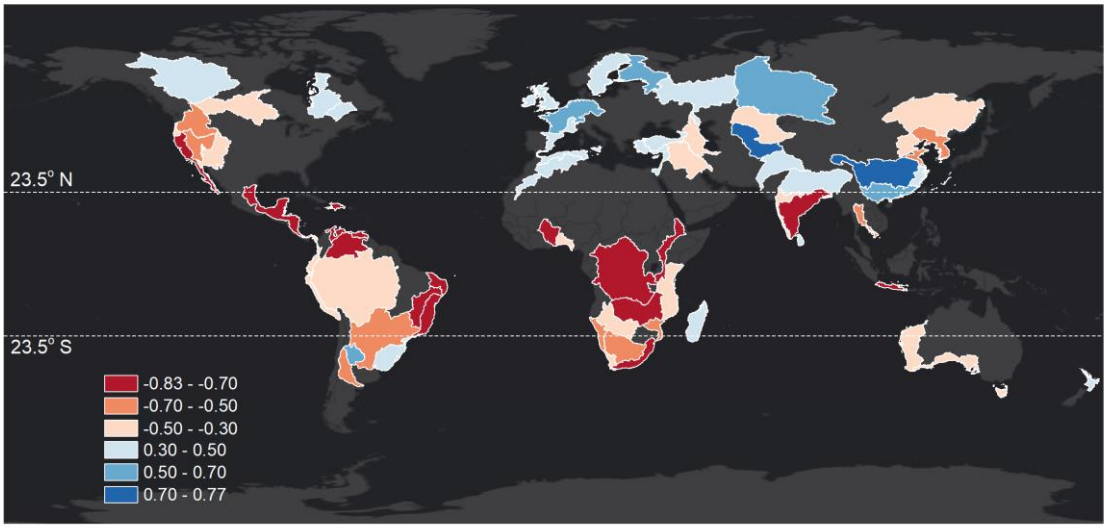

Figure 4.11 Basins with significant correlations ($p < 0.01$) between MEI.v2 and the normalized storage anomaly during strong ENSO years.

4.3.5. Reservoir storage variations under different functions

Reservoirs are designed to fulfill single- or multiple-functions, which are directly related to operation rules and storage. In this study, we selected four main functions (i.e., hydropower, irrigation, water supply, and flood control) to evaluate their normalized storage variations and responses to climate variability. The function information was collected from GRanD, and a 'main function' was selected for each reservoir. Figure 4.12

summarizes the distribution of these four functions for both old and new reservoirs (in terms of number and capacity). It is evident that reservoirs with hydropower purposes are predominant, followed by those focused on irrigation. With regard to the old reservoirs (Figure 4.12a), 32% (1516) of them are mainly used for hydropower, accounting for 70% (3797.42 km^3) of the total capacity. While for the new reservoirs (Figure 4.12b), the percentage devoted to hydropower in terms of number and capacity increased to 62% and 86%, respectively, indicating that the reservoirs constructed in the 21st century are primarily for hydropower purposes.

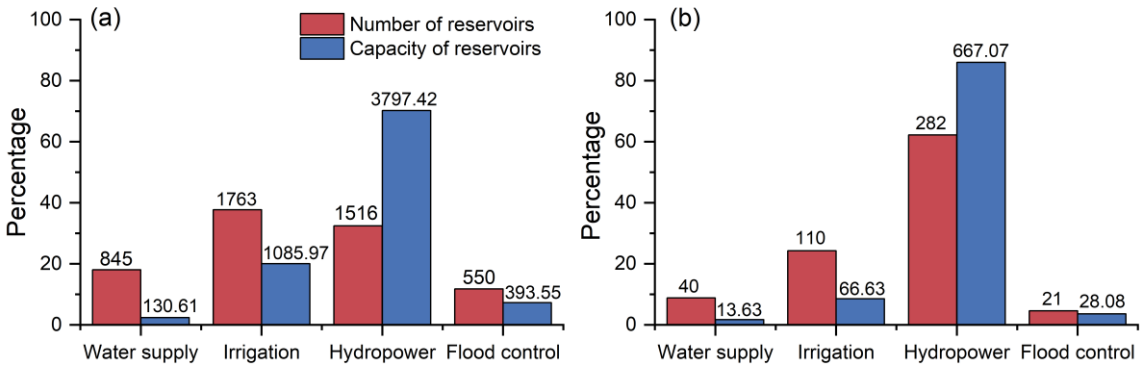

Figure 4.12 Summary of the main functions for global (a) old and (b) new reservoirs. The plots show the percentage of each function with regard to the total reservoir number or storage capacity. The corresponding absolute values of reservoir number and storage are labeled on the top of each column.

The normalized storages for global reservoirs with different functions are shown in Figure 4.13. Among all of the reservoirs, those with hydropower as the main purpose have the highest normalized storage levels (mean value of 0.74), but also have the smallest variation (standard deviation of 0.015). This is because hydropower reservoirs need to maintain relatively high water levels to ensure that the generator operates efficiently. It is worth noting that the normalized storage shows a significant decreasing trend ($p < 0.001$),

which is highly related to ENSO with a correlation value of -0.85 ($p < 0.001$). For instance, the normalized storage dipped in 2015, which was the strongest El Niño year in the 21st century. The reservoirs used for water supply have the smallest average storage capacity—0.16 km^3 (vs 2.49 km^3 for hydropower). However, the normalized storage for these reservoirs experienced the largest variation (with a standard deviation of 0.04, denoted by error bar in Figure 4.13b), along with a significant decrease ($p < 0.001$)—which suggests that they are suffering from increased pressure under the increasing municipal water demand. It is worth noting that the normalized storage has a sharp decrease in the first several years, followed by a slow decrease. The month of February 2002 was detected as the changing point using the Strucchange approach—which detects the structural changes in linear regression relationships (Zeileis et al. 2001). Therefore, we divided the period into two shorter ones: 1999–2001 and 2002–2018. The magnitude of decrease from 1999 to 2001 was 11 times larger than that from 2002 to 2018. While for reservoirs with flood control functions, the normalized storage values also show a rapid decrease from 1999 to 2001 (December 2001 was detected as the changing point). However, they bounced back with a significant increase from 2002 to 2018. The storage values of the irrigation reservoirs are relatively stable with no significant trends. They have shown uniform seasonal variations, which are consistent with crop phenology.

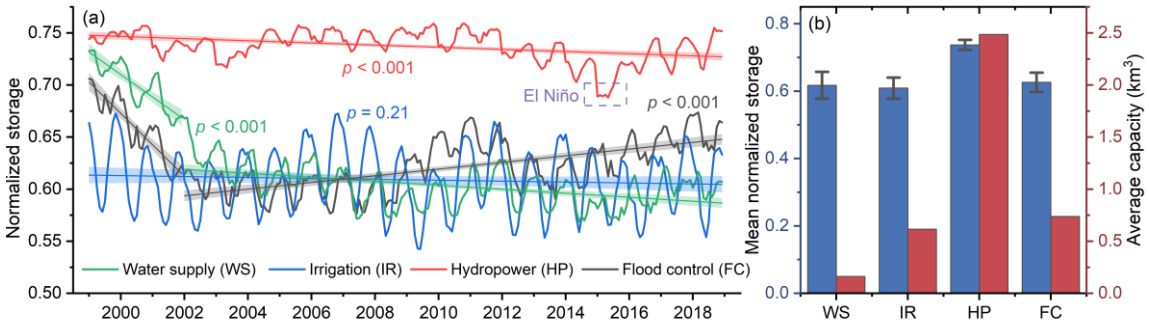

Figure 4.13 (a) Monthly normalized storage and linear trend (with the shaded areas representing the 95% confidence intervals) from 1999 to 2018 for global reservoirs with different functions. It should be noted that the time series of the water supply and flood control reservoirs was divided into two periods—1999–2001 and 2002–2018—using a change point approach. (b) Mean normalized storage by function (with error bars representing the standard deviations) from 1999 to 2018, along with the average capacity for each reservoir function.

4.4. Discussion and Conclusions

Despite the overall good accuracy of the storage dataset, uncertainties from two sources need to be discussed. The first is the uncertainty due to reservoir sedimentation, which can reduce the storage capacity. Reservoir sedimentation is affected by several major factors, such as geometry, streamflow, sediment load, particle size, deposit specific weight, reservoir size, and operation rules (Salas and Shin 1999; Schleiss et al. 2016; USBR 1987). It has been reported that the sedimentation rate varies with reservoir size, with larger reservoirs having smaller rates (Dendy et al. 1973; Rahmani et al. 2018; Wisser et al. 2013). Recently, Wisser et al. (2013) evaluated the storage capacity loss for global reservoirs in GRanD. It shows that the total storage capacity declined by 4.5% from 1990 to 2010, at an annual rate of 0.23%. Moreover, Dendy et al. (1973) estimated the average annual loss rates for different size categories using the sedimentation data for 1105 reservoirs. Based on this set of loss rates, we calculated the storage weighted annual

sedimentation rate for the 7245 reservoirs in our dataset to be 0.18%. These two small storage loss rates (i.e., 0.23% and 0.18%) indicate that the reservoir sedimentation does not have a significant influence on the evaluation of storage variations. Currently, a wide range of techniques (e.g., flushing and dredging) have been developed and implemented—from the planning phase to the design, build, and operation phases—to control sedimentation and ensure the long-term sustainability of reservoirs (Garcia 2008; Kondolf et al. 2014; Morris 2014; Schleiss et al. 2016). It should be noted that a fraction of the reservoirs in our dataset (e.g., some in the U.S. and India) were evaluated in terms of live storage, which is more resistant to sedimentation. Therefore, we did not consider the effects of reservoir sedimentation on storage estimation in this study.

The second source is related to the modified simulation method of Yigzaw et al. (2018). The performance of the mathematical approximations is not ideal sometimes because the reservoir geometry is very complicated. For example, the NRMSE values of storage estimations for Rana Pratap Sagar and Yeleru are 127.73% and 87.14%, respectively (Table 4.3). However, they have good consistency with the *in situ* observations, with respective R^2 values of 0.80 and 0.89, indicating that they can successfully capture the pattern of storage variations. Therefore, the effect of this relatively large bias should not be significant because the analyses are focused on evaluating the trend of storage variations across large scales.

ENSO is the largest driver of interannual water exchanges between land and ocean (Chandanpurkar et al. 2019). In general, El Niño is associated with a decrease in global terrestrial precipitation (Dai and Wigley 2000) and terrestrial water storage (Phillips et al.

2012), and the decrease is especially strong for tropical areas. This is consistent with the correlation between ENSO and reservoir storage. With the improved capability of ENSO forecasting (Ham et al. 2019), the reservoir storage values can then be projected, which will provide valuable information for water management.

The storage variations show different patterns according to reservoir function. The reservoirs with hydropower as the primary function account for 72.21% of global total storage, followed by those focused on irrigation (18.64%). Therefore, the storage variations of hydropower and irrigation reservoirs are highly correlated with MEI, with correlation values of -0.85 and -0.56, respectively. This is consistent with the significant negative correlation between global reservoir storage and MEI (Figure 4.10). With regard to water supply and flood control reservoirs, their correlations with MEI are not very strong. It is worth noting that their storage values show a rapid decrease starting in 1999, which is mainly attributed to severe droughts in North America. For reservoirs with primary functions of water supply and flood control, those in North America account for 53.93% and 56.39% in terms of storage. Since late 1999, the western U.S. has been suffering from a severe drought, which reached its peak in July 2002 when more than half of the contiguous U.S. was under moderate to severe drought conditions (Cook et al. 2007; Lawrimore and Stephens 2003; Svoboda et al. 2002). This severe drought also extended to large portions of the Canadian Prairie provinces and to the northern and western parts of Mexico (Hanesiak et al. 2011; Lawrimore et al. 2002). The water storage recovery from these extreme droughts (Wang et al. 2013), and the increased flood frequency and duration after the 2000s (Najibi and Devineni 2018), can explain the significant storage increase of

flood control reservoirs from 2002 to 2018. However, water supply reservoirs continue shrinking due to the steadily increasing water demand, although the rate is slower after 2002.

The storage dataset resulting from this study can benefit multiple applications. First, it provides critical information for management purposes, especially for reservoirs in transboundary river basins where gauge observations are not shared. Moreover, it can help to calibrate and validate the operation rules in the global hydrological models which have a reservoir module component, and can improve our understanding about the roles of reservoir storage in the hydrological cycle. Additionally, a drought index based on reservoir storage can be developed to evaluate hydrological droughts. Lastly, we can compare the reservoir storage values with GRACE observations to assess groundwater variations more accurately.

In the future, ICESat-2 (launched in September 2018) and the Surface Water and Ocean Topography (SWOT) mission (planned for launch in 2022) will provide more data for bathymetry mapping (Li et al. 2020), which will improve the estimates of reservoir storage. Moreover, the satellite observations with high temporal resolution (e.g., MODIS and VIIRS) can be used to achieve near real-time (daily) monitoring.

To conclude, the findings are summarized as follows:

(1) The estimated storage values agree well with *in situ* observations. Overall, the storage estimations using the A-V relationships derived from bathymetry data are more accurate than those from the simulation method.

(2) Global reservoir storage has an overall increasing trend at a rate of 27.44 ± 0.96 km^3/yr, which is mainly attributed to the construction of new dams. On the other hand, the normalized storage shows a significant decrease because of the effects of new reservoirs.

(3) The storage growth is primarily contributed to by Asia (20.53 ± 0.73 km^3/yr), which accounts for about 75% of the global increase. However, the addition of new reservoirs did not affect the normalized storages for other continents (where new reservoirs have a relatively small capacity). The increase of the normalized storage in North America is due to the water storage growth that occurred after recovery from a series of severe droughts, while the decrease in South America and Africa is highly correlated to ENSO.

(4) The reservoirs with hydropower purposes have a relatively high storage level, and they are more sensitive to ENSO. Water supply reservoirs are experiencing a significant storage decrease, indicating the growing water crisis brought on by the steadily increasing municipal water demand.

5. CONCLUSIONS

Despite the importance of reservoirs to human society, our knowledge of reservoirs is still limited at the global scale. With the advancement of satellite remote sensing, monitoring reservoirs from the space is becoming increasingly practical. Knowledge of reservoir bathymetry is essential for many studies on terrestrial hydrological and biogeochemical processes. However, there are currently no cost-effective approaches to derive reservoir bathymetry at the global scale. Moreover, water retained by global reservoirs has long term impacts on global and regional water cycles. Therefore, this dissertation fills in a knowledge gap with regard to remotely sensed high-resolution bathymetry and long-term storage datasets for global reservoirs.

Through the first study (Chapter 2), an algorithm was developed to generate reservoir bathymetries exclusively from lidar altimetry and satellite imagery data. By combining elevations collected by the airborne ICESat-2 prototype with water areas from long-term Landsat observations, a high-resolution 3D reservoir bathymetry map was derived for Lake Mead, representing the dynamic area over the last three decades. The bathymetry for the central reservoir area can be projected by extrapolation, and then integrated with the remotely sensed results to obtain the full bathymetry. Validations against lidar survey data from four transacts of remotely sensed bathymetry show R^2 values from 0.82 to 0.99 and RMSE values from 1.18 m to 2.36 m. The predicted portions have relatively large errors and uncertainties (compared to the remotely sensed portions) because the extrapolated elevations cannot fully capture the underwater topography.

Built upon the bathymetry generation algorithm, the second study (Chapter 3) extended the domain to global reservoirs. We utilized multiple satellite altimetry datasets (ICESat, G-REALM, and Hydroweb) in combination with Landsat-based surface water datasets to develop the first consistent high-resolution 3-D bathymetry dataset for global reservoirs. This dataset includes 347 reservoirs with a total capacity of 3123 km^3, representing 50% of the global reservoir capacity. Validation against the surveyed bathymetry over four reservoirs indicates a relatively high accuracy and reliability of the remotely sensed bathymetry, with R^2 values ranging from 0.82 to 0.99 and RMSE values from 0.19 m to 1.65 m. An indirect validation—which compared the remotely sensed A-E and E-V relationships with those derived from in situ data for 16 reservoirs—also suggests good agreement. These relationships could be used to monitor the storage variations of global reservoirs, either from satellite altimetry or imagery data. In addition to reservoirs, the bathymetry values for hundreds of global natural lakes could also be obtained using this method.

In Chapter 4, a long-term storage dataset was developed by leveraging multi-satellite observations for a total of 7245 global reservoirs. For each reservoir, the A-V relationship was either derived from the 3-D bathymetry using a remote sensing method or estimated through an improved simulation method. In general, the storage estimated from the bathymetry had a better performance compared to the storage estimated from the simulation method. Based on this dataset, the reservoir storage variations were assessed at global, continental, and basin scales. The results suggest that the global reservoir storage has an overall increasing trend at a rate of 27.44 ± 0.96 km^3/yr, which is mainly attributed

to the construction of new dams. On the other hand, the normalized storage shows a significant decrease because of the effects of new reservoirs. The storage growth is primarily contributed to by Asia (20.53 ± 0.73 km^3/yr), which accounts for about 75% of the global increase. It was also found that the increase of the normalized storage in North America is due to the water storage growth resulting from the recovery of several severe droughts, while the decrease in South America and Africa is highly correlated to ENSO. Moreover, the reservoirs with hydropower purposes have a relatively high normalized storage, and they are more sensitive to ENSO. The reservoirs focused on water supply are experiencing a significant decrease in their normalized storage, which corresponds to the growing water crisis under the steadily increasing municipal water demand.

REFERENCES

Abshire, J.B., Sun, X., Riris, H., Sirota, J.M., McGarry, J.F., Palm, S., Yi, D., & Liiva, P. (2005). Geoscience laser altimeter system (GLAS) on the ICESat mission: on ‐ orbit measurement performance. *Geophysical Research Letters, 32*

Alex Elliott, J., Thackeray, S.J., Huntingford, C., & Jones, R.G. (2005). Combining a regional climate model with a phytoplankton community model to predict future changes in phytoplankton in lakes. *Freshwater Biology, 50*, 1404-1411

Amante, C. (2009). ETOPO1 1 arc-minute global relief model: procedures, data sources and analysis. *http://www.ngdc.noaa.gov/mgg/global/global.html*

Arsen, A., Crétaux, J.-F., Berge-Nguyen, M., & del Rio, R.A. (2013). Remote sensing-derived bathymetry of Lake Poopó. *Remote Sensing, 6*, 407-420

Arvidson, T., Gasch, J., & Goward, S.N. (2001). Landsat 7's long-term acquisition plan—An innovative approach to building a global imagery archive. *Remote Sensing of Environment, 78*, 13-26

Bai, X., Wang, J., Schwab, D.J., Yang, Y., Luo, L., Leshkevich, G.A., & Liu, S. (2013). Modeling 1993–2008 climatology of seasonal general circulation and thermal structure in the Great Lakes using FVCOM. *Ocean Modelling, 65*, 40-63

Bailey, J.E., Self, S., Wooller, L.K., & Mouginis-Mark, P.J. (2007). Discrimination of fluvial and eolian features on large ignimbrite sheets around La Pacana Caldera, Chile, using Landsat and SRTM-derived DEM. *Remote Sensing of Environment, 108*, 24-41

Balsamo, G., Salgado, R., Dutra, E., Boussetta, S., Stockdale, T., & Potes, M. (2012). On the contribution of lakes in predicting near-surface temperature in a global weather forecasting model. *Tellus A: Dynamic Meteorology and Oceanography, 64*, 15829

Beletsky, D., Schwab, D., & McCormick, M. (2006). Modeling the 1998–2003 summer circulation and thermal structure in Lake Michigan. *Journal of Geophysical Research: Oceans, 111*

Biancamaria, S., Lettenmaier, D.P., & Pavelsky, T.M. (2016). The SWOT mission and its capabilities for land hydrology. *Remote Sensing and Water Resources* (pp. 117-147): Springer

Biemans, H., Haddeland, I., Kabat, P., Ludwig, F., Hutjes, R., Heinke, J., Von Bloh, W., & Gerten, D. (2011). Impact of reservoirs on river discharge and irrigation water supply during the 20th century. *Water Resources Research, 47*

Bierkens, M.F., Bell, V.A., Burek, P., Chaney, N., Condon, L.E., David, C.H., de Roo, A., Döll, P., Drost, N., & Famiglietti, J.S. (2015). Hyper-resolution global hydrological modelling: What is next? Everywhere and locally relevant. *Hydrological Processes, 29*, 310-320

Birkett, C. (1994). Radar altimetry: a new concept in monitoring lake level changes. *Eos, Transactions American Geophysical Union, 75*, 273-275

Birkett, C. (1995). The contribution of TOPEX/POSEIDON to the global monitoring of climatically sensitive lakes. *Journal of Geophysical Research: Oceans, 100*, 25179-25204

Birkett, C., Reynolds, C., Beckley, B., & Doorn, B. (2011). From research to operations: the USDA global reservoir and lake monitor. In *Coastal altimetry* (pp. 19-50): Springer

Brando, V.E., Anstee, J.M., Wettle, M., Dekker, A.G., Phinn, S.R., & Roelfsema, C. (2009). A physics based retrieval and quality assessment of bathymetry from suboptimal hyperspectral data. *Remote Sensing of Environment, 113*, 755-770

Brenner, A.C., DiMarzio, J.P., & Zwally, H.J. (2007). Precision and accuracy of satellite radar and laser altimeter data over the continental ice sheets. *IEEE Transactions on Geoscience and Remote Sensing, 45*, 321-331

Britton-Simmons, K.H., Rhoades, A.L., Pacunski, R.E., Galloway, A.W., Lowe, A.T., Sosik, E.A., Dethier, M.N., & Duggins, D.O. (2012). Habitat and bathymetry influence the landscape ‐ scale distribution and abundance of drift macrophytes and associated invertebrates. *Limnology and Oceanography, 57*, 176-184

Busker, T., de Roo, A., Gelati, E., Schwatke, C., Adamovic, M., Bisselink, B., Pekel, J.F., & Cottam, A. (2019). A global lake and reservoir volume analysis using a surface water dataset and satellite altimetry. *Hydrology and Earth System Sciences, 23*, 669-690

Chandanpurkar, H.A., Fasullo, J.T., Reager, J.T., Nerem, R.S., & Famiglietti, J.S. (2019). Asymmetric Response of Land Storage to ENSO Phase and Duration. *Water, 11*, 2249

Chao, B.F., Wu, Y., & Li, Y. (2008). Impact of artificial reservoir water impoundment on global sea level. *Science, 320*, 212-214

Cheng, C.T., Wang, W.C., Xu, D.M., & Chau, K.W. (2008). Optimizing hydropower reservoir operation using hybrid genetic algorithm and chaos. *Water Resources Management, 22*, 895-909

Cook, C., & Bakker, K. (2012). Water security: Debating an emerging paradigm. *Global Environmental Change, 22*, 94-102

Cook, E.R., Seager, R., Cane, M.A., & Stahle, D.W. (2007). North American drought: Reconstructions, causes, and consequences. *Earth-Science Reviews, 81,* 93-134

Cooke, G.D., Welch, E.B., Peterson, S., & Nichols, S.A. (2016). Restoration and management of lakes and reservoirs. CRC press

Crétaux, J.-F., Abarca-del-Río, R., Berge-Nguyen, M., Arsen, A., Drolon, V., Clos, G., & Maisongrande, P. (2016). Lake volume monitoring from space. *Surveys in Geophysics, 37,* 269-305

Crétaux, J.-F., Jelinski, W., Calmant, S., Kouraev, A., Vuglinski, V., Bergé-Nguyen, M., Gennero, M.-C., Nino, F., Del Rio, R.A., & Cazenave, A. (2011). SOLS: A lake database to monitor in the Near Real Time water level and storage variations from remote sensing data. *Advances in Space Research, 47*, 1497-1507

Dai, A., & Wigley, T. (2000). Global patterns of ENSO ‐ induced precipitation. *Geophysical Research Letters, 27,* 1283-1286

Dendy, F., Champion, W., & Wilson, R. (1973). Reservoir sedimentation surveys in the United States. *Washington DC American Geophysical Union Geophysical Monograph Series, 17*, 349-357

Döll, P., Fiedler, K., & Zhang, J. (2009). Global-scale analysis of river flow alterations due to water withdrawals and reservoirs. *Hydrology and Earth System Sciences, 13*, 2413

Donchyts, G., Baart, F., Winsemius, H., Gorelick, N., Kwadijk, J., & Van De Giesen, N. (2016). Earth's surface water change over the past 30 years. *Nature Climate Change, 6,* 810

Downing, J.A. (2010). Emerging global role of small lakes and ponds: little things mean a lot. *Limnetica, 29*, 0009-0024

Downing, J.A., Prairie, Y., Cole, J., Duarte, C., Tranvik, L., Striegl, R.G., McDowell, W., Kortelainen, P., Caraco, N., & Melack, J. (2006). The global abundance and size distribution of lakes, ponds, and impoundments. *Limnology and Oceanography, 51*, 2388-2397

Duan, Z., & Bastiaanssen, W. (2013). Estimating water volume variations in lakes and reservoirs from four operational satellite altimetry databases and satellite imagery data. *Remote Sensing of Environment, 134*, 403-416

Dunbar, J.A., Allen, P.M., & Higley, P.D. (1999). Multifrequency acoustic profiling for water reservoir sedimentation studies. *Journal of Sedimentary Research, 69*, 518-527

Dutra, E., Balsamo, G., Viterbo, P., Miranda, P.M., Beljaars, A., Schär, C., & Elder, K. (2010). An improved snow scheme for the ECMWF land surface model: Description and offline validation. *Journal of Hydrometeorology, 11*, 899-916

Falkowski, P., Scholes, R., Boyle, E., Canadell, J., Canfield, D., Elser, J., Gruber, N., Hibbard, K., Högberg, P., & Linder, S. (2000). The global carbon cycle: a test of our knowledge of earth as a system. *Science, 290*, 291-296

Farr, T.G., Rosen, P.A., Caro, E., Crippen, R., Duren, R., Hensley, S., Kobrick, M., Paller, M., Rodriguez, E., & Roth, L. (2007). The shuttle radar topography mission. *Reviews of Geophysics, 45*

Fu, G. (2008). A fuzzy optimization method for multicriteria decision making: An application to reservoir flood control operation. *Expert Systems with Applications, 34*, 145-149

Gao, H. (2015). Satellite remote sensing of large lakes and reservoirs: From elevation and area to storage. *Wiley Interdisciplinary Reviews: Water, 2*, 147-157

Gao, H., Birkett, C., & Lettenmaier, D.P. (2012). Global monitoring of large reservoir storage from satellite remote sensing. *Water Resources Research, 48*

Gao, H., Zhang, S., Durand, M., & Lee, H. (2016). Satellite remote sensing of lakes and wetlands. *Hydrologic Remote Sensing; CRC Press: Boca Raton, FL, USA*, 57-72

Gao, J. (2009). Bathymetric mapping by means of remote sensing: methods, accuracy and limitations. *Progress in Physical Geography, 33*, 103-116

Garcia, M. (2008). Sedimentation engineering: processes, measurements, modeling, and practice. In: American Society of Civil Engineers

Getirana, A., Jung, H.C., & Tseng, K.-H. (2018). Deriving three dimensional reservoir bathymetry from multi-satellite datasets. *Remote Sensing of Environment, 217*, 366-374

Grigg, N.S. (1996). Water resources management: principles, regulations, and cases. McGraw-Hill New York

Haddeland, I., Skaugen, T., & Lettenmaier, D.P. (2006). Anthropogenic impacts on continental surface water fluxes. *Geophysical Research Letters, 33*

Ham, Y.-G., Kim, J.-H., & Luo, J.-J. (2019). Deep learning for multi-year ENSO forecasts. *Nature, 573*, 568-572

Hanasaki, N., Kanae, S., & Oki, T. (2006). A reservoir operation scheme for global river routing models. *Journal of Hydrology, 327*, 22-41

Hanesiak, J., Stewart, R., Bonsal, B., Harder, P., Lawford, R., Aider, R., Amiro, B., Atallah, E., Barr, A., & Black, T. (2011). Characterization and summary of the 1999–2005 Canadian Prairie drought. *Atmosphere-Ocean, 49,* 421-452

Heathcote, A.J., del Giorgio, P.A., & Prairie, Y.T. (2015). Predicting bathymetric features of lakes from the topography of their surrounding landscape. *Canadian Journal of Fisheries and Aquatic Sciences, 72,* 643-650

Hell, B., Broman, B., Jakobsson, L., Jakobsson, M., Magnusson, Å., & Wiberg, P. (2012). The Use of Bathymetric Data in Society and Science: A Review from the Baltic Sea. *Ambio, 41*, 138-150

Hilldale, R.C., & Raff, D. (2008). Assessing the ability of airborne LiDAR to map river bathymetry. *Earth Surface Processes and Landforms, 33*, 773-783

Irish, J.L., & Lillycrop, W.J. (1999). Scanning laser mapping of the coastal zone: the SHOALS system. *ISPRS Journal of Photogrammetry and Remote Sensing, 54*, 123-129

Jasinski, M.F., Stoll, J.D., Cook, W.B., Ondrusek, M., Stengel, E., & Brunt, K. (2016). Inland and Near-Shore Water Profiles Derived from the High-Altitude Multiple Altimeter Beam Experimental Lidar (MABEL). *Journal of Coastal Research, 76*, 44-55

Khandelwal, A., Karpatne, A., Marlier, M.E., Kim, J., Lettenmaier, D.P., & Kumar, V. (2017). An approach for global monitoring of surface water extent variations in reservoirs using MODIS data. *Remote Sensing of Environment, 202*, 113-128

Kondolf, G.M., Gao, Y., Annandale, G.W., Morris, G.L., Jiang, E., Zhang, J., Cao, Y., Carling, P., Fu, K., & Guo, Q. (2014). Sustainable sediment management in reservoirs and regulated rivers: Experiences from five continents. *Earth's future, 2*, 256-280

Kourzeneva, E., Asensio, H., Martin, E., & Faroux, S. (2012). Global gridded dataset of lake coverage and lake depth for use in numerical weather prediction and climate modelling. *Tellus A: Dynamic Meteorology and Oceanography, 64*, 15640

Krieger, G., Moreira, A., Fiedler, H., Hajnsek, I., Werner, M., Younis, M., & Zink, M. (2007). TanDEM-X: A satellite formation for high-resolution SAR interferometry. *IEEE Transactions on Geoscience and Remote Sensing, 45*, 3317-3341

Kuhn, E., & Fleck, J. (2019). Science Be Dammed: How Ignoring Inconvenient Science Drained the Colorado River. University of Arizona Press

Lafon, V., Froidefond, J.M., Lahet, F., & Castaing, P. (2002). SPOT shallow water bathymetry of a moderately turbid tidal inlet based on field measurements. *Remote Sensing of Environment, 81*, 136-148

Lakewatch, F. (2001). A Beginner's Guide to Water Management: Lake Morphometry. University of Florida Cooperative Extension Service, Institute of Food and Agricultural Sciences, EDIS

Langland, M.J. (2009). Bathymetry and sediment-storage capacity change in three reservoirs on the Lower Susquehanna River, 1996-2008. In: US Geological Survey

Lawrimore, J., Heim Jr, R.R., Svoboda, M., Swail, V., & Englehart, P.J. (2002). Beginning a new era of drought monitoring across North America. *Bulletin of the American Meteorological Society, 83*, 1191-1192

Lawrimore, J., & Stephens, S. (2003). Climate of 2002 annual review. *NOAA National Climatic Data Center*

Lehmann, A. (1998). GIS modeling of submerged macrophyte distribution using Generalized Additive Models. *Plant Ecology, 139*, 113-124

Lehner, B., & Döll, P. (2004). Development and validation of a global database of lakes, reservoirs and wetlands. *Journal of Hydrology, 296*, 1-22

Lehner, B., Reidy Liermann, C., Revenga, C., Vorosmarty, C., Fekete, B., Crouzet, P., Doll, P., Endejan, M., Frenken, K., Magome, J., Nilsson, C., Robertson, J.C., Rodel, R., Sindorf, N., & Wisser, D. (2011a). Global Reservoir and Dam Database, Version 1 (GRanDv1): Dams, Revision 01. In. Palisades, NY: NASA Socioeconomic Data and Applications Center (SEDAC)

Lehner, B., Reidy Liermann, C., Revenga, C., Vorosmarty, C., Fekete, B., Crouzet, P., Doll, P., Endejan, M., Frenken, K., Magome, J., Nilsson, C., Robertson, J.C., Rodel, R., Sindorf, N., & Wisser, D. (2011b). High-Resolution Mapping of the World's Reservoirs and Dams for Sustainable River-Flow Management. *Frontiers in Ecology and the Environment, 9*, 494-502

Lettenmaier, D.P., & Milly, P. (2009). Land waters and sea level. *Nature Geoscience, 2*, 452

Li, J., & Sheng, Y. (2012). An automated scheme for glacial lake dynamics mapping using Landsat imagery and digital elevation models: A case study in the Himalayas. *International Journal of Remote Sensing, 33*, 5194-5213

Li, X., Long, D., Huang, Q., Han, P., Zhao, F., & Wada, Y. (2019a). High-temporal-resolution water level and storage change data sets for lakes on the Tibetan Plateau during 2000–2017 using multiple altimetric missions and Landsat-derived lake shoreline positions. *Earth System Science Data, 11*, 1603-1627

Li, X.A., Guo, S.L., Liu, P., & Chen, G.Y. (2010). Dynamic control of flood limited water level for reservoir operation by considering inflow uncertainty. *Journal of Hydrology, 391*, 126-134

Li, Y., Gao, H., Jasinski, M.F., Zhang, S., & Stoll, J.D. (2017). Comparing Storage Estimations for Lake Mead using multi-source satellite altimetry and imagery data. *AGU Fall Abstract*

Li, Y., Gao, H., Jasinski, M.F., Zhang, S., & Stoll, J.D. (2019b). Deriving High-Resolution Reservoir Bathymetry From ICESat-2 Prototype Photon-Counting Lidar and Landsat Imagery. *IEEE Transactions on Geoscience and Remote Sensing, 57*, 7883-7893

Li, Y., Gao, H., Zhao, G., & Tseng, K.-H. (2020). A high-resolution bathymetry dataset for global reservoirs using multi-source satellite imagery and altimetry. *Remote Sensing of Environment, 244*, 111831

Lindim, C., Pinho, J.L., & Vieira, J.M.P. (2011). Analysis of spatial and temporal patterns in a large reservoir using water quality and hydrodynamic modeling. *Ecological Modelling, 222*, 2485-2494

Markus, T., Neumann, T., Martino, A., Abdalati, W., Brunt, K., Csatho, B., Farrell, S., Fricker, H., Gardner, A., Harding, D., Jasinski, M., Kwok, R., Magruder, L., Lubin, D., Luthcke, S., Morison, J., Nelson, R., Neuenschwander, A., Palm, S., Popescu, S., Shum,

C.K., Schutz, B.E., Smith, B., Yang, Y., & Zwally, J. (2017). The Ice, Cloud, and land Elevation Satellite-2 (ICESat-2): Science requirements, concept, and implementation. *Remote Sensing of Environment, 190*, 260-273

McFeeters, S.K. (1996). The use of the Normalized Difference Water Index (NDWI) in the delineation of open water features. *International Journal of Remote Sensing, 17*, 1425-1432

Melesse, A.M., & Jordan, J.D. (2002). A comparison of fuzzy vs. augmented-ISODATA classification algorithms for cloud-shadow discrimination from landsat images. *Photogrammetric Engineering and Remote Sensing, 68*, 905-911

Messager, M.L., Lehner, B., Grill, G., Nedeva, I., & Schmitt, O. (2016). Estimating the volume and age of water stored in global lakes using a geo-statistical approach. *Nature Communications, 7*, 13603

Mishra, V., Cherkauer, K.A., & Bowling, L.C. (2010). Parameterization of lakes and wetlands for energy and water balance studies in the great lakes region. *Journal of Hydrometeorology, 11*, 1057-1082

Mohammed, I.N., & Tarboton, D.G. (2011). On the interaction between bathymetry and climate in the system dynamics and preferred levels of the Great Salt Lake. *Water Resources Research, 47*

Moknatian, M., Piasecki, M., & Gonzalez, J. (2017). Development of Geospatial and Temporal Characteristics for Hispaniola's Lake Azuei and Enriquillo Using Landsat Imagery. *Remote Sensing, 9*, 510

Morris, G.L. (2014). Sediment management and sustainable use of reservoirs. In *Modern water resources engineering* (pp. 279-337): Springer

Moy, W.S., Cohon, J.L., & ReVelle, C.S. (1986). A programming model for analysis of the reliability, resilience, and vulnerability of a water supply reservoir. *Water Resources Research, 22*, 489-498

Muirhead, K., & Cracknell, A.P. (1986). Airborne lidar bathymetry. *International Journal of Remote Sensing, 7*, 597-614

Mulholland, P.J., & Elwood, J.W. (1982). The role of lake and reservoir sediments as sinks in the perturbed global carbon cycle. *Tellus, 34*, 490-499

Murdock, H.E., Gibb, D., André, T., Appavou, F., Brown, A., Epp, B., Kondev, B., McCrone, A., Musolino, E., & Ranalder, L. (2019). Renewables 2019 Global Status Report

Najibi, N., & Devineni, N. (2018). Recent trends in the frequency and duration of global floods. *Earth System Dynamics, 9*, 757–783

Ni, S., Chen, J., Wilson, C.R., Li, J., Hu, X., & Fu, R. (2018). Global terrestrial water storage changes and connections to ENSO events. *Surveys in Geophysics, 39*, 1-22

Nilsson, C., Reidy, C.A., Dynesius, M., & Revenga, C. (2005). Fragmentation and flow regulation of the world's large river systems. *Science, 308*, 405-408

Odhiambo, B.K., & Boss, S.K. (2004). Integrated echo sounder, GPS, and GIS for Reservoir sedimentation studies: examples from two Arkansas lakes. *JAWRA Journal of the American Water Resources Association, 40*, 981-997

Oki, T., & Kanae, S. (2006). Global hydrological cycles and world water resources. *Science, 313*, 1068-1072

Pekel, J.-F., Cottam, A., Gorelick, N., & Belward, A.S. (2016). High-resolution mapping of global surface water and its long-term changes. *Nature, 540*, 418-422

Phan, V.H., Lindenbergh, R., & Menenti, M. (2012). ICESat derived elevation changes of Tibetan lakes between 2003 and 2009. *International Journal of Applied Earth Observation and Geoinformation, 17*, 12-22

Phillips, T., Nerem, R., Fox‐Kemper, B., Famiglietti, J., & Rajagopalan, B. (2012). The influence of ENSO on global terrestrial water storage using GRACE. *Geophysical Research Letters, 39*

Pickens, A.H., Hansen, M.C., Hancher, M., Stehman, S.V., Tyukavina, A., Potapov, P., Marroquin, B., & Sherani, Z. (2020). Mapping and sampling to characterize global inland water dynamics from 1999 to 2018 with full Landsat time-series. *Remote Sensing of Environment, 243*, 111792

Plate, E.J. (2002). Flood risk and flood management. *Journal of Hydrology, 267*, 2-11

Rahmani, V., Kastens, J.H., DeNoyelles, F., Jakubauskas, M.E., Martinko, E.A., Huggins, D.H., Gnau, C., Liechti, P.M., Campbell, S.W., & Callihan, R.A. (2018). Examining storage capacity loss and sedimentation rate of large reservoirs in the central US Great Plains. *Water, 10*, 190

Ren, C.T., Li, C.Y., Jia, K.L., Zhang, S., Li, W.P., & Cao, Y.L. (2008). Water quality assessment for Ulansuhai Lake using fuzzy clustering and pattern recognition. *Chinese Journal of Oceanology and Limnology, 26*, 339-344

Rouse, W.R., Oswald, C.J., Binyamin, J., Spence, C., Schertzer, W.M., Blanken, P.D., Bussières, N., & Duguay, C.R. (2005). The role of northern lakes in a regional energy balance. *Journal of Hydrometeorology, 6*, 291-305

Rowan, J., Goodwill, P., & Greco, M. (1995). Temporal variability in catchment sediment yield determined from repeated bathymetric surveys: Abbeystead Reservoir, UK. *Physics and Chemistry of the Earth, 20*, 199-206

Salas, J.D., & Shin, H.-S. (1999). Uncertainty analysis of reservoir sedimentation. *Journal of Hydraulic Engineering, 125*, 339-350

Samuelsson, P., Kourzeneva, E., & Mironov, D. (2010). The impact of lakes on the European climate as stimulated by a regional climate madel. *Boreal Environment Research, 15*

Saylam, K., Brown, R.A., & Hupp, J.R. (2017). Assessment of depth and turbidity with airborne Lidar bathymetry and multiband satellite imagery in shallow water bodies of the Alaskan North Slope. *International Journal of Applied Earth Observation and Geoinformation, 58*, 191-200

Schleiss, A.J., Franca, M.J., Juez, C., & De Cesare, G. (2016). Reservoir sedimentation. *Journal of Hydraulic Research, 54*, 595-614

Schutz, B.E., Zwally, H., Shuman, C., Hancock, D., & DiMarzio, J. (2005). Overview of the ICESat mission. *Geophysical Research Letters, 32*

Schwatke, C., Dettmering, D., Bosch, W., & Seitz, F. (2015). DAHITI–an innovative approach for estimating water level time series over inland waters using multi-mission satellite altimetry. *Hydrology and Earth System Sciences, 19*, 4345-4364

Seckler, D., Barker, R., & Amarasinghe, U. (1999). Water scarcity in the twenty-first century. *International Journal of Water Resources Development, 15*, 29-42

Shin, S., Pokhrel, Y., & Miguez-Macho, G. (2019). High-Resolution Modeling of Reservoir Release and Storage Dynamics at the Continental Scale. *Water Resources Research, 55*, 787-810

Smith, L.C., Sheng, Y., MacDonald, G., & Hinzman, L. (2005). Disappearing arctic lakes. *Science, 308*, 1429-1429

Song, C., Huang, B., & Ke, L. (2013). Modeling and analysis of lake water storage changes on the Tibetan Plateau using multi-mission satellite data. *Remote Sensing of Environment, 135*, 25-35

Svoboda, M., LeComte, D., Hayes, M., Heim, R., Gleason, K., Angel, J., Rippey, B., Tinker, R., Palecki, M., & Stooksbury, D. (2002). The drought monitor. *Bulletin of the American Meteorological Society, 83*, 1181-1190

Tranvik, L.J., Downing, J.A., Cotner, J.B., Loiselle, S.A., Striegl, R.G., Ballatore, T.J., Dillon, P., Finlay, K., Fortino, K., & Knoll, L.B. (2009). Lakes and reservoirs as regulators of carbon cycling and climate. *Limnology and Oceanography, 54*, 2298-2314

Tseng, K.-H., Shum, C., Kim, J.-W., Wang, X., Zhu, K., & Cheng, X. (2016). Integrating landsat imageries and digital elevation models to infer water level change in Hoover Dam. *IEEE Journal of Selected Topics in Applied Earth Observations and Remote Sensing, 9*, 1696-1709

Tufford, D.L., & McKellar, H.N. (1999). Spatial and temporal hydrodynamic and water quality modeling analysis of a large reservoir on the South Carolina (USA) coastal plain. *Ecological Modelling*, *114*, 137-173

Twichell, D.C., Cross, V.A., & Belew, S.D. (2003). Mapping the floor of Lake Mead (Nevada and Arizona): Preliminary discussion and GIS data release.

Udall, B., & Overpeck, J. (2017). The twenty-first century Colorado River hot drought and implications for the future. *Water Resources Research*, *53*, 2404-2418

USBR (1987). Design of small dams. *Water Resources Technical Publication Series*

USBR (2008). 2001 Lake Mead Sedimentation Survey, https://www.usbr.gov/tsc/techreferences/reservoir/2001%20Lake%20Mead%20Sedimentation%20Survey.pdf

USBR (2011). 2009 Lake Mead LiDAR Survey, https://www.usbr.gov/lc/region/g2000/2009MeadLIDARsurvey.pdf

Veldkamp, T., Wada, Y., Aerts, J., Döll, P., Gosling, S.N., Liu, J., Masaki, Y., Oki, T., Ostberg, S., & Pokhrel, Y. (2017). Water scarcity hotspots travel downstream due to human interventions in the 20th and 21st century. *Nature Communications*, *8*, 15697

Voisin, N., Hejazi, M.I., Leung, L.R., Liu, L., Huang, M., Li, H.Y., & Tesfa, T. (2017). Effects of spatially distributed sectoral water management on the redistribution of water resources in an integrated water model. *Water Resources Research*, *53*, 4253-4270

Votruba, L., & Broža, V. (1989). Water management in reservoirs. Elsevier

Wang, C.-K., & Philpot, W.D. (2007). Using airborne bathymetric lidar to detect bottom type variation in shallow waters. *Remote Sensing of Environment*, *106*, 123-135

Wang, H., Jia, L., Steffen, H., Wu, P., Jiang, L., Hsu, H., Xiang, L., Wang, Z., & Hu, B. (2013). Increased water storage in North America and Scandinavia from GRACE gravity data. *Nature Geoscience, 6*, 38-42

WCD (2000). Dams and development: A new framework for decision-making: The report of the world commission on dams. Earthscan

Wisser, D., Frolking, S., Hagen, S., & Bierkens, M.F. (2013). Beyond peak reservoir storage? A global estimate of declining water storage capacity in large reservoirs. *Water Resources Research, 49*, 5732-5739

Wood, E.F., Roundy, J.K., Troy, T.J., Van Beek, L., Bierkens, M.F., Blyth, E., de Roo, A., Döll, P., Ek, M., & Famiglietti, J. (2011). Hyperresolution global land surface modeling: Meeting a grand challenge for monitoring Earth's terrestrial water. *Water Resources Research, 47*

Wright, R., Garbeil, H., Baloga, S.M., & Mouginis-Mark, P.J. (2006). An assessment of shuttle radar topography mission digital elevation data for studies of volcano morphology. *Remote Sensing of Environment, 105*, 41-53

Wulder, M.A., White, J.C., Loveland, T.R., Woodcock, C.E., Belward, A.S., Cohen, W.B., Fosnight, E.A., Shaw, J., Masek, J.G., & Roy, D.P. (2016). The global Landsat archive: Status, consolidation, and direction. *Remote Sensing of Environment, 185*, 271-283

WWAP (2019). The United Nations World Water Development Report 2019: Leaving No One Behind. In: UNESCO World Water Assessment Programme Paris

Yamazaki, D., Ikeshima, D., Tawatari, R., Yamaguchi, T., O'Loughlin, F., Neal, J.C., Sampson, C.C., Kanae, S., & Bates, P.D. (2017). A high accuracy map of global terrain elevations. *Geophysical Research Letters, 44,* 5844-5853

Yang, L., Meng, X., & Zhang, X. (2011). SRTM DEM and its application advances. *International Journal of Remote Sensing, 32,* 3875-3896

Yao, F., Wang, J., Wang, C., & Crétaux, J.-F. (2019). Constructing long-term high-frequency time series of global lake and reservoir areas using Landsat imagery. *Remote Sensing of Environment, 232,* 111210

Yao, F., Wang, J., Yang, K., Wang, C., Walter, B.A., & Crétaux, J.-F. (2018). Lake storage variation on the endorheic Tibetan Plateau and its attribution to climate change since the new millennium. *Environmental Research Letters, 13,* 064011

Yigzaw, W., Li, H.Y., Demissie, Y., Hejazi, M.I., Leung, L.R., Voisin, N., & Payn, R. (2018). A New Global Storage-Area-Depth Dataset for Modeling Reservoirs in Land Surface and Earth System Models. *Water Resources Research, 54,* 10,372-10,386

Zajac, Z., Revilla-Romero, B., Salamon, P., Burek, P., Hirpa, F.A., & Beck, H. (2017). The impact of lake and reservoir parameterization on global streamflow simulation. *Journal of Hydrology, 548,* 552-568

Zarfl, C., Lumsdon, A.E., Berlekamp, J., Tydecks, L., & Tockner, K. (2015). A global boom in hydropower dam construction. *Aquatic Sciences, 77,* 161-170

Zeileis, A., Leisch, F., Hornik, K., & Kleiber, C. (2001). strucchange. An R package for testing for structural change in linear regression models

Zhang, G., Xie, H., Kang, S., Yi, D., & Ackley, S.F. (2011). Monitoring lake level changes on the Tibetan Plateau using ICESat altimetry data (2003–2009). *Remote Sensing of Environment, 115*, 1733-1742

Zhang, G., Yao, T., Shum, C., Yi, S., Yang, K., Xie, H., Feng, W., Bolch, T., Wang, L., & Behrangi, A. (2017a). Lake volume and groundwater storage variations in Tibetan Plateau's endorheic basin. *Geophysical Research Letters, 44*, 5550-5560

Zhang, G., Zheng, G., Gao, Y., Xiang, Y., Lei, Y., & Li, J. (2017b). Automated water classification in the Tibetan plateau using Chinese GF-1 WFV data. *Photogrammetric Engineering & Remote Sensing, 83*, 509-519

Zhang, S., Foerster, S., Medeiros, P., de Araújo, J.C., Motagh, M., & Waske, B. (2016). Bathymetric survey of water reservoirs in north-eastern Brazil based on TanDEM-X satellite data. *Science of the Total Environment, 571*, 575-593

Zhang, S., & Gao, H. (2016). A novel algorithm for monitoring reservoirs under all‐weather conditions at a high temporal resolution through passive microwave remote sensing. *Geophysical Research Letters, 43*, 8052-8059

Zhang, S., Gao, H., & Naz, B.S. (2014). Monitoring reservoir storage in South Asia from multisatellite remote sensing. *Water Resources Research, 50*, 8927-8943

Zhao, G., & Gao, H. (2018). Automatic correction of contaminated images for assessment of reservoir surface area dynamics. *Geophysical Research Letters, 45*, 6092-6099

Zhao, G., & Gao, H. (2019). Estimating reservoir evaporation losses for the United States: Fusing remote sensing and modeling approaches. *Remote Sensing of Environment, 226*, 109-124

Zhao, G., Gao, H., Kao, S.-C., Voisin, N., & Naz, B.S. (2018). A modeling framework for evaluating the drought resilience of a surface water supply system under non-stationarity. *Journal of Hydrology, 563,* 22-32

Zhao, G., Gao, H., Naz, B.S., Kao, S.-C., & Voisin, N. (2016). Integrating a reservoir regulation scheme into a spatially distributed hydrological model. *Advances in Water Resources, 98,* 16-31

Zhou, T., Nijssen, B., Gao, H., & Lettenmaier, D.P. (2016). The contribution of reservoirs to global land surface water storage variations. *Journal of Hydrometeorology, 17,* 309-325

Zwally, H., Schutz, R., Bentley, C., Bufton, J., Herring, T., Minster, J., Spinhirne, J., & Thomas, R. (2011). GLAS/ICESat L2 Global Land Surface Altimetry Data. *Version 33,* 27

APPENDIX A

SUPPORTING INFORMATION FOR CHAPTER III

1. Validation of the A-E and E-V relationships

In Section 3.4.2.1, 16 reservoirs were selected to use for validation of the A-E and E-V relationships. Table S1 shows the summarization of remotely sensed bathymetry for these reservoirs. Figures S1 to S16 show the remotely sensed bathymetry maps over the Mead, Fort Peck, Oahe, Success, Sakakawea, Powell, Gandhi Sagar, Hirakud, Jayakwadi, Malaprabha, Matatila, Sriram Sagar, Srisailam, Tawa, Tungabhadra, and Indravati reservoirs, respectively. For Lake Mead, since results based on A-E relationships derived from ICESat and Hydroweb radar altimetry have the same spatial patterns, only the ICESat based bathymetry is shown.

In this dataset, the smallest reservoir detected by ICESat is Mehgaon Tola Tank (India), which has an average area of 1.47 km^2. Clear patterns can be observed from the bathymetry map (Figure S17).

Table S1 Summary of the remotely sensed bathymetry for the reservoirs used for validation

Reservoir name	Min elev.(m)	Max elev.(m)	Elev range (m)	Total area (km^2)	Dynamic area (km^2)/fraction (%)	Storage capacity (km^3)	Dynamic storage (km^3)/ fraction (%)
Mead (ICESat)	329.71	368.25	38.54	583.64	282.97/48.48%	34.07	21.36/62.69%
Mead (Hydroweb)	327.70	369.64	41.94	583.64	282.97/48.48%	34.07	23.24/68.22%
Fort Peck	667.92	683.98	16.06	929.22	367.13/39.51%	22.77	16.91/74.2
Oahe	478.88	491.69	12.81	1333.73	590.07/44.24%	28.35	16.36/57.70%
Success	174.02	203.10	29.08	7.92	7.65/96.53%	0.10	0.10/100%
Sakakawea	552.21	563.30	11.09	1404.34	449.21/31.99%	29.38	13.08/44.50%
Powell	1078.28	1123.64	45.36	578.99	334.20/57.72%	30.00	18.68/62.27%
Gandhi Sagar	380.97	399.10	18.13	596.08	538.61/90.36%	6.83	5.92/86.68%
Hirakud	181.85	190.43	8.58	597.65	389.61/65.19%	4.82	3.84/79.58%
Jayakwadi	454.25	462.70	8.45	344.51	264.00/76.63%	2.17	1.73/79.72%
Malaprabha	621.48	632.93	11.45	110.89	89.35/80.57%	0.92	0.78/84.85%
Matatila	299.70	308.25	8.55	109.94	85.24/77.53%	0.64	0.58/90.88%
Sriram Sagar	320.44	332.82	12.38	321.40	309.21/96.21%	2.3	1.91/83.04%
Srisailam	253.82	269.64	15.82	529.12	512.23/96.81%	6.12	4.32/70.68%
Tawa	339.03	355.05	16.02	167.31	144.43/86.33%	1.94	1.55/79.65%
Tungabhadra	483.82	497.87	14.05	352.59	340.95/96.70%	2.86	2.56/89.54%
Indravati	630.52	642.03	11.51	111.74	34.38/30.77%	1.46	1.12/77.15%

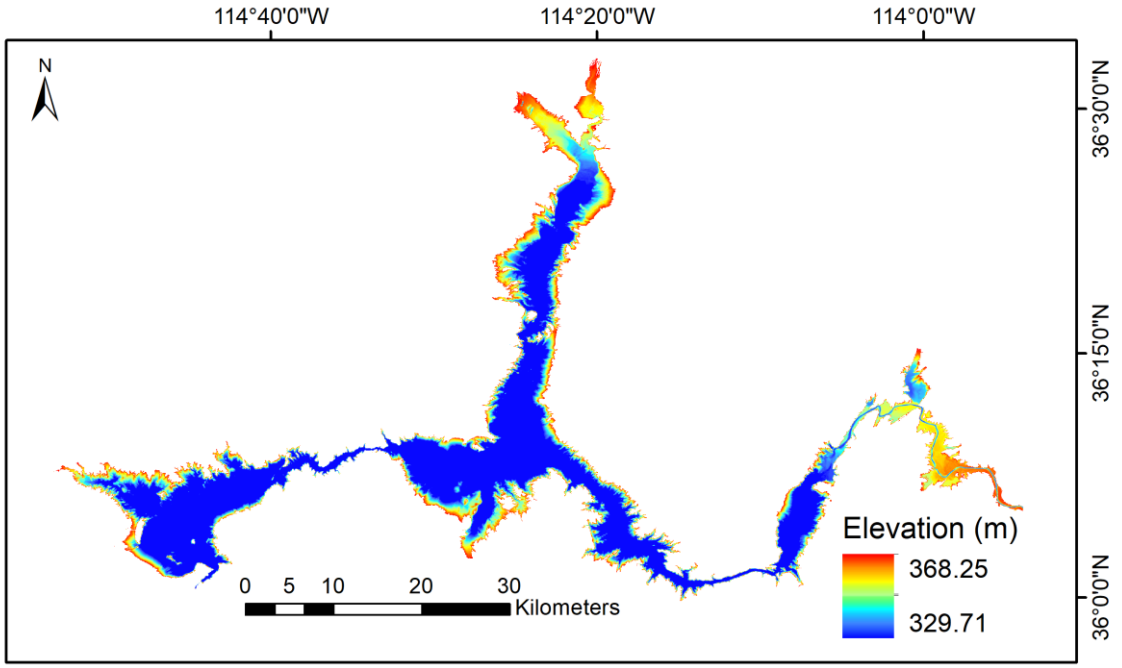

Figure S1 Remotely sensed bathymetry over Lake Mead (ICESat based).

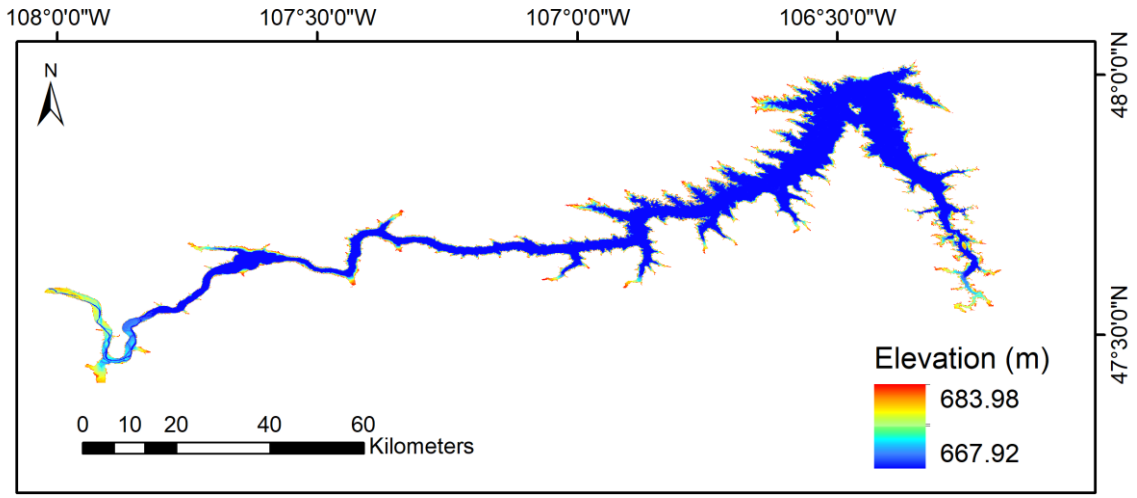

Figure S2 Remotely sensed bathymetry over Lake Fort Peck.

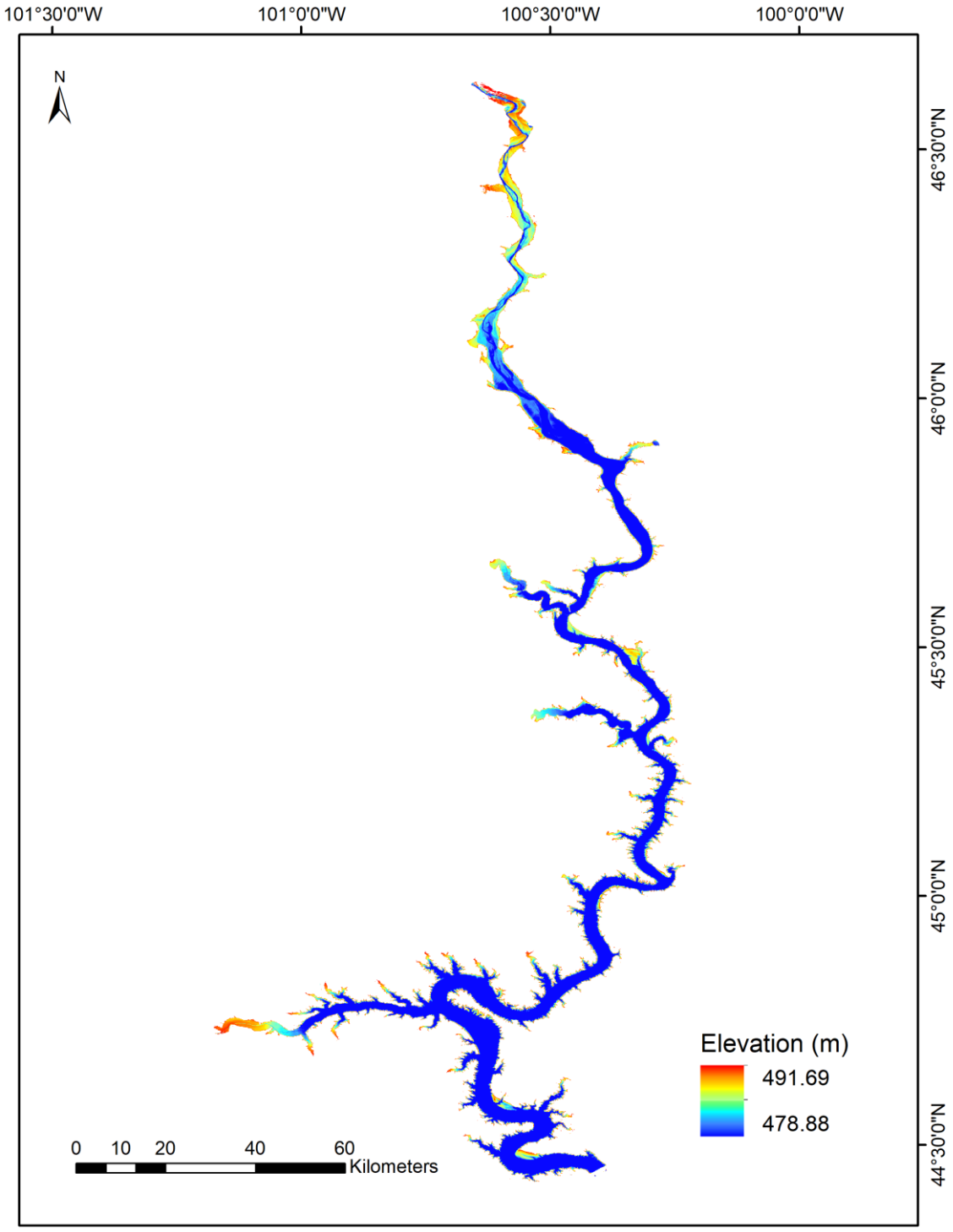

Figure S3 Remotely sensed bathymetry over Lake Oahe.

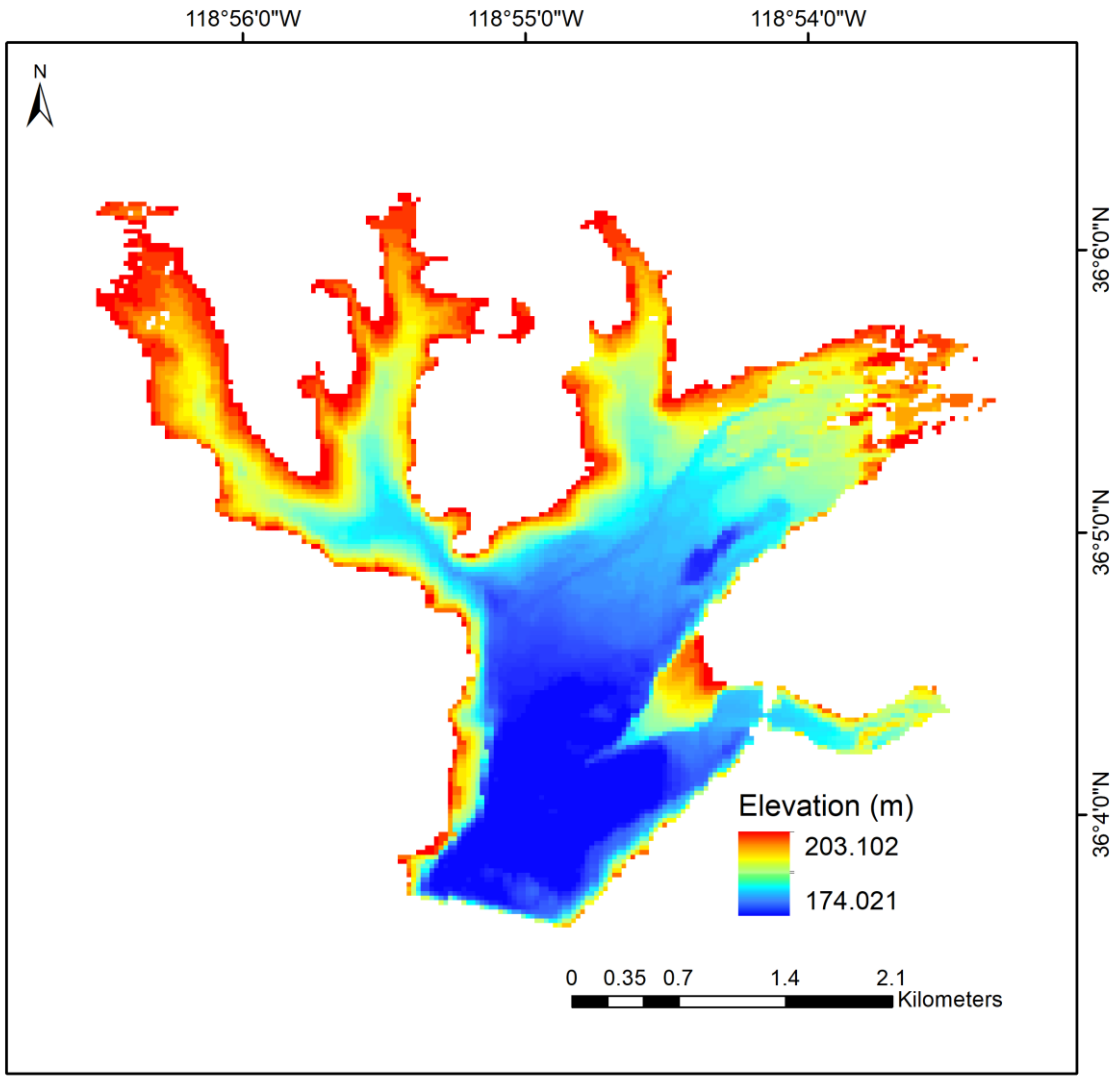

Figure S4 Remotely sensed bathymetry over Lake Success.

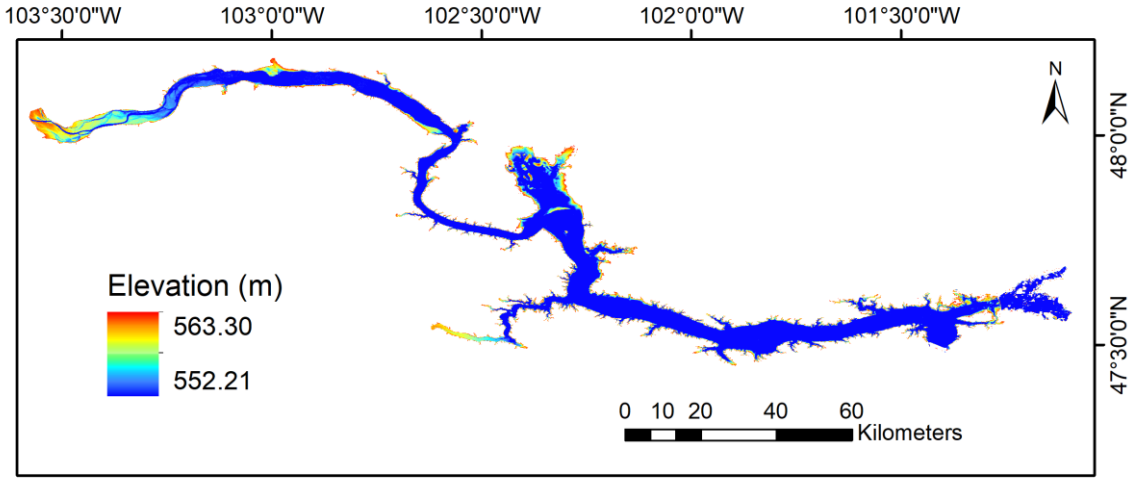

Figure S5 Remotely sensed bathymetry over Lake Sakakawea.

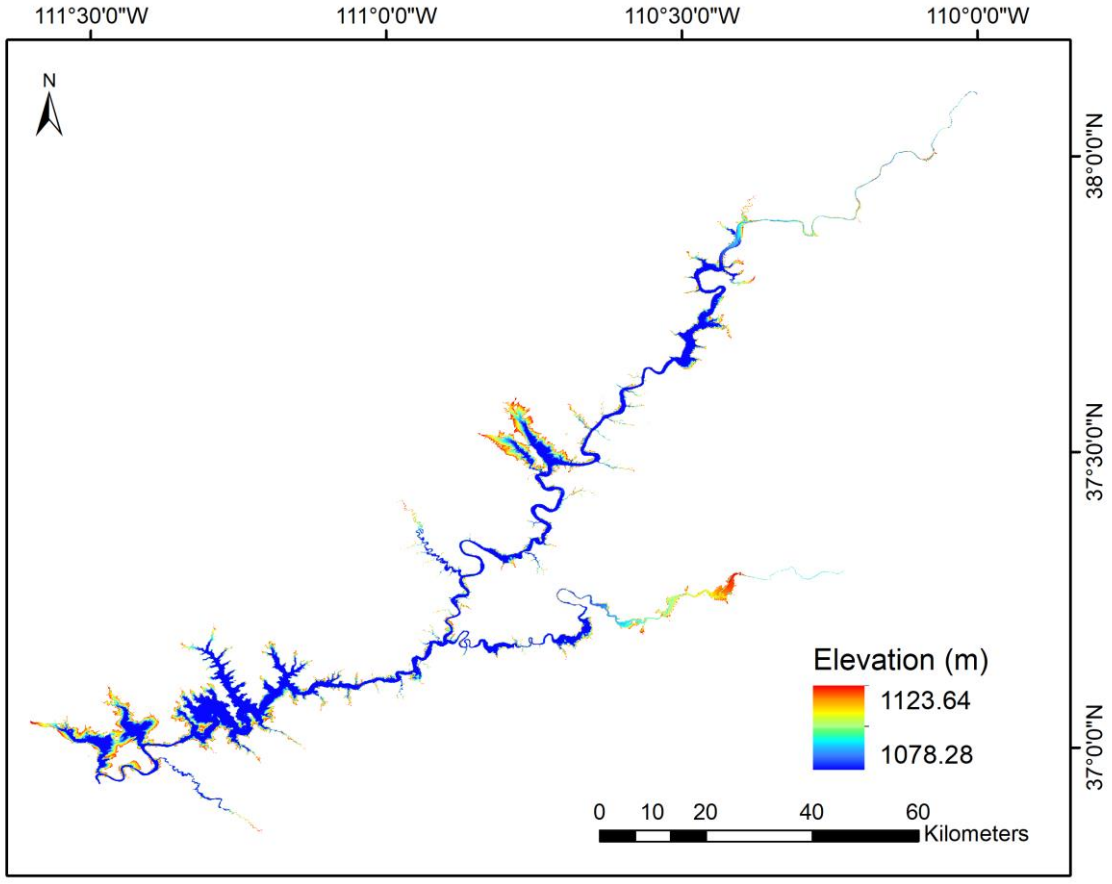

Figure S6 Remotely sensed bathymetry over Lake Powell.

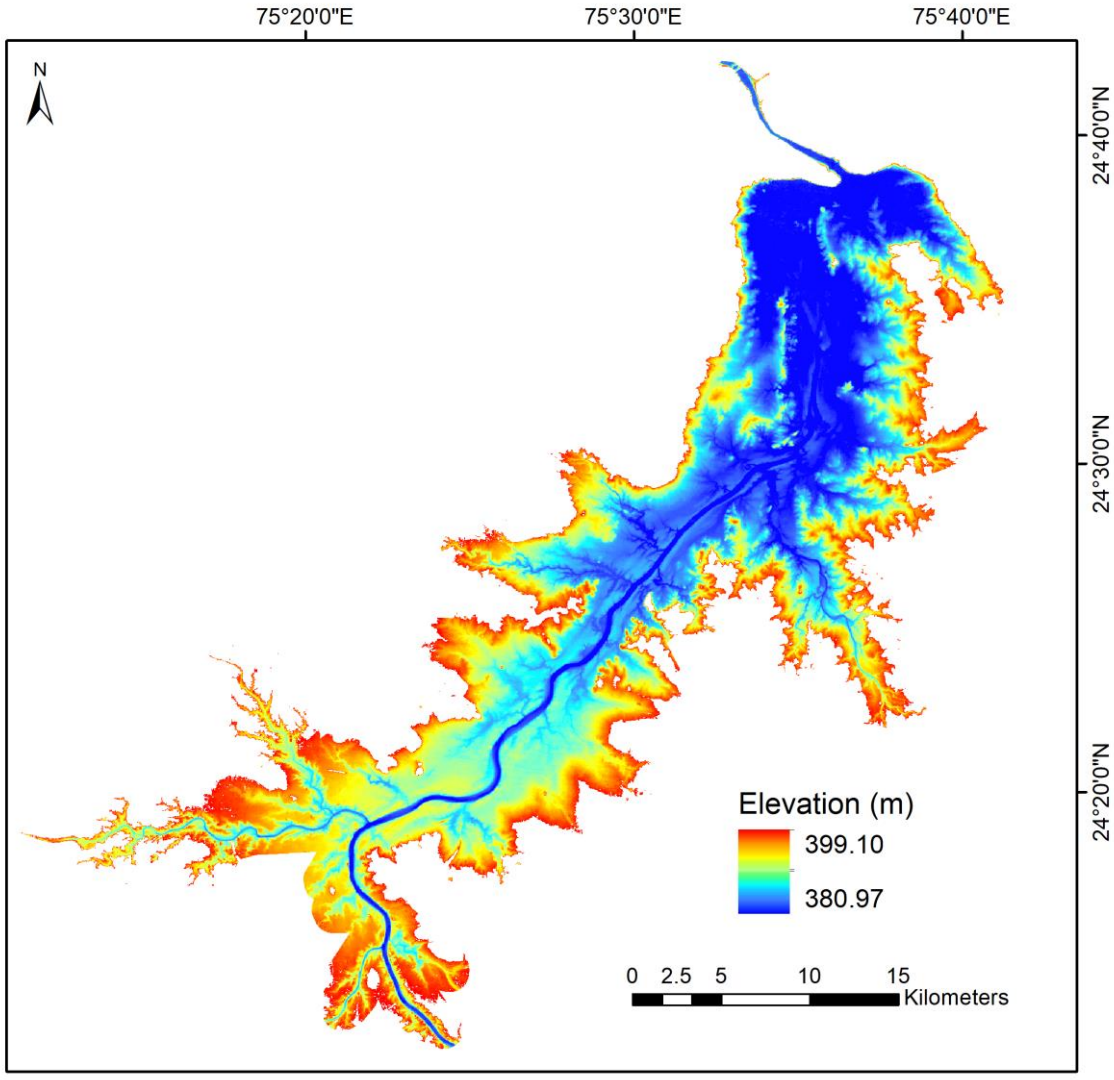

Figure S7 Remotely sensed bathymetry over Gandhi Sagar Reservoir.

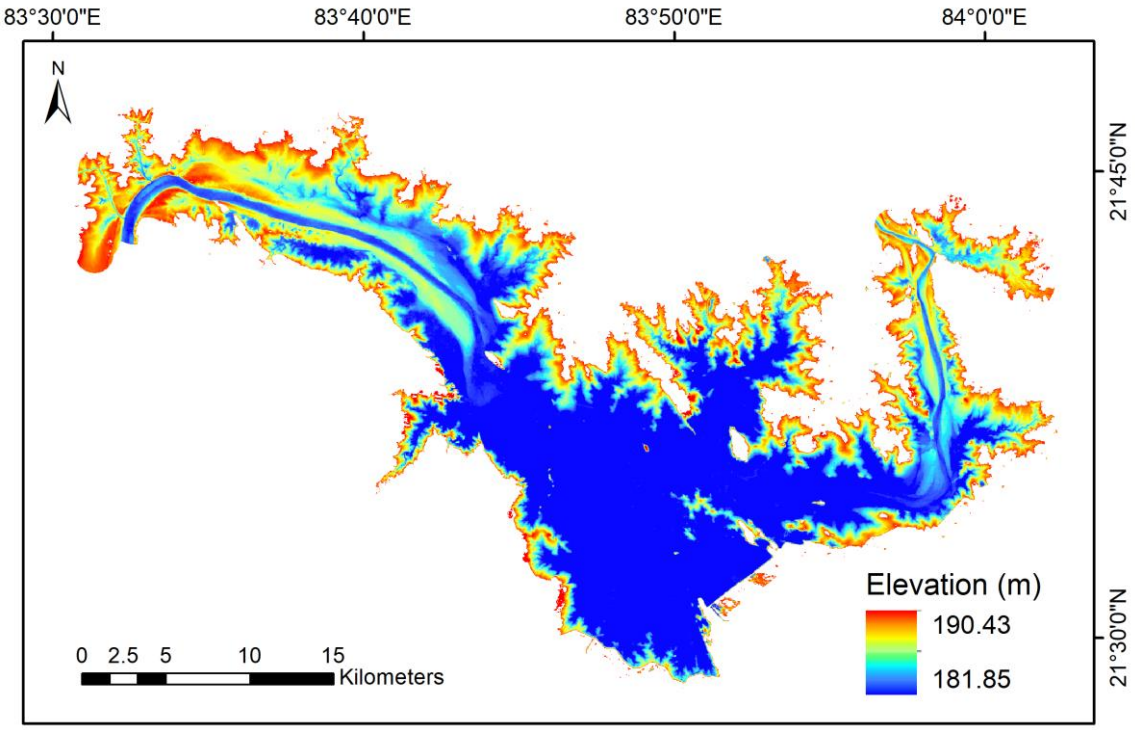

Figure S8 Remotely sensed bathymetry over Hirakud Reservoir.

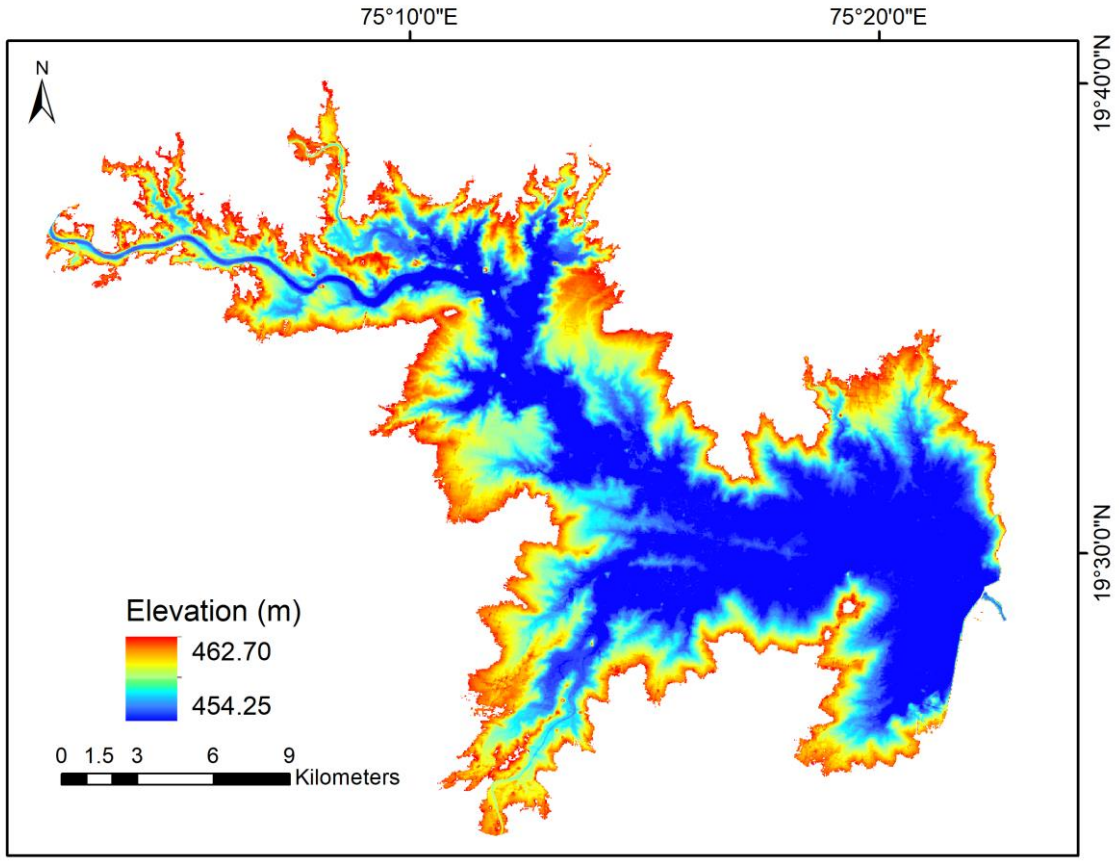

Figure S9 Remotely sensed bathymetry over Jayakwadi Reservoir.

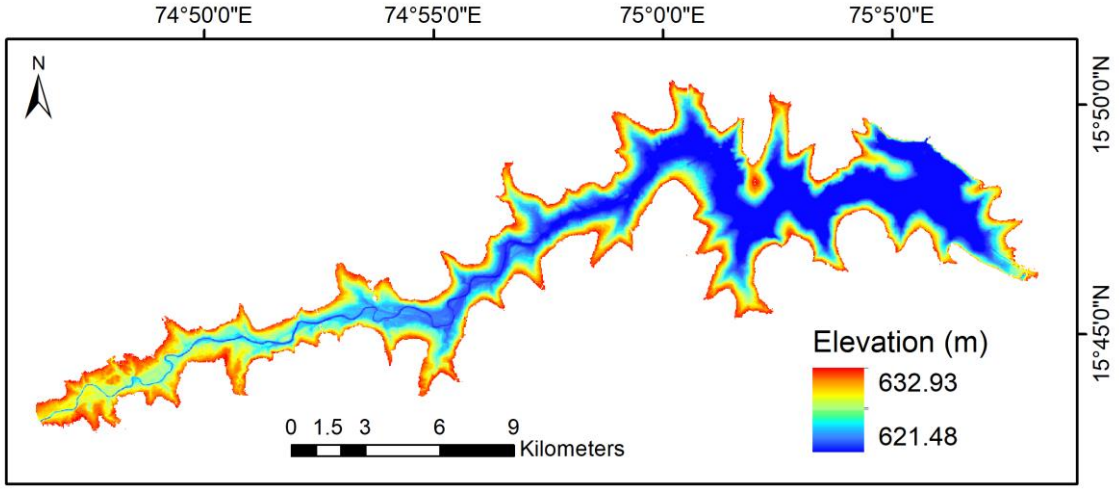

Figure S10 Remotely sensed bathymetry over Malaprabha Reservoir.

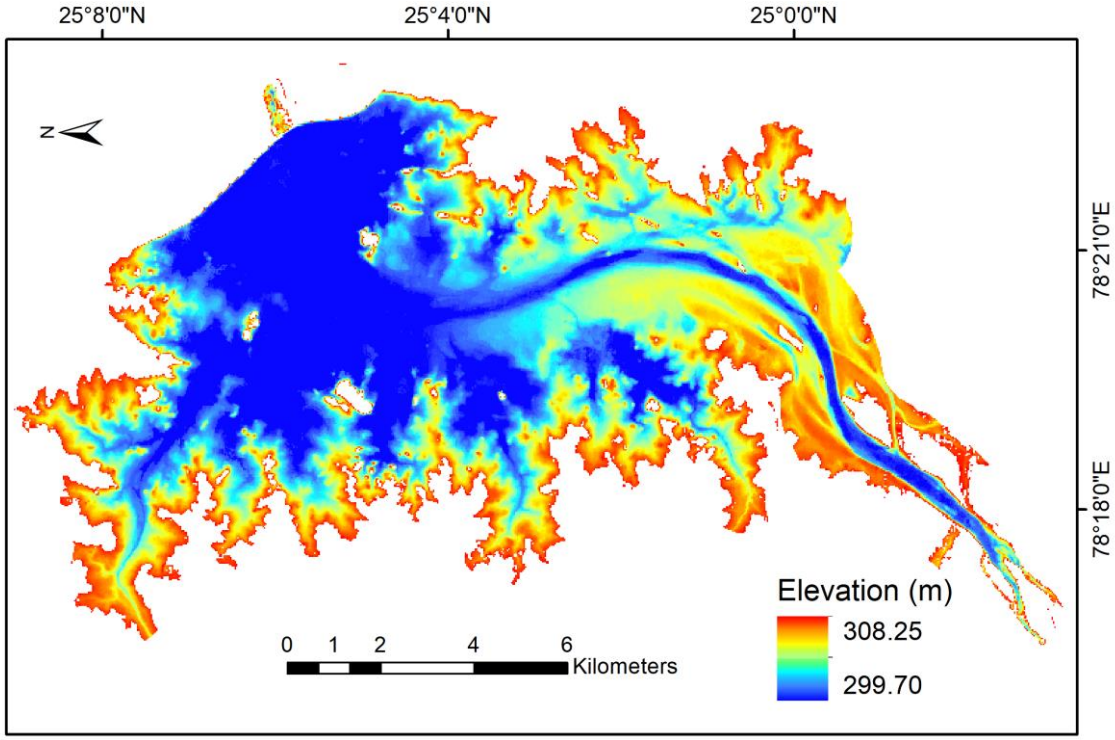

Figure S11 Remotely sensed bathymetry over Matatila Reservoir.

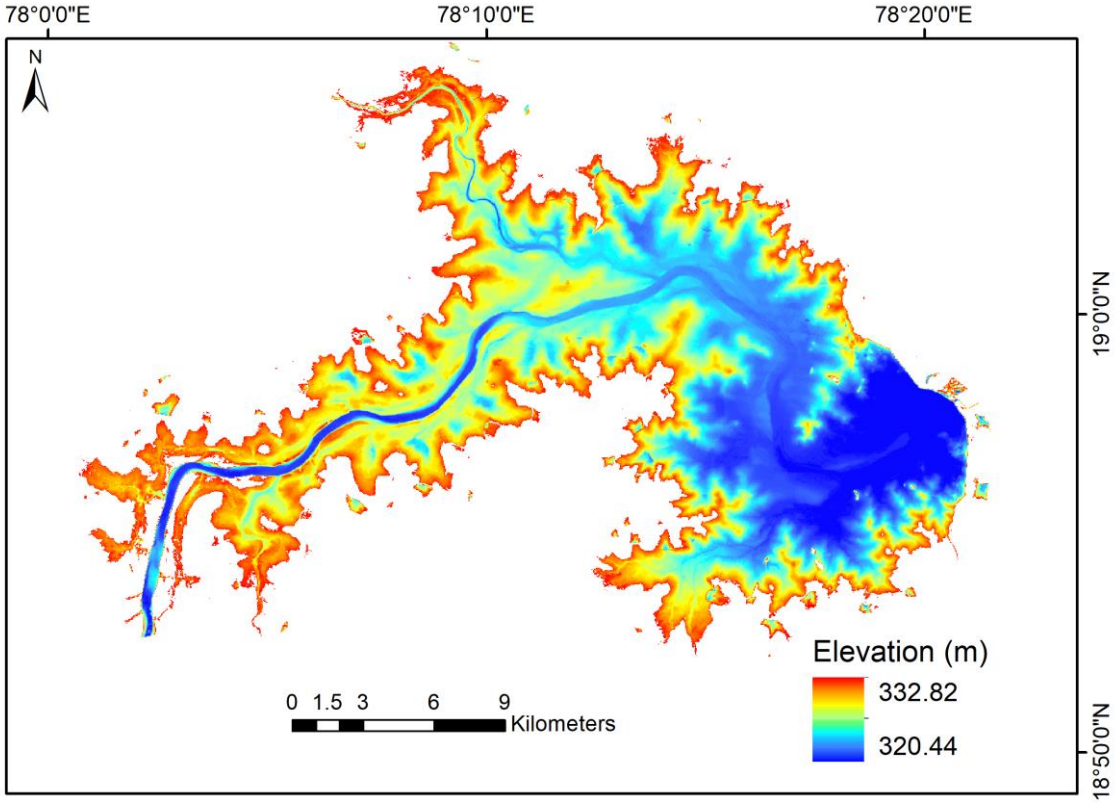

Figure S12 Remotely sensed bathymetry over Sriram Sagar Reservoir.

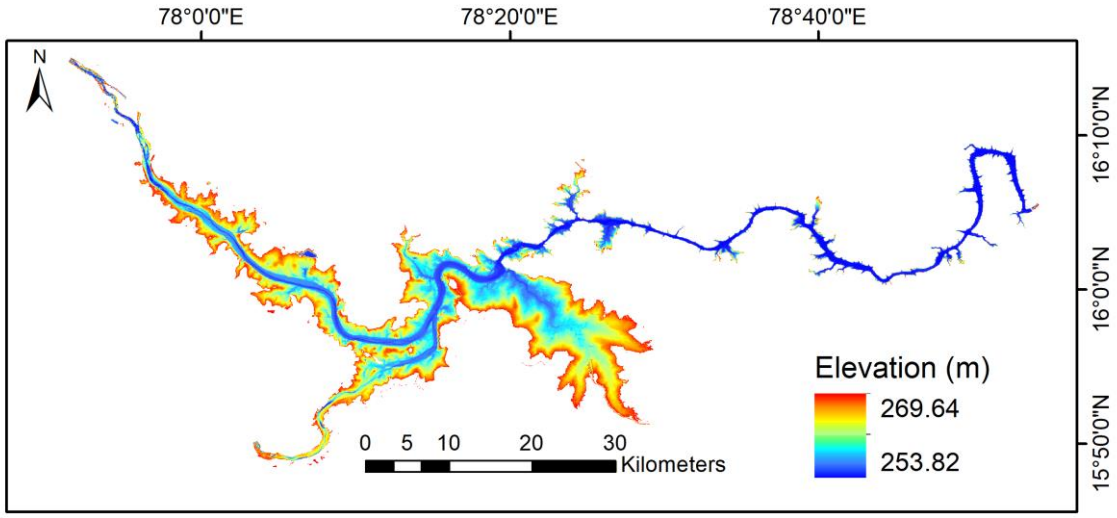

Figure S13 Remotely sensed bathymetry over Srisailam Reservoir.

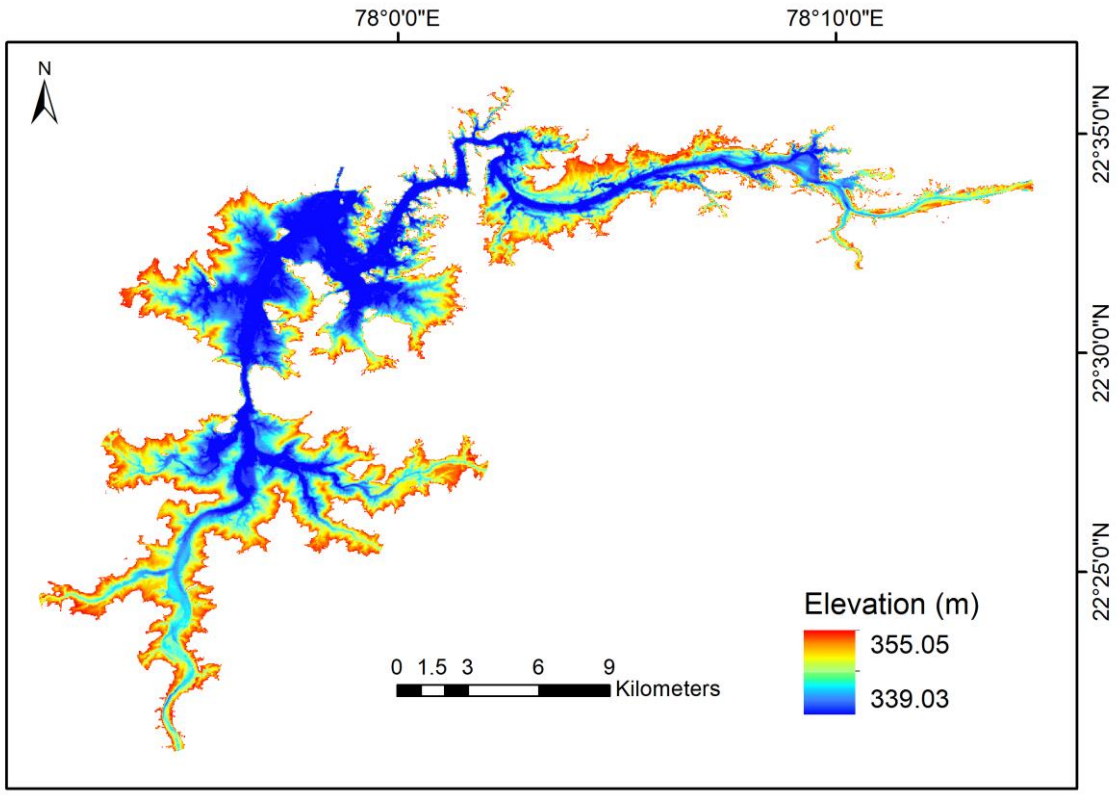

Figure S14 Remotely sensed bathymetry over Tawa Reservoir.

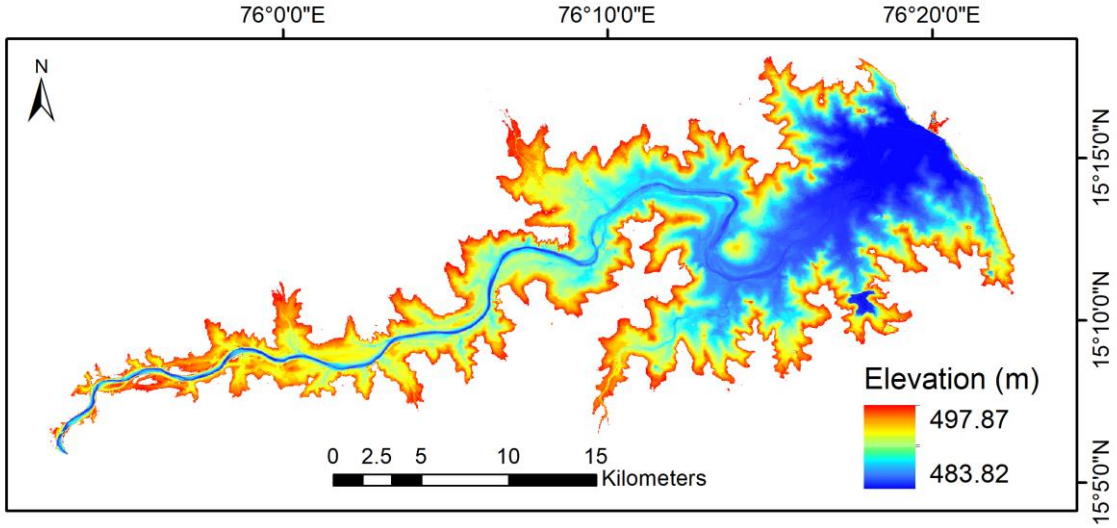

Figure S15 Remotely sensed bathymetry over Tungabhadra Reservoir.

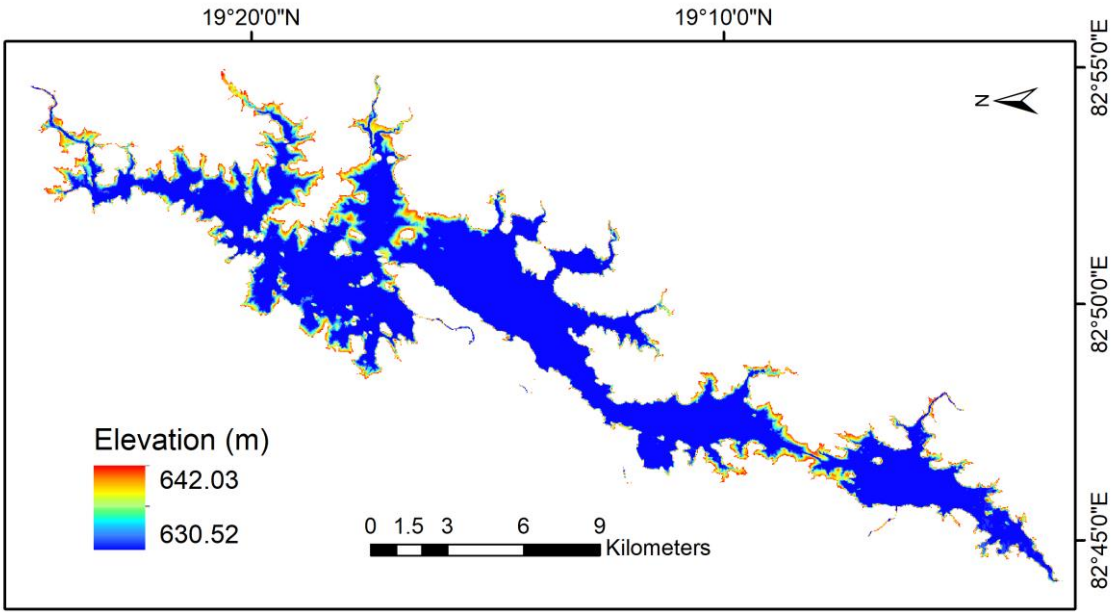

Figure S16 Remotely sensed bathymetry over Indravati Reservoir.

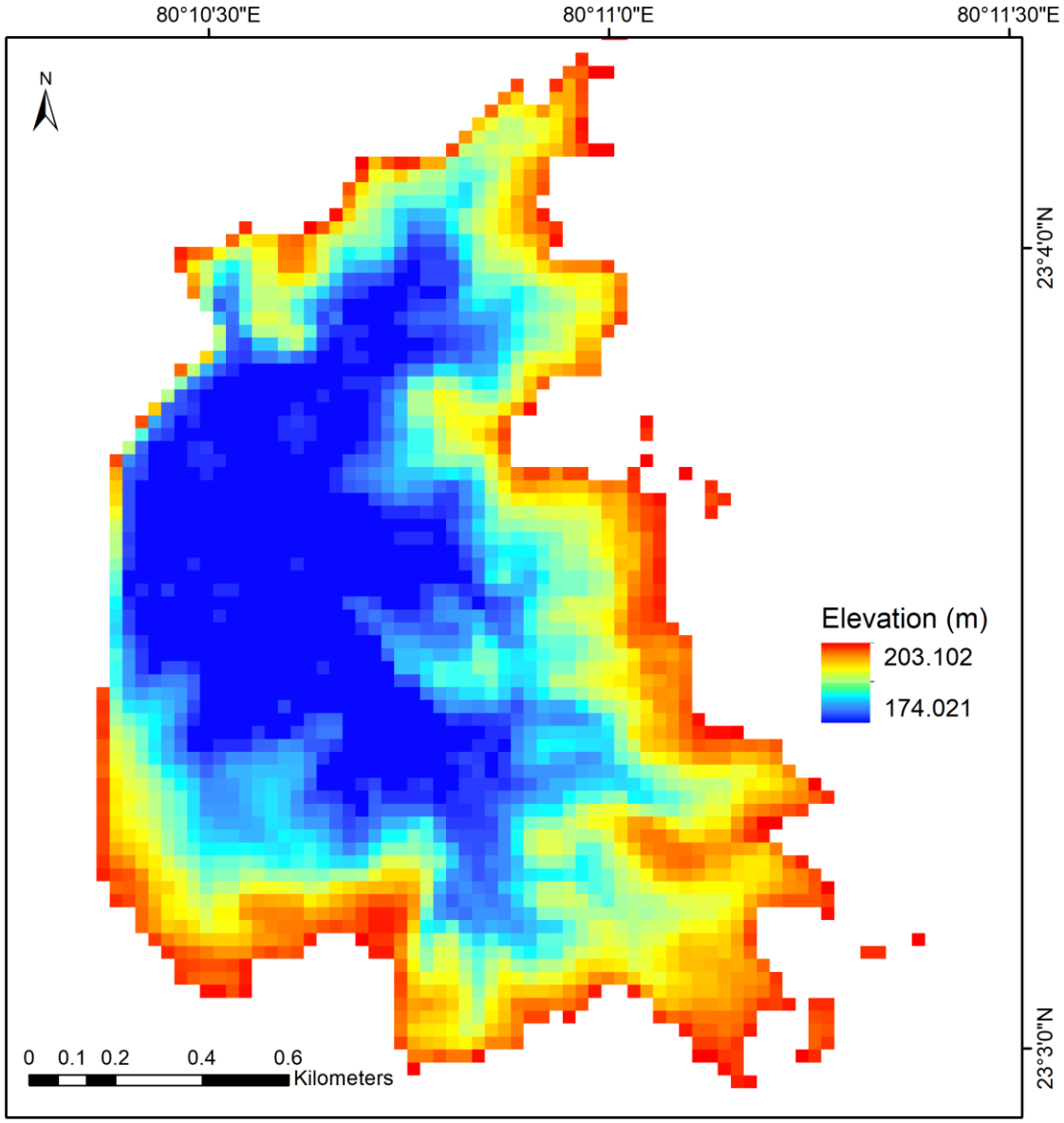

Figure S17 Remotely sensed bathymetry over Mehgaon Tola Tank.

2. Validation against surveyed bathymetry values

In Section 3.4.2.2, four reservoirs were selected to validate the remotely sensed bathymetry against surveyed bathymetry values. For each of these reservoirs, we selected four transects—evenly distributed over the reservoir area—which were used to compare the elevation values from the remotely sensed bathymetry with their counterparts from the surveyed bathymetry. The remotely sensed bathymetry maps and the locations of validation transects for Lake Roosevelt, Cascade Reservoir, and Clear Lake Reservoir are shown in Figures S18 to S20, respectively (those for Lake Mead are shown in Figure 3.8a–e). Moreover, the statistics of the validation results over the selected transects are shown in Table S2.

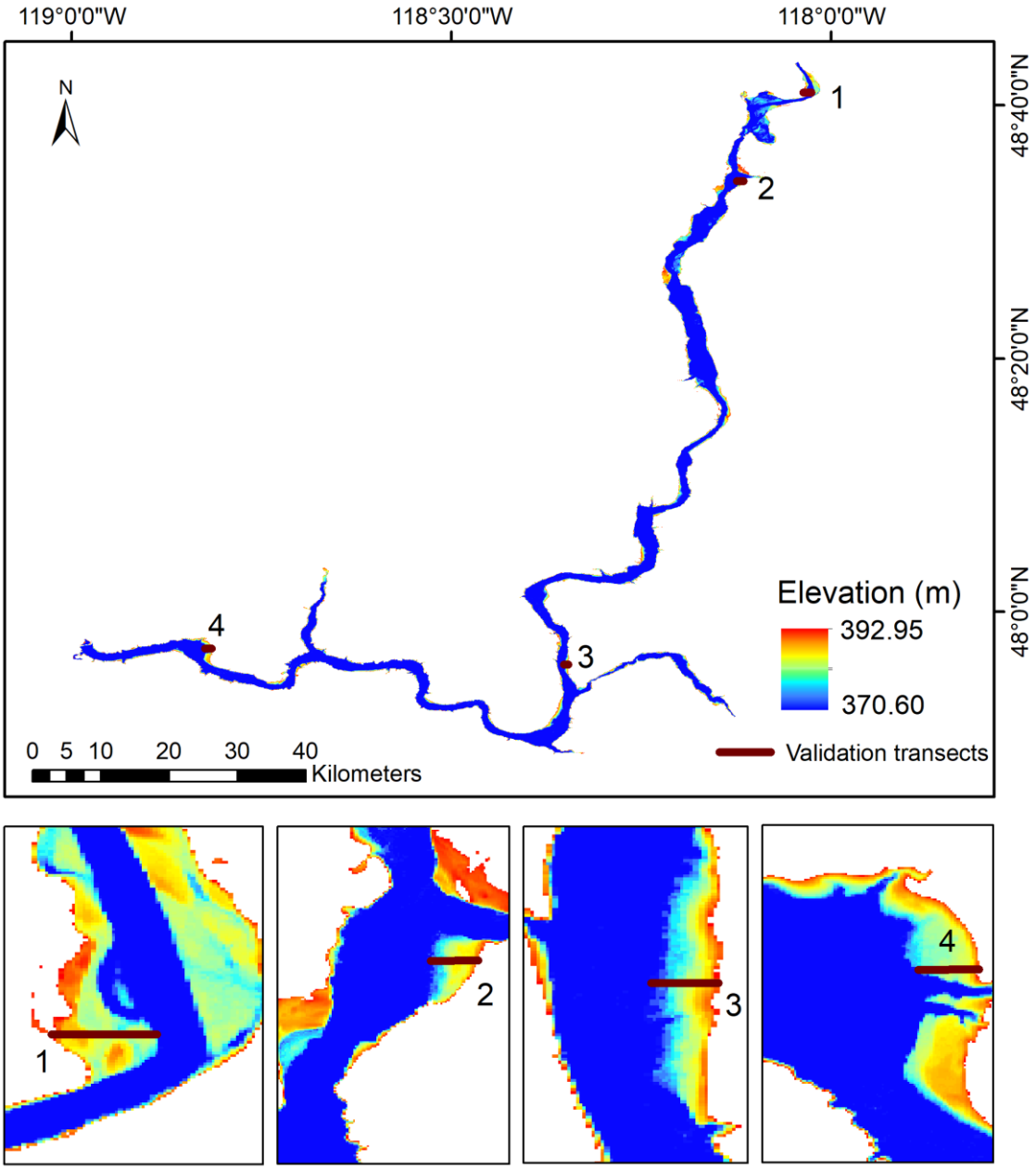

Figure S18 Remotely sensed bathymetry over Lake Roosevelt and the locations of the validation transects.

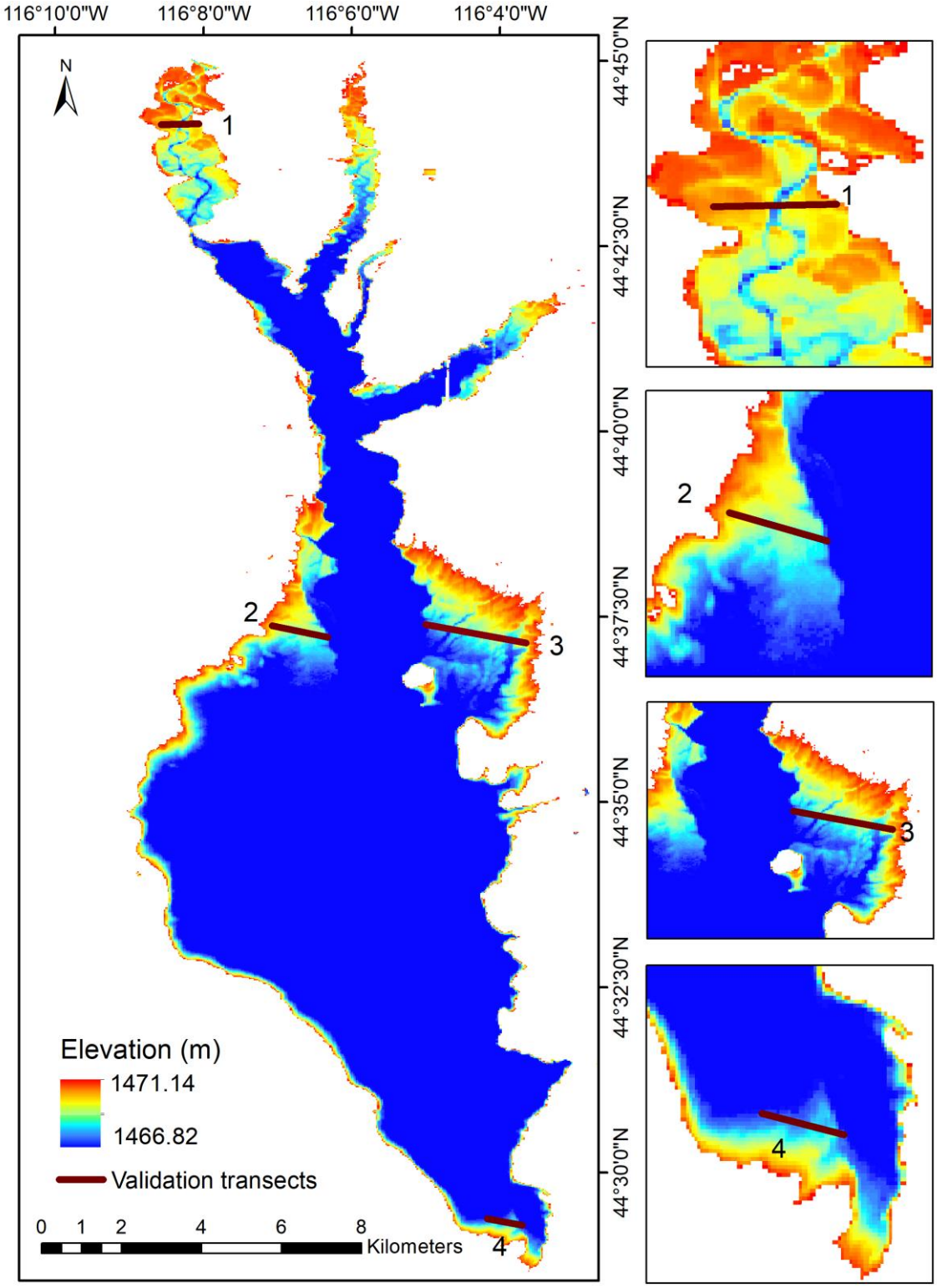

Figure S19 Remotely sensed bathymetry over the Cascade Reservoir and the locations of the validation transects.

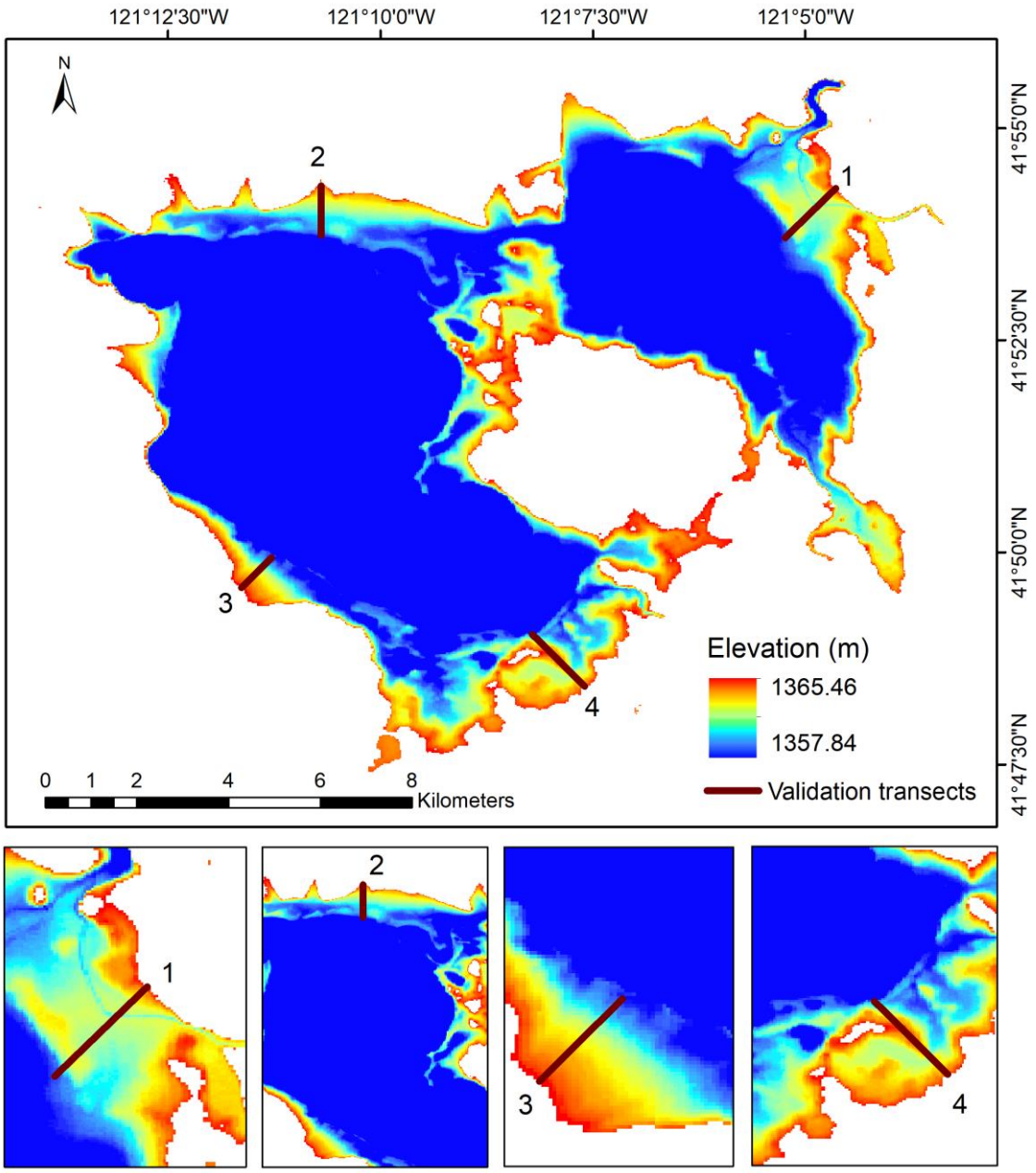

Figure S20 Remotely sensed bathymetry over Clear Lake Reservoir and the locations of the validation transects.

Table S2 Statistics of the validation results over the selected transects

Reservoir /Transect	Elevation dataset	Max (m)	Min (m)	Mean (m)	SD[a] (m)	N[b]	R^2	RMSE (m)
Lake Mead (ICESat)								
1	ICESat	367.38	335.47	350.21	10.16	20	0.99	1.54
	Survey	368.81	334.67	351.02	10.77			
2	ICESat	367.38	336.55	342.78	8.06	75	0.98	1.78
	Survey	365.76	335.89	341.60	8.58			
3	ICESat	367.87	336.55	352.74	9.12	49	0.99	1.21
	Survey	369.42	334.67	353.17	9.48			
4	ICESat	367.68	337.06	358.03	4.41	86	0.82	1.97
	Survey	368.24	345.79	357.95	3.41			
Lake Mead (Hydroweb)								
1	Hydroweb	368.68	333.97	350.01	11.06	20	0.99	1.61
	Survey	368.81	334.67	351.02	10.77			
2	Hydroweb	368.68	335.14	341.92	8.77	75	0.98	1.33
	Survey	365.76	335.89	341.60	8.58			
3	Hydroweb	369.22	335.14	352.75	9.92	49	0.99	1.27
	Survey	369.42	334.67	353.17	9.48			
4	Hydroweb	369.02	335.69	358.51	4.80	86	0.82	2.31
	Survey	368.24	345.79	357.95	3.41			
Lake Roosevelt								
1	G-REALM	392.30	374.27	385.74	3.73	37	0.87	1.43
	Survey	392.83	373.93	386.27	3.31			
2	G-REALM	392.80	374.27	384.09	4.63	34	0.90	1.51
	Survey	392.48	377.88	384.14	3.87			
3	G-REALM	390.95	375.96	383.07	4.81	23	0.96	1.43
	Survey	391.30	374.28	384.02	5.30			
4	G-REALM	392.34	377.29	384.10	3.33	32	0.93	2.23
	Survey	392.58	372.77	382.20	4.04			
Cascade Reservoir								
1	G-REALM	1470.52	1467.46	1469.88	0.77	37	0.67	0.75
	Survey	1469.83	1467.63	1469.31	0.43			
2	G-REALM	1470.00	1467.65	1469.00	0.55	40	0.95	0.17
	Survey	1469.93	1467.61	1468.88	0.54			
3	G-REALM	1469.97	1467.35	1468.65	0.63	84	0.79	0.45
	Survey	1469.76	1465.97	1468.33	0.69			
4	G-REALM	1468.52	1467.01	1467.80	0.42	31	0.90	0.15
	Survey	1468.42	1467.34	1467.87	0.39			
Clear Lake Reservoir								
1	ICESat	1365.23	1358.62	1361.94	1.35	37	0.80	1.54
	Survey	1366.91	1361.68	1363.35	1.09			
2	ICESat	1364.66	1358.62	1361.43	1.64	39	0.86	1.58
	Survey	1366.05	1361.85	1362.84	1.19			
3	ICESat	1365.46	1358.26	1362.45	2.14	23	0.94	1.58
	Survey	1366.82	1361.48	1363.88	1.69			
4	ICESat	1365.27	1358.77	1363.22	1.55	39	0.89	1.33
	Survey	1366.70	1361.78	1464.43	1.26			

[a]SD represents standard deviation, and [b]N is the number of samples for each transect.

3. Evaluation of the projected bathymetry

In Section 3.4.2.3, we used Lake Mead and Cascade Reservoir to evaluate the performance of the projected bathymetry. Figure S21 shows the full bathymetry of Cascade Reservoir—including the remotely sensed portion (1466.82 m – 1471.14 m) and the projected portion (1461.00 m – 1466.81 m)—along with the locations of the transects used to validate the projected bathymetry. Figure S22 shows the comparison between the elevations of the projected bathymetry and their counterpart values from the sedimentation survey data over the Cascade Reservoir. Additionally, we compared the Area-Volume relationship derived from this study with those of Yigzaw et al. (2018) in Figure S23.

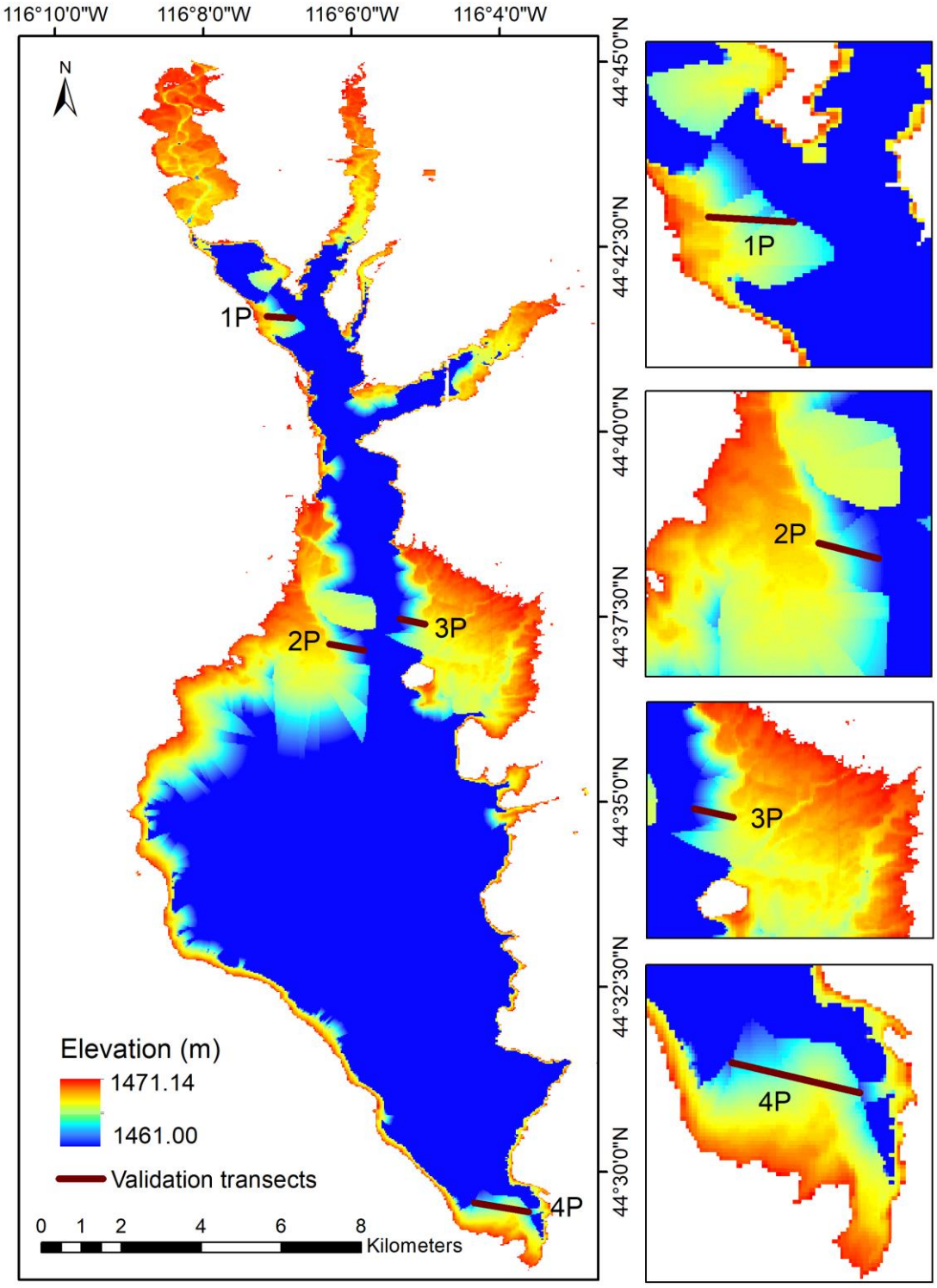

Figure S21 Full bathymetry of Cascade Reservoir (remotely sensed bathymetry plus projected bathymetry) and the locations of the validation transects over the projected bathymetry.

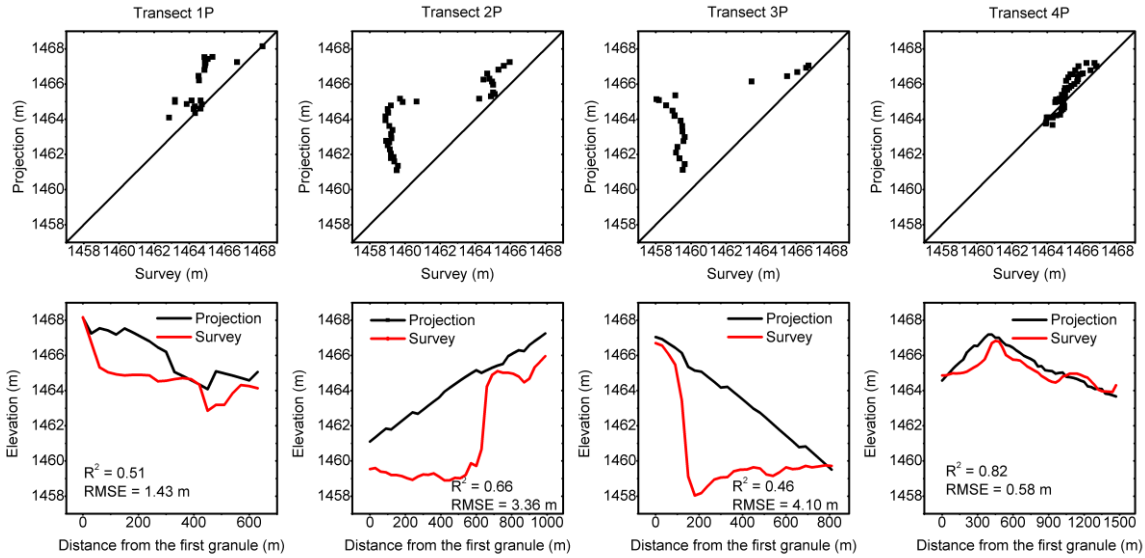

Figure S22 Scatter plots and elevation profiles for transects 1P, 2P, 3P, and 4P over Cascade Reservoir.

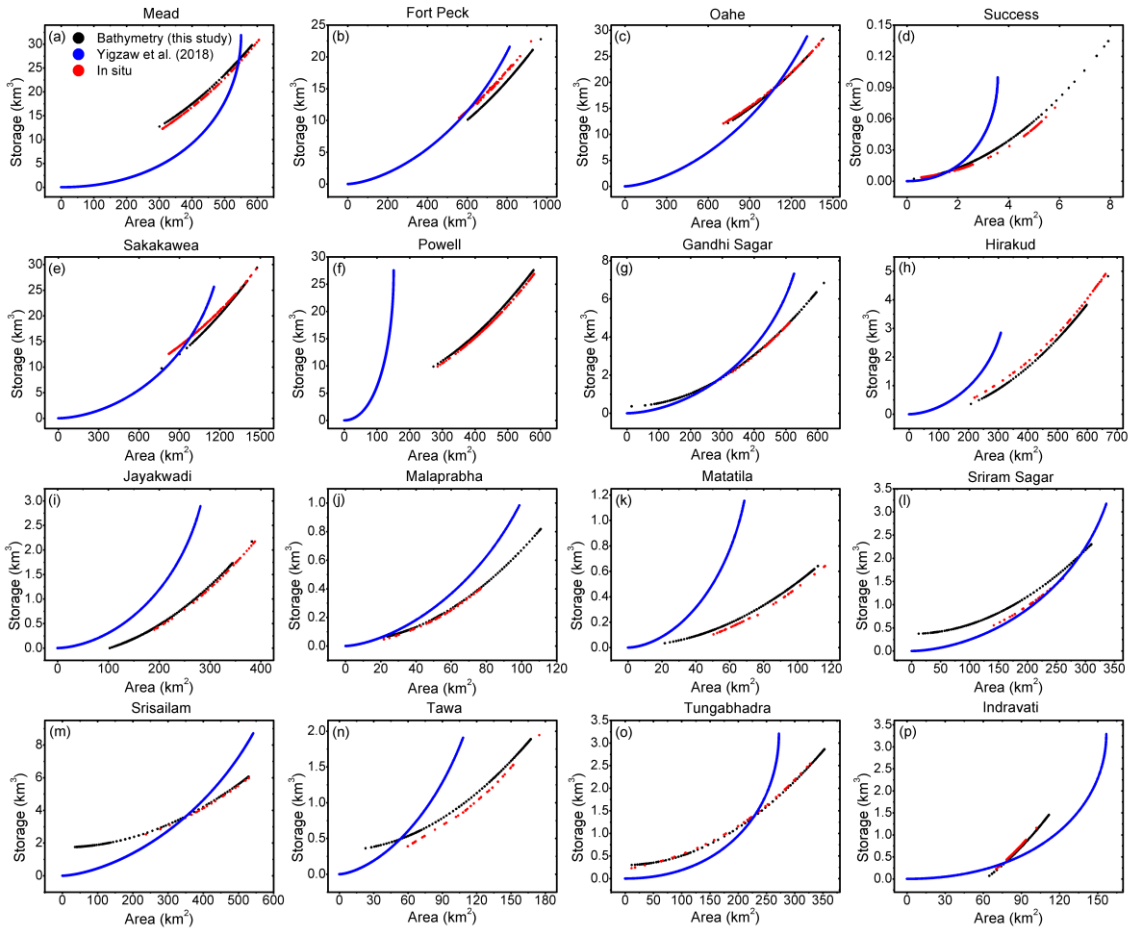

Figure S23 Comparison of Area-Volume (A-V) relationships derived from bathymetry (this study) and Yigzaw et al. (2018) over the (a) Mead, (b) Fort Peck, (c) Oahe, (d) Success, (e) Sakakawea, (f) Powell, (g) Gandhi Sagar, (h) Hirakud, (i) Jayakwadi, (j) Malaprabha, (k) Matatila, (l) Sriram Sagar, (m) Srisailam, (n) Tawa, (o) Tungabhadra, and (p) Indravati reservoirs.

APPENDIX B

SUPPORTING INFORMATION FOR CHAPTER IV

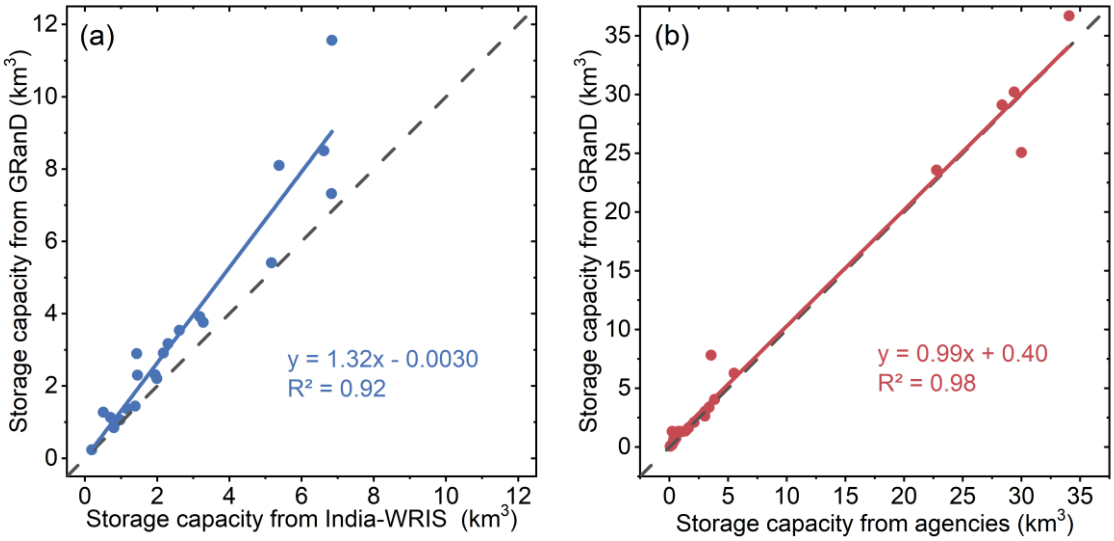

Figure S1 Comparison of storage capacity values from water management agencies and GRanD for reservoirs in (a) India, and (b) the United States and Australia.

Table S1 Hypothesis test results of regression models for (a) North America, (b) Africa, and (c) South America.

Regression Equation (a)

Condition			
A	Operating rate	=	0.75251 + 0.000884 Time
B	Operating rate	=	0.75116 + 0.000902 Time

Coefficients

Term	Coef	SE Coef	T-Value	P-Value	VIF
Constant	0.75251	0.00254	296.60	0.000	
Time	0.000884	0.000220	4.01	0.000	2.00
Condition					
B	-0.00135	0.00359	-0.38	0.707	3.98
Time*Condition					
B	0.000018	0.000312	0.06	0.955	4.98

Regression Equation (b)

Condition			
A	Operating rate	=	0.74968 - 0.001102 Time
B	Operating rate	=	0.75008 - 0.000943 Time

Coefficients

Term	Coef	SE Coef	T-Value	P-Value	VIF
Constant	0.74968	0.00377	198.92	0.000	
Time	-0.001102	0.000327	-3.37	0.001	2.00
Condition					
B	0.00040	0.00533	0.08	0.940	3.98
Time*Condition					
B	0.000159	0.000463	0.34	0.732	4.98

Regression Equation (c)

Condition			
A	Operating rate	=	0.68606 - 0.001872 Time
B	Operating rate	=	0.68949 - 0.002441 Time

Coefficients

Term	Coef	SE Coef	T-Value	P-Value	VIF
Constant	0.68606	0.00606	113.30	0.000	
Time	-0.001872	0.000526	-3.56	0.000	2.00
Condition					
B	0.00343	0.00856	0.40	0.689	3.98
Time*Condition					
B	-0.000569	0.000744	-0.77	0.445	4.98

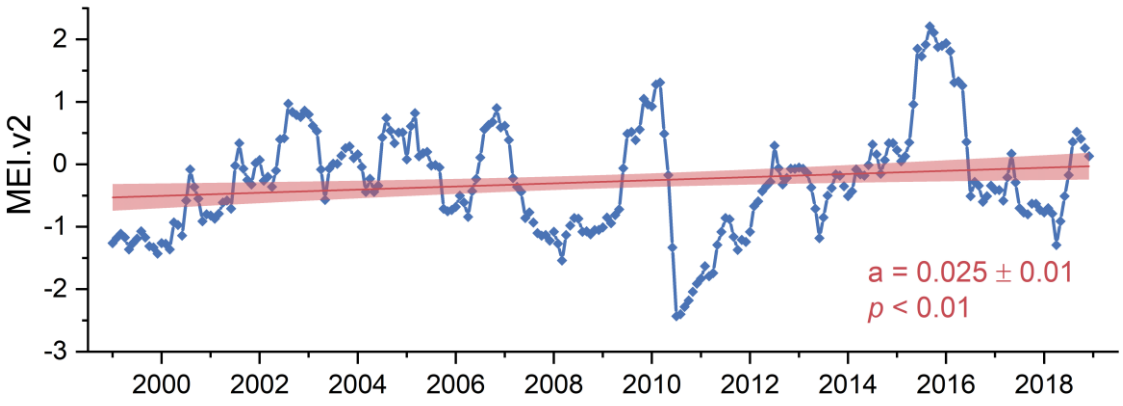

Figure S2 Monthly MEI.v2 variations from 1999 to 2018 and the linear trend, with the shaded area representing the 95% confidence intervals.